RCA Review

IC with Borophosphosilicate Glass Dielectric

September 1982 Volume 43 No. 3

RCARCI 43(3) 421–566 (1982)

Cover:
The cover shows a scanning electron micrograph of the radiation hardened C^2L IC described in the paper by Napoli, et al. The interlevel dielectric in this IC is borophosphosilicate glass, discussed in the paper by Kern and Schnable. The smooth low-defect surface and tapered contours that can be obtained with this glass, which can be fused and reflowed at low temperature (850°C), are clearly visible.

RCA Review, published quarterly in March, June, September and December by RCA Research and Engineering, RCA Corporation, Princeton, New Jersey 08540. Entered as second class matter July 3, 1950 under the Act of March 3, 1879., Second-class postage paid at Princeton, New Jersey, and at additional mailing offices. Effective January 1, 1978, subscription rates as follows: United States and Canada: one year $8.00, two years $14.00, three years $18.00; in other countries, one year $8.60, two years $15.20, three years $19.80. Single copies (except for special issues) up to five years old $3.00.

RCA
Review

RCA Review (ISSN 0033-6831) is a technical journal published quarterly by RCA Research and Engineering in cooperation with the subsidiaries and divisions of RCA.

Contents

423 **Chemically Vapor-Deposited Borophosphosilicate Glasses for Silicon Device Applications**
Werner Kern and George L. Schnable

458 **A Radiation Hardened 256X4 Bulk CMOS RAM**
L. S. Napoli, R. K. Smeltzer, R. Donnelly, and J. Yeh

464 **Single Sideband, Amplitude Modulated, Satellite Voice Communication System Having 6000 Channels per Transponder**
Krishnamurthy Jonnalagadda

489 **Broadband Microwave Power Amplifiers Using Lumped-Element Matching and Distributed Combining Techniques**
R. L. Camisa and A. Mikelsons

504 **Offset Near-Field Gregorian Antenna Scanning Beam Analysis**
Eugene C. Ngai

529 **A Simplified Real Frequency Technique for Broadband Matching a Complex Generator to a Complex Load**
B. S. Yarman

542 **The Photoresponse of Thin-Film PtSi Schottky Barrier Detectors with Optical Cavity**
Hammam Elabd and Walter F. Kosonocky

548 **Theory of Large-Angle Deflection of Electrons in the Magnetic Field Inside a Television Tube**
Basab B. Dasgupta

558 **Patents**

561 **Authors**

September 1982 Volume 43 Number 3 ISSN 0033-6831

RCA Corporation

Thornton F. Bradshaw Chairman and Chief Executive Officer

Editorial Advisory Board

Chairman, J. J. Tietjen RCA Laboratories
H. Kressel RCA Laboratories
J. Kurshan RCA Laboratories
W. J. Merz Laboratories RCA, Ltd.
K. H. Powers RCA Laboratories
R. E. Quinn RCA Laboratories
C. C. Richard International Licensing
T. O. Stanley RCA Laboratories
A. H. Teger RCA Laboratories
W. M. Webster RCA Laboratories
B. F. Williams RCA Laboratories

Editor **Ralph F. Ciafone**
Associate Editor **Rita L. Strmensky**

Editorial Representatives

D. R. Higgs Missile and Surface Radar
C. Hoyt Consumer Electronics Division
T. E. King RCA Research and Engineering
R. Mausler National Broadcasting Company
M. Rosenthal RCA Americom, Inc.
J. Schoen Solid State Division
M. G. Pietz RCA Advanced Technology Laboratories
W. S. Sepich Commercial Communications Systems Division
J. E. Steoger RCA Service Company
D. Tannenbaum Government Communications Systems

© RCA Corporation 1982. All rights reserved, except that express permission is hereby granted for the use in computer-based and other information-service systems of titles and abstracts of papers published in RCA Review.

Chemically Vapor-Deposited Borophosphosilicate Glasses for Silicon Device Applications

Werner Kern and George L. Schnable
RCA Laboratories, Princeton, NJ 08540

Abstract—Borophosphosilicate glass (BPSG) films have been used as fusable deposited dielectrics in silicon-gate MOS integrated circuits, with fusion tapering achieved at temperatures 100°C to 200°C lower than is normally possible with phosphosilicate glass films (PSG). The BPSG films were deposited on silicon wafers by the oxidation of the hydrides at 430°C in conventional atmospheric-pressure chemical-vapor-deposition (CVD) systems. Physical and chemical properties of CVD BPSG films have been characterized, both for as-deposited and for fused films. The relationship between deposited BPSG film composition and infrared absorption, solution etch rate, and fusion temperature is discussed, and examples of BPSG compositions that can be fused at 900-950°C and 800-850°C are given.

In addition to having lower fusion temperature than PSG films, BPSG films have lower as-deposited intrinsic tensile stress and low aqueous chemical etch rate; they have been considered for applications where these characteristics are advantageous.

1. Introduction

The recent interest in borophosphosilicate glass (BPSG) is primarily for fusion tapering applications in fabricating high-density silicon integrated circuits where the conventional phosphosilicate glass (PSG) containing 6 to 8 wt% P cannot be used. PSG requires unacceptably high temperatures (in the 1000 to 1100°C range) to form adequately tapered contours over steep steps of oxide and polycrystalline silicon in the device topography. Gradually tapered steps are imperative to ensure continuity and maintenance of film thickness of subsequently deposited metal-conductor interconnect lines. Failure to provide for

tapered steps in the dielectric can result in electrical defects, electromigration problems, and impairment of device reliability. Chemical etching with buffered hydrofluoric acid solutions or by use of plasma techniques, to open vias through the fused glass to underlying polycrystalline silicon or metal silicide electrical contact areas, results in steep walls with sharp top edges. A second fusion, known as reflow, is therefore needed to form an optimally rounded contour for improved metal coverage.

The fusion temperature of PSG can be lowered by substantially increasing the phosphorus concentration in the glass. However, serious reliability problems can arise due to aluminum corrosion and/or electrical instability of the devices during operation.

Addition of boric oxide (B_2O_3) to PSG by co-oxidation of the hydrides yields BPSG, whose fusion temperatures are significantly lower. Depending on the boron concentration, the fusion temperature can be lowered by 150-350°C. The higher the boron content, the lower the fusion or flow temperature of the glass. The main functions of the phosphorus in the glass are for chemically stabilizing the glass structure and for protecting the devices against mobile sodium ions. We will show that BPSG films are at least as effective in this latter respect as PSG films of similar phosphorus content.

Other advantages of BPSG over PSG are lower chemical etch rates in buffered hydrofluoric acid solutions used for via etching, lower intrinsic tensile stress (which allows the deposition of thicker defect-free insulator layers and over-metal passivation protect coatings), and increased dopant diffusivity (which allows use of the glass as a solid/solid diffusion source at much lower temperatures).

Chemical vapor deposition (CVD) of borophosphosilicate glass films was first described[1] in 1970. A U.S. patent[2] was issued to RCA in 1969 on the CVD of silicate glass coatings, including BPSG, for semiconductor devices. Use of BPSG for etch-rate control was described[3] in 1975. CVD of BPSG films was noted in a review[4] in 1978 and in an article[5] in March 1982. The application of BPSG for low-temperature reflow[6] in integrated circuit processing was described in May 1982. Two papers[7,8] were presented in July 1982 where CVD BPSG was used as flow and reflow fusion tapering glass in CMOS/SOS technology, a third paper[9] on BPSG applications for SOS ICs has been prepared for presentation in October 1982, and a fourth[10] is included in this issue of *RCA Review*. The only other published papers on BPSG, on the basis of a thorough literature search, are those relating to the phase relationships of B_2O_3-SiO_2-P_2O_5 bulk glasses.[11-13]

In the present paper we briefly describe the CVD conditions for preparing BPSG films; discuss analytical methods for composition control and film characterization; present important physical, chemi-

cal, and dielectric properties of the films; and finally point out and exemplify a number of possible applications in silicon device technology.

We refer throughout this paper to three types of BPSG films denoted, for convenience, as types A, B, and C. They differ mainly in increasing boron content in concentrations that lead to a lowering of the fusion-flow temperature in approximately 100°C steps.

2. Deposition of BPSG Films

2.1 CVD of PSG, BSG, and BPSG

Chemical vapor deposition of phosphosilicate glass (PSG) and borosilicate glass (BSG) by oxidation of the hydrides in an inert gas diluent at atmospheric pressure in the 300 to 500°C temperature range is widely used in semiconductor technology, and has been well established and researched. For a comprehensive review of the subject the reader may consult References [4] and [5].

Films of BPSG can be prepared similarly, by co-oxidation of silane, phosphine, and diborane with oxygen diluted with an inert gas, usually nitrogen.[1-6]

2.2 Standard CVD Conditions

Most of our exploratory work was carried out with an RCA rotary CVD reactor described elsewhere.[14] Nitrogen-diluted semiconductor grade hydride source gases were used, at the concentrations listed in Table 1, with oxygen as the oxidant and nitrogen as the diluent and carrier gas. The oxygen-to-hydride ratio was held fixed at 20:1, and the substrate temperature for film deposition was maintained at 430 ± 5°C. Chemically polished (100)-plane silicon wafers were used as the usual test substrate. Evaluation and analyses of the films were conducted as described in Sec. 3.

2.3 CVD Parameters

Systematic experiments to determine CVD parameters over a wide range of gas flow ratios and deposition conditions have led to the following results.

(1) The rate of formation of BPSG by co-oxidation of SiH_4, B_2H_6, and PH_3 with O_2 in N_2 is different from that expected on the basis of the single hydrides. In other words, the oxidation kinetics of the mixed components is different from that expected from the single components. Inhibiting or synergistic effects of this type are not uncommon

Table 1—CVD Conditions for BPSG "Standard" Compositions*

	BPSG Type A	BPSG Type B	BPSG Type C
Gas Flow Rates (cc/min)			
4.0% SiH_4 in N_2	1052	916	660
2.0% B_2H_6 in N_2	200	300	300
1.0% PH_3 in N_2	546	819	656
Total Equivalent Hydrides	51.5	50.8	39.0
O_2	1031	1017	780
N_2	8200	7200	7600
Total Gas Flow Rate	11,000	10,250	10,000
Total Hydrides (%)			
SiH_4	81.6	72.1	68.0
B_2H_6	7.8	11.8	15.0
PH_3	10.6	16.1	17.0
Total Equivalent Hydrides	100.0	100.0	100.0
Gas Flow Ratios			
O_2/Hydrides	20	20	20
PH_3/B_2H_6	1.36	1.36	1.13
B_2H_6/SiH_4	0.096	0.164	0.221
PH_3/SiH_4	0.130	0.223	0.250
Film Deposition Rate Range (KÅ/min)	1.2–1.5	1.0–1.3	0.9–1.1

* All films were deposited in an RCA rotary hotplate reactor featuring a 23-cm-diameter substrate plate and a glass belljar of 25-cm height and 21-cm inside diameter.[14] The deposition temperature was 430 ± 5°C as measured by digital thermocouple thermometer and bimetallic surface thermometers. Gas flow controllers with rotameters in series were used to control the hydride flow rates.

in CVD. The deposition rates listed in Table 2 for BPSG type A and type B, and those for its components BSG, PSG, SiO_2, and BPG indicate a strong mutual inhibition of the hydride components. Deposition of BPSG type A under the standardized conditions noted gave a deposition rate of 1460 Å/min. Omitting the B_2H_6 and the O_2 corresponding to the 20:1 ratio B_2H_6/O_2 and adding a like amount of N_2 deposits PSG at a rate of 2250 Å/min, demonstrating the very strong inhibitory effect of B_2H_6 on the oxidation rate of PH_3. Omitting both the B_2H_6 and PH_3 and their corresponding O_2 flows to deposit SiO_2 had a similarly large effect on reducing the film deposition rate, indicating strong inhibition of SiH_4 oxidation by B_2H_6 and, to a smaller extent, by PH_3. The inhibitory effect of PH_3 on B_2H_6 and SiH_4

Table 2—Mutual Oxidation Inhibition of Hydrides as Evidenced by Film Deposition Rates*

		Film Deposition Rate (Å/min) for Hydride Flow Rates as used for BPSG	
Hydride Reactant	Resulting Film	Type A	Type B
SiH_4	SiO_2	2380	2380
$SiH_4 + PH_3$	PSG	2250	2200
$SiH_4 + B_2H_6$	BSG	1230	1130
$SiH_4 + PH_3 + B_2H_6$	BPSG	1460	1150
$PH_3 + B_2H_6$	BPG	400	400

* Deposition conditions as outlined in Table 1; total gas flow rate held constant by N_2 substitution for gases omitted.

oxidation is much less, indicating that the deposition rate of BPSG is not substantially affected by the PH_3 component. Omitting SiH_4/O_2 leads to borophosphate glass (BPG) at a deposition rate of 400 Å/min. These findings agree with other literature data[6] and are consistent with the thermodynamics of hydride oxidation.[4,15,16]

(2) The effect of the diborane and phosphine concentrations on the chemical composition of the resulting glasses was studied for a range of 3 to 25 mol% B_2H_6 with additions of 8 to 14 mol% PH_3, both in terms of total hydrides. Under these conditions, the boron content up to about 11 wt% B in the glasses rose linearly with increasing diborane concentrations. As expected, the phosphorus content in the glasses decreased sharply with increasing diborane concentrations. Increasing the phosphine concentration in the gas mixture had generally only a secondary effect of slightly decreasing the boron content of the glasses, except for very high ratios of PH_3/B_2H_6.

(3) The effects of changes from the standard deposition temperature (430°C) and O_2/hydride ratio (20:1) on the film composition (B and P contents) and deposition rate (DR) were tested for BPSG types A and B. Decreasing the temperature to 410°C at the 20:1 ratio increased B and DR for types A and B, and decreased P for type B. No substantial changes occurred at 450°C and the 20:1 ratio. Lowering the ratio to 10:1 at 410, 430 and 450°C increased B and tended to decrease DR for types A and B. Increasing the ratio to 30:1 at 410°C increased P, B and DR for type A, whereas at 450°C P increased and DR decreased; 410 and 430°C at 30:1 caused an increase of B and P for type B.

(4) The ratio wt% P/wt% B in the glass films tends to be directly proportional to the ratio mol% PH_3/mol% B_2H_6 in the gas mixture from which the glass was prepared.

(5) The effect of diborane and phosphine concentrations in the gas mixture on the fusion temperature of the resulting BPSG films is presented graphically in Fig. 1. As the B_2H_6 concentration increases, forming progressively boron-richer glass films, the fusion temperature decreases. Phosphine exerts the additional but secondary influence of depressing the fusion temperature.

(6) Average compositions of several types of BPSG are listed in Table 3 together with their fusion ranges in dry nitrogen and in steam. For comparison, data for PSG, BSG, and SiO_2 have also been included.

2.4 CVD Reactor Systems

Chemical vapor deposition of BPSG films is readily feasible in large-scale commercial normal-pressure reactor systems[4,14] under conditions similar to the ones described for our laboratory research reactor. Systems for which deposition conditions were optimized include the

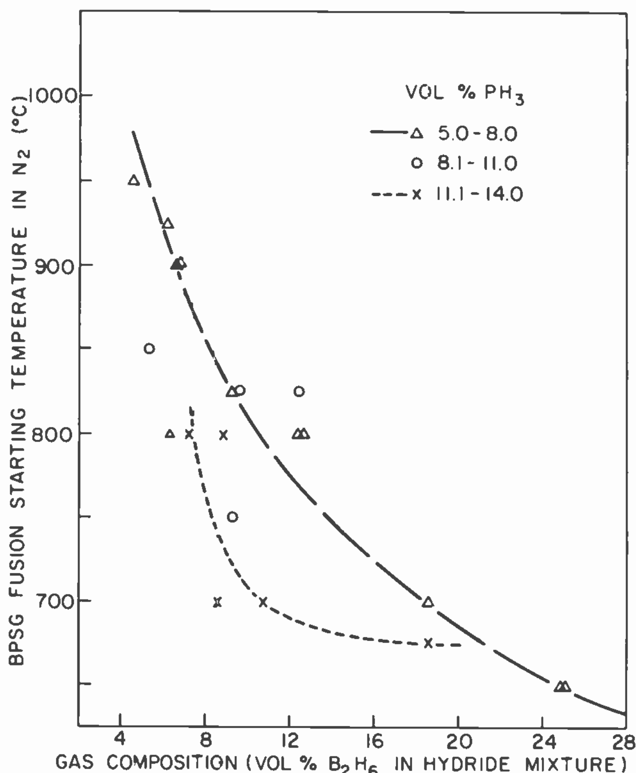

Fig. 1—BPSG fusion temperature in dry N_2 versus diborane and phosphine concentration in reactant gas stream.

Model 216 Pyrox rotary batch reactor by Tempress-Microelectronics, the continuous oxide deposition reactor AMS-2100 by Applied Materials, Inc., and the PWS-2000 continuous reactor by Pacific Western Systems, Inc.

The most recent addition to commercial chemical vapor deposition systems are those that combine plasma-enhanced CVD with low-pressure CVD techniques in a tubular reaction chamber.[17] Equipment of this type is available from Advanced Semiconductor Materials/

Table 3—Typical Composition and Flow Temperatures of Fusable CVD Glasses

Glass Type	Average Composition		Flow Temperature (°C)	
	Wt% B	Wt% P	Steam	Dry N_2
BPSG Type A	4	4	900–925	925–950
BPSG Type B	5	4	800–825	825–850
BPSG Type C	6	3	700–725	725–750
BSG	6.5	0	800–825	825–850
PSG	0	6.5	1050–1075	1075–1100
SiO_2	0	0	<1725	1725

America, Inc. and from Pacific Western Systems, Inc. Feasibility studies for depositing BPSG films by plasma-enhanced low-pressure CVD techniques have shown that compositions suitable for fusion flow can be successfully obtained at a deposition temperature of 380°C and at a pressure of 0.9 Torr, using N_2O as the oxidant for the ternary hydride gas mixture.[18]

3. Analytical Methods

Several methods can be used for determining the chemical composition of BPSG films.

3.1 Wet Chemical Analysis

Primary calibration for boron and phosphorus may be done by standardized wet chemical colorimetric microanalysis of the dissolved film. This method is based on spectrophotometric measurements of colored complexes (N-methylthionine for boron,[19,20] phosphomolybdenum blue for phosphorus[21,22]), and uses pure boric acid and alkali phosphate standards for calibration. The method is slow and destructive, but should be reliable for the purpose of calibration of more convenient and rapid secondary methods for routine applications.

3.2 Instrumental Analysis Methods

We have also examined electron probe microanalysis for determining the elemental composition. However, this method has certain limitations because of the relatively low energy electron beam needed for typical BPSG films of one micrometer or less thickness.

Secondary ion mass spectroscopy (SIMS) is particularly well suited for examining the relative elemental composition of BPSG films as a function of layer depth. The estimated absolute accuracy for B, P, and Si is not much better than ±10%; standards of ion-implanted B and P in SiO_2 were used for calibration.

3.3 X-Ray Fluorescence Analysis

The phosphorus content of the films can be readily determined by x-ray fluoresence spectroscopy, just as for binary PSG films,[21,22] by use of accurate BPSG standard samples. Either the more conventional and accurate wavelength dispersive technique or the newer, very convenient computerized energy dispersive technique (such as EDAX) is suitable for rapid quality control. Commercially available systems,

such as the PGT-800XRF Materials Analyzer by Princeton Gamma-Tech, provide a single-measurement accuracy of ±3% of the phosphorus present in the range of 2 to 15 wt% P. The results in terms of wt% P are displayed digitally on a video screen in just 2 minutes and are also printed out on tape.

3.4 Infrared Spectroscopy

Infrared absorption spectroscopy has been used for determining the glass composition of BPSG films on special silicon wafer substrates. Despite its limitations due to overlapping of the critical B—O and P=O absorption bands, this high-speed method has proven sufficiently accurate for practical applications. Infrared spectra for SiO_2, BSG, PSG, and BPSG (type B) CVD films are shown superimposed for comparison in Fig. 2, which clearly shows the spectral relationships. The technique developed for measuring the absorbance ratios is outlined in Fig. 3. The absorbance ratio (net B—O at 7.30 μm)/(total Si—O at ~9.25 μm max.) can then be related to wt% B in the film by use of a calibration graph. Similarly, the wt% P can be estimated from the absorbance ratio ("P=O" at 7.60 μm)/(total Si—O ~9.25 μm max.). The absorbance ratios should be normalized for film thickness (10,000 Å) for improved accuracy. The same wavelength positions for reading the absorbance maxima are used for as-deposited and for densified films.

It may be noted that the absorbance measurement taken at the 7.6 μm P=O maximum is not being corrected for the B—O absorbance

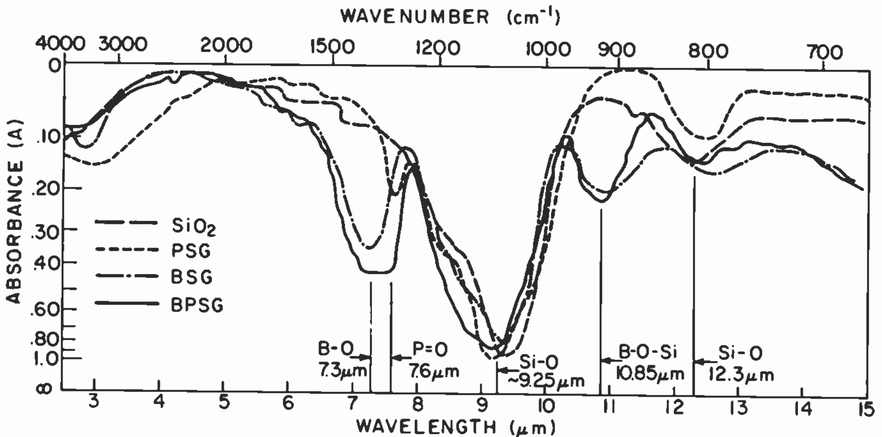

Fig. 2—Comparative infrared absorption spectra for as-deposited films of CVD SiO_2, PSG, BSG, and BPSG on IR-Si wafers measured against blank wafer (Perkin-Elmer Infrared Spectrophotometer Model 137).

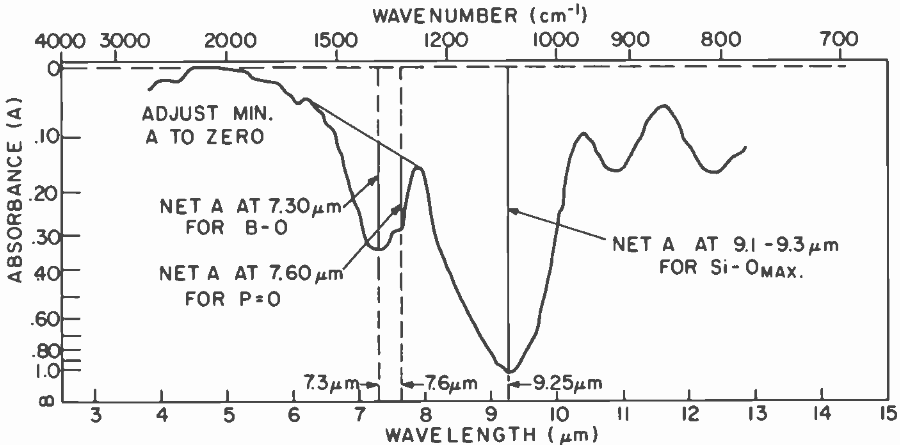

Fig. 3—Determination of approximate BPSG composition from IR absorption spectrum. Film on special IR-Si wafer measured against IR-Si blank. Absorbance ratios (*R*) are calculated as outlined in text. The spectrum shown is for a BPSG type A film as-deposited.

contributed in this region. Rather, we have used the composite value in an empirical manner, which we found preferable even though it is not ideal analytically. Attempts to resolve the two bands by various techniques, including infrared spectroscopy in liquid helium and Raman spectroscopy, have not been successful.

The substrate wafers needed for infrared measurements are high-resistivity (typically 50 to 100 ohm-cm) float zone refined silicon of at least 0.6 mm thickness, polished on both sides. The infrared transmission should be uniform in the wavelength range of at least 6 to 14 µm. Measurements are done with the uncoated half of the silicon wafer in the reference beam of the instrument.

Infrared spectra for as-deposited BPSG type A and B films taken in a Perkin-Elmer Model 683 double-beam infrared spectrophotometer against a blank silicon control wafer are shown in Fig. 4 for the wavelength range of 5.4 to 32 µm.

Densification of BPSG films at 700°C in nitrogen improves the resolution in the critical region of the P=O band at 7.60 µm without changing the intensity or the wavelength position of the maxima of the critical B—O and P=O absorption bands. The intensification of the Si—O stretching vibration band on densification is normal and is responsible for the changes in the absorbance ratios. Its wavelength shift from 9.25 µm to 9.10 µm is, again, characteristic of SiO_2[23] and silicates[21,23-26] but does not affect the reading, since we utilize the maximum regardless of its exact location.

Use of the relationship of infrared absorbance ratios and film com-

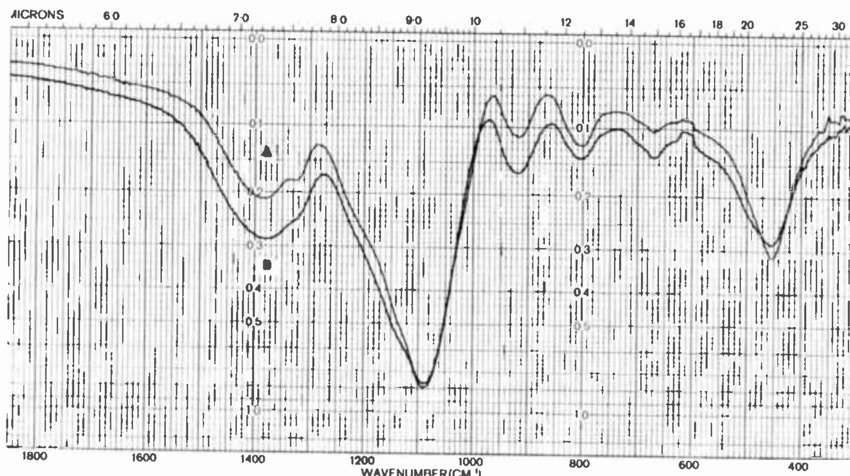

Fig. 4—Infrared absorption spectra of type A and type B BPSG. (Perkin-Elmer Model 683 Infrared Spectrophotometer)

position in terms of wt% B and wt% P allows the determination of the boron content and an approximate estimation of the phosphorus content in the glass from the infrared data alone, similar to the analysis of the binary films BSG[25] and PSG.[21,26]

It is important to realize that some changes occur in as-deposited films, due mainly to room-temperature densification effects. These changes affect the infrared absorption spectrum and the chemical etch rates, which is characteristic of practically all types of films deposited at low temperature. One should, therefore, execute these analyses within hours after deposition or preferably, after a densification treatment well below fusion temperature (30 min at 700°C in N_2), which anneals and stabilizes the films.

3.5 Etch-Rate Measurements

Chemical etch-rate measurements in liquid etchants provide an additional convenient test for rapid composition control[6] that can be performed in minutes by interferometric or ellipsometric determination of the film thickness followed by measuring the film dissolution time.[27]

Etch-rate data for standard BPSG films in both buffered hydrofluoric acid solution (BHF) and in the more composition-sensitive P-etch are summarized in Table 4 for both as-deposited and for densified films. Increasing the phosphorus concentration increases the etch rate in both etchants, as for binary PSG films,[21,28] whereas increasing the boron concentration decreases the BHF etch rate, as in the case of BSG films.[24,28]

Table 4—Chemical Etch Rate Ranges of BPSG, BSG, PSG, and SiO_2

	Etch Rate (Å/sec) at 25°C	
	BHF[a]	P-Etch[b]
Type A BPSG		
As-Deposited	25–30	50–60
Densified	12–15	18–23
Type B BPSG		
As-Deposited	12–16	100–120
Densified	8–11	30–35
Type C BPSG		
As-Deposited	11–14	150–170
Densified	7–9	55–65
6.5 Wt% B-BSG		
As-Deposited	6–7	50–70
Densified	4–5	15–20
6.5 Wt% P-PSG		
As-Deposited	130–140	120–130
Densified	90–100	65–75
SiO_2		
As-Deposited	92	15–16
Thermally-Grown	16	2.0

[a] 1 vol. HF 49% + 6 vol. NH_4F 40%
[b] 3 vol. HF 49% + 2 vol. HNO_3 70% + 60 vol. H_2O.

Etch-rate data should be taken at a controlled temperature,[27] preferably under fixed isothermal conditions, such as 25.0°C. The effects of temperature on the etch rate in BHF of BPSG type A, type B, and thermally grown SiO_2 (for comparison) are apparent from the plots in Fig. 5. A correlation can be made, by use of these graphs, between the etch rates and different temperatures. The differences in the slope of the curves indicate different activation energies for the etching mechanism of the three types of films.

In conjunction with the infrared data and the x-ray fluorescence measurements for phosphorus, the etch-rate values assist in rapid composition control.

3.6 Glass Fusion Tests

The most pertinent test for ascertaining the correct glass properties of BPSG films intended for flow and/or reflow tapering applications is to expose glassed silicon wafers with topographic test patterns of polycrystalline silicon and thermally grown SiO_2 to the actual fusion treatments for which they are intended. Side-view examination of the samples by SEM will reveal directly the degrees of fusion and tapering. For more accurate determination of step coverage, SEM of sample cross sections is an unexcelled technique.

We have tried various alternative methods for checking glass fusion more rapidly than is possible by SEM. However, none of the methods tested proved to be consistently reliable, including stylus profilometry

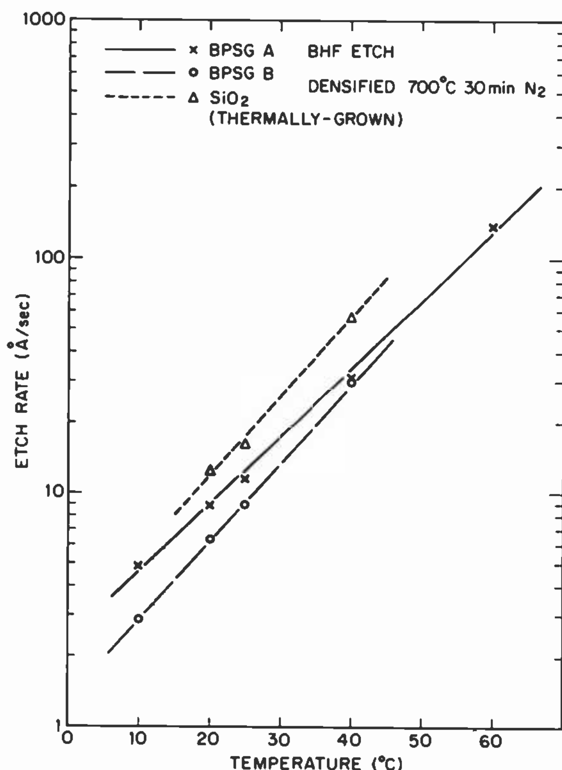

Fig. 5—Buffered-HF (6:1) etch rate as a function of temperature for BPSG type A, type B, and thermally grown SiO_2.

for surface roughness or smoothness, laser scanning and elastic scattering techniques, light microscopy of taper edges, and change in width of a tapered step etched in the glass before fusion. Scanning electron microscopy appears to be the only reliable method. Fusion tests are therefore done only as a final check of important samples.

4. Properties of BPSG Films

4.1 Phase Relationships

Phosphosilicate glass is widely used as a fusable layer in silicon-gate MOS integrated circuits, where it provides a smooth, gradually contoured surface over delineated polysilicon lines. Such surfaces, as indicated in a number of publications,[29-32] provide a favorable topology for coverage by subsequently deposited aluminum metal. Phosphosilicate glass also provides a very effective alkali ion gettering capability.[33-36]

Phosphosilicate compositions that have been used for fusable layers range from 6 wt% up to approximately 10 wt% phosphorus. In this composition range, higher phosphorus concentrations correspond to lower flow temperatures. Higher phosphorus-containing phosphosilicates, however, tend to be more hygroscopic. For IC applications in which devices are encapsulated in plastic, phosphorus concentrations over 7 wt% P can result in increased susceptibility to aluminum metal corrosion during device usage in humid ambients.[37]

Unfortunately, a relatively large increase in the concentration of phosphorus is required above the frequently used level of 6.5 wt% to attain a significant decrease of the fusion temperature in the range of 1000 to 1100°C. For example, to reduce the fusion temperature of a 6.5 wt% P-PSG from 1100°C to 1050°C, an increase in the phosphorus content to 9.5 wt% is needed to attain the same viscosity.[38]

Borophosphosilicate glasses offer the possibility of lower flow temperatures[6] than those attainable with 7 wt% P PSG. Binary borosilicates can also offer lower flow temperatures,[24] but they do not provide an alkali ion gettering capability.[39]

There is relatively little data available on the ternary oxide system $B_2O_3—P_2O_5—SiO_2$, although some information is available on flow temperatures of a few portions of the ternary system.[6,11-13] A CVD BPSG film containing 3.4 wt% B and 4.5 wt% P was shown to have flow properties similar to a PSG film with >7 wt% P, both at 920°C in steam or at 1000°C in nitrogen.[6] By contrast, there is a considerable amount of information available on the $B_2O_3—SiO_2$ binary oxide system[40,41] and on the $P_2O_4—SiO_2$ binary oxide system.[33,42-45]

Fig. 6 shows the silica-rich corner of the ternary system $B_2O_3—P_2O_5—SiO_2$. For convenience, the B_2O_3 and P_2O_5 concentrations are expressed in percent by weight of B and P, respectively. Fusion temperatures of several BPSG compositions are indicated, and for comparison purposes, one BSG and one PSG composition are shown.

The binary and ternary oxide systems can be further complicated by the presence of water.[46] The fusion temperature of glasses can be lowered appreciably by the presence of retained water or by the equilibrium water content attained during fusion in a moisture-containing ambient.[47] In a steam ambient, the fusion temperature of phosphosilicate glass is decreased relative to that in a dry ambient.[32,37]

4.2 BPSG Fusion Parameters

The chemical composition of the borophosphosilicate glasses described has been selected primarily from the standpoint of fusion applications. The three types of BPSG fuse at temperatures 100°C apart: type A,

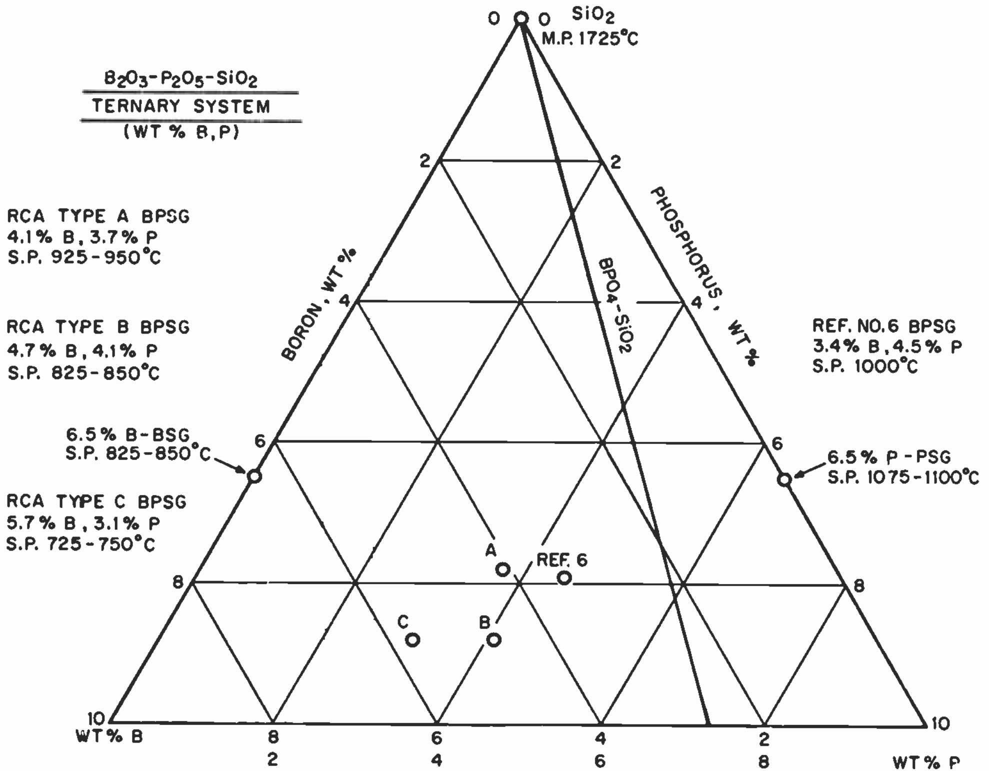

Fig. 6—Composition diagram of B_2O_3—P_2O_5—SiO_2 ternary system, with fusion temperature ranges as indicated for dry N_2 ambient.

900–950°C; type B, 800–850°C; and type C, 700–750°C. Compositions for intermediate fusion ranges have also been prepared. The reasons for specifying a range of temperatures rather than a single value are several-fold. Glass fusion is a gradual and continuous process that for a given glass composition and fusion temperature, depends to a secondary degree on fusion time, gas ambient, pressure, and thermal history of the glass. In addition, the degree of glass flow on device wafers is affected by feature size and height of the topography, film thickness, and surface condition of the substrate. Our standard heat treatment time is 30 min in a tube furnace, either in steam or in a dry inert gas (N_2), both under normal atmospheric pressure conditions. The lower half of each temperature range refers to steam; the upper half refers to dry ambient. This gives considerable flexibility to the process for the application engineer. The first fusion is frequently done in steam, whereas reflow after contact etching is done in nitrogen to avoid reoxidation of the exposed contacts. There are indications that

oxygen ambient, as found by Armstrong and Tolliver[32] in the case of PSG Fusion may also enhance the fusion flow of BPSG.

Several examples of BPSG over SiO_2 test patterns are shown in Figs. 7, 8, and 9. Examination by SEM at 5,000× or 10,000× shows BPSG before fusion to be always slightly rough, whereas after fusion the glass is perfectly smooth, with gradual tapers over the substrate steps. The SEMs also show the effect of dry versus steam ambient for identical samples heated at the same temperature. While heating at 900°C in dry nitrogen did not fuse the glass, 900°C in steam produced extensive fusion. The cross-section SEMs of the fused sample in Fig. 9 demonstrate the gradual contour of the taper formed.

As noted above, steam ambient at one atmosphere pressure allows a reduction of the BPSG dry fusion temperature of about 25–35°C. It is estimated that the flow temperature would be further lowered by approximately 60°C if the BPSG were flowed in a high-pressure oxidation system at 10 atmospheres water vapor; this estimate is based on the equation of effect of H_2O pressure on solubility of OH in glass.[48]

Densification of a glass film prior to fusion increases the degree of fusion, as shown in the SEMs of Fig. 10. It appears that thermal treatments below the flow temperature of the glass have an additive effect, increasing the degree of fusion resulting under the same conditions.

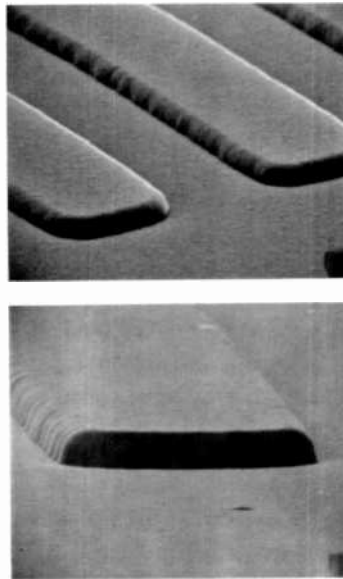

Fig. 7—BPSG type A over SiO_2 bars on Si after 30 min at 900°C in dry N_2. Surface and profile indicates that no fusion has taken place as yet. (Top SEM: 2000×, 70°; bottom SEM: 4000×, 80°).

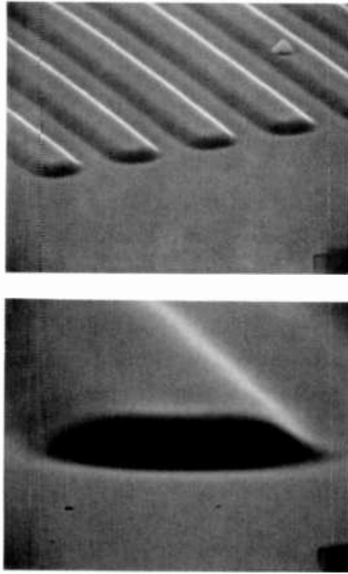

Fig. 8—Samples from same wafer shown in Fig. 7, but after 30 min at 900°C in steam. Smoothness of surfaces and tapers indicates good fusion (Top SEM: 800×, 70°; Bottom SEM: 4000×, 80°).

Time can be traded for temperature. This effect is clearly demonstrated in Fig. 11 which was prepared for high-temperature planarization studies with BPSG. Silicon samples with 8000-Å-thick widely spaced SiO_2 patterns were coated with 13,000-Å BPSG type AB and fusion-flowed at 1000°C in N_2 for periods of 30, 120, and 390 minutes. The resulting profile was then examined by Tencor stylus measurements and by cross-section SEM. The graphs in Fig. 11 show the rapid initial decrease of the step height with time at 1000°C, or with temperature from 900–1200°C at a fixed time period of 120 minutes. Zero step height would indicate complete planarization, that is, complete filling of the spaces between the steps with glass resulting in a planar surface. These effects can be utilized to either reduce the temperature necessary for fusion-flow, or to achieve planarization of refractory structures that may be applicable to VLSI.

4.3 Chemical Composition and Compositional Uniformity

The chemical compositions of over 20 BPSG samples deposited from a systematically varied range of diborane and phosphine concentrations were determined by wet chemical microanalysis, electron-probe microanalysis, x-ray fluorescence analysis for phosphorus, and secondary ion mass spectroscopy. The results showed generally fair agree-

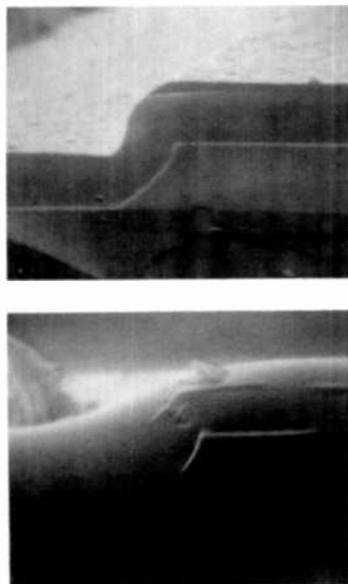

Fig. 9—Same as in Fig. 8. but cross-section views (SEMs: 8250×, 90°).

ment between the values for phosphorus, but not for boron. The average concentrations in terms of wt% B and wt% P for the main compositions of BPSG denoted as types A, B, and C have already been listed in Table 3, together with their fusion temperature ranges. For comparison, CVD BSG, CVD PSG, and SiO_2 (fused quartz) were also included.

The compositional uniformity of BPSG films in terms of boron and phosphorus content was examined by secondary ion mass spectroscopy (SIMS). Profile traces through the layers revealed an excellent uniformity of boron and phosphorus through the bulk of the film thickness. A slight increase of the phosphorus concentration was noted in the first 500 Å of the film above the silicon substrate in several of the samples analysed. A typical profile trace for an as-deposited film of BPSG type AB is presented in Fig. 12.

The etch rates in buffered HF are of importance in device contact etching; they are relatively insensitive to composition. The P-etch rates, on the other hand, are very sensitive to composition and are used as an analytical check. Film thickness as a function of etching time in P-etch offers a sensitive means for determining vertical compositional uniformity through the film. A good uniformity has been demonstrated, as shown in Fig. 13, for as-deposited BPSG type B. The effects of densification at a temperature of 700°C and of fusion at 850°C, both in nitrogen for 30 min, are illustrated for BPSG type B in

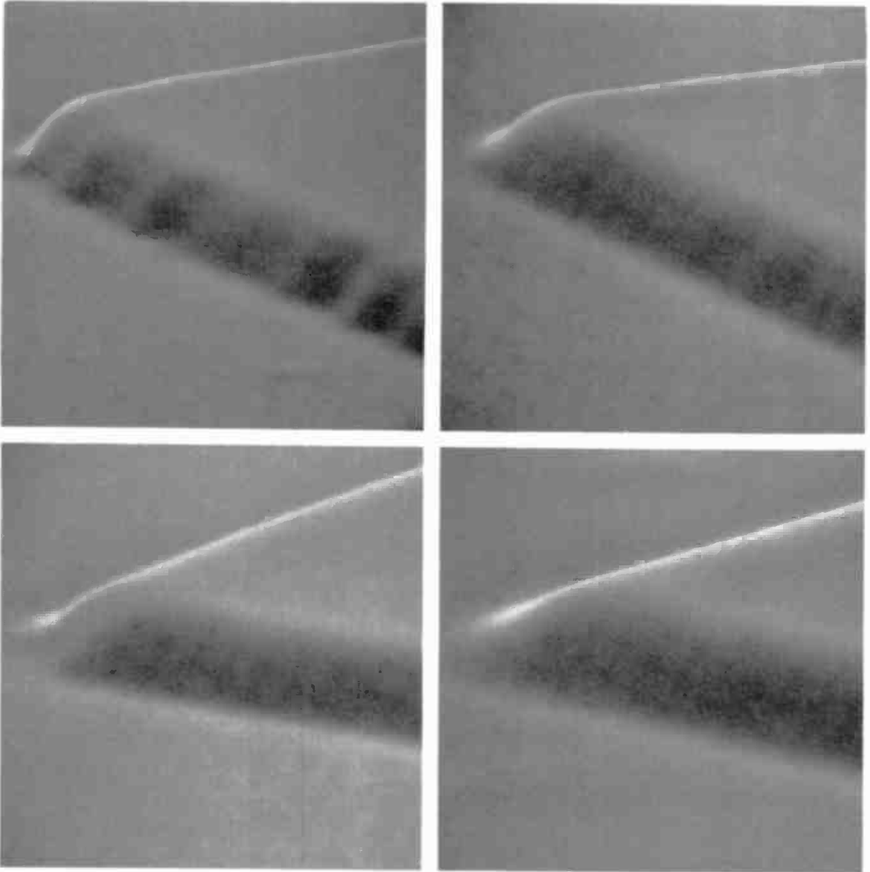

Fig. 10—BPSG type A fusion over 1-μ SiO_2 edges without (top) and with (bottom) prior densification at 700°C, 30 min N_2. Left: fused at 925°C, 30 min N_2; right: fused at 950°C, 30 min N_2. Conclusion: densification increases degree of fusion (SEMs at 9400×, 80°).

Fig. 14. The uniformity from the surface of the films through the bulk remains good. A slight but distinct etch rate decrease occurs in the first few hundred angstroms of the films at the silicon interface.

BPSG type A and type AB are relatively stable chemically during storage and exposure to humid ambients, similar to low-concentration PSG and BSG films. BPSG type B is more sensitive to humidity because of its higher boron content. Device wafers coated with this type of film should be processed promptly or kept under dry ambient condition, preferably in a desiccator. BPSG type C is the least stable and should be used only where the lowest fusion temperature must be used. Extended exposure of undensified films at high humidity can

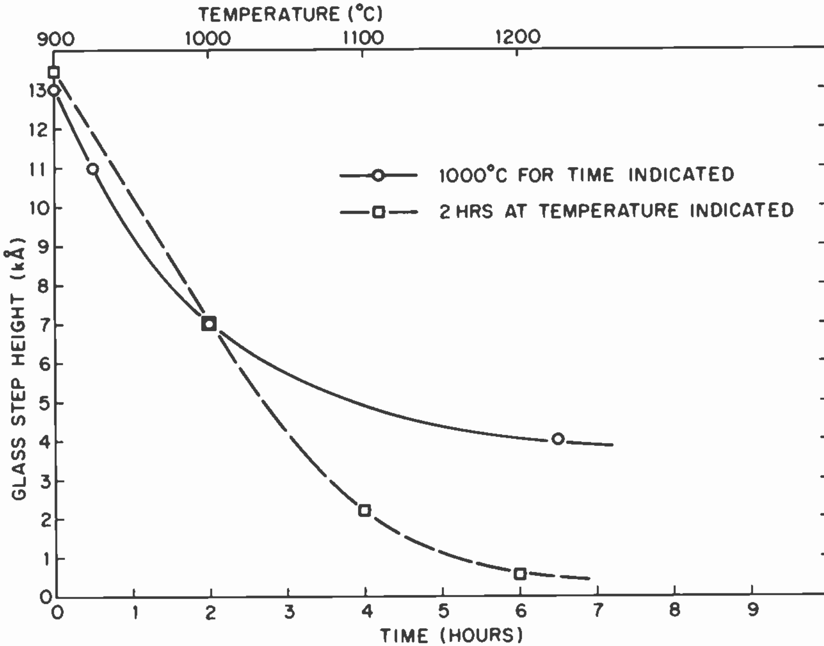

Fig. 11—BPSG type AB fusion flow as functions of time and temperature.

cause some surface devitrification, which becomes evident by the formation of boric acid crystals on the surface of the film. A dip in methanol readily dissolves the crystallites and restores a clear appearance of the film, but leaves the surface and the first few hundred angstroms of the film with a reduced boron concentration, as seen by SIMS profiling analysis and chemical etching tests. The desired flow to improve surface topology may be impaired in such cases.

The resistance of fused BPSG toward leaching in aqueous solutions was tested by infrared spectroscopy of samples before and after exposure to boiling deionized water for 5 minutes and to a hot 1:1 mixture of 30% H_2O_2 and 98% H_2SO_4 for 20 minutes. No changes in the spectra were recorded for BPSG type A. Some leaching of boron and phosphorus oxides for BPSG type B was evidenced by a decrease in absorbance intensity in the wavelength region of 7.0 to 7.8 μm.

4.4 Protection Efficiency Against Sodium Ions

Two types of tests were conducted in a comprehensive series of analyses to assess the protection effectiveness afforded by BPSG and PSG, a known Na^+ getter,[33, 34, 49] against sodium ions: (1) radiotracer measurements of Na^{22} penetration through the films on heating and

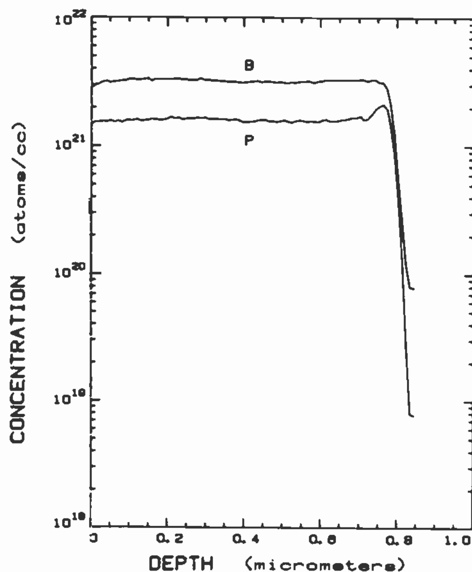

Fig. 12—Typical SIMS profile through a BPSG (type AB) film on silicon.

(2) capacitance-voltage bias-temperature stress measurements on metal-gate MOS transistors fabricated using BPSG or PSG as the passivation layer.

Radioactive tracer analyses with Na^{22} applied on the surface of glassed wafers followed by a drive-in diffusion step in N_2 at 500°C for 16 hours demonstrated the superior protective capability of BPSG over PSG. In wafers with a layer of 7720 Å fused 6 wt% P-PSG control or with 7560 Å fused BPSG test layer, both over thermal SiO_2 on Si, the sodium not retained by the BPSG amounted to only 0.03%, compared to 1.0% for the fused PSG. Even larger differences (0.002% vs 0.3%) were obtained with 3 wt% P-PSG layers that were not fused; in these cases the drive-in diffusion was carried out at the film deposition temperature of 430°C to minimize densification effects. Examples of the results obtained are presented in the profile curves in Figs. 15 and 16. In all tests the sodium was applied to the film surface in the form of a $Na^{22}Cl$ solution. The wafers were rinsed repeatedly with deionized water and then with alcohol after the diffusion heat treatment to remove excess $Na^{22}Cl$ from the surface. Autoradiograms were taken to check the uniformity of the sodium distribution. A series of etching steps (usually 10) in HF etchants was then applied to strip off layers of known thicknesses. The radioactivity of the wafers after each step was measured using a methane end-window beta radiation detector in a standard geometry, yielding a counting efficiency of 30%

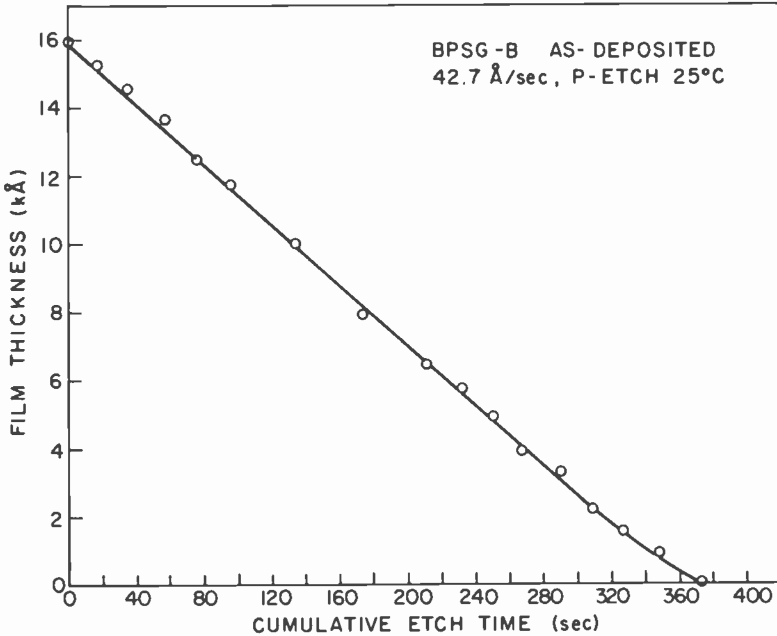

Fig. 13—Film thickness of BPSG type B as-deposited as a function of cumulative etch time for testing compositional uniformity through the film.

for Na^{22}. The concentration of sodium ions remaining on the wafers after each etching treatment was calculated from the Na^{22} radioactivity and the decay constant.

The CVBT electrical stress measurements were carried out with aluminum-metallized metal-gate MOS transistors. The controls consisted again of 3 wt% P-PSG passivation overcoats; BPSG type A films were used as the test passivation layer. The surfaces of the glassed device wafers were uniformly contaminated with sodium ions from 0.1 molar $NaHCO_3$ solution. Electrical measurements were made and graphically recorded initially and after successive heat treatments at 300, 350, 400, and 450°C. Devices with several types of 18,000-Å-thick BPSG overcoats survived heat treatments up to 400°C, whereas controls with standard 12,000-Å-thick 3 wt% P–PSG failed at temperatures as low as 350°C (large shifts in flatband voltage).

Measurements made with MIS capacitors that were fabricated with BPSG type A films and either clean or contaminated aluminum films as the top electrode have also confirmed the effectiveness of BPSG to protect against impurities. In these experiments, control wafers with 1000 Å of thermally grown SiO_2 films and clean In-Source* deposited

* Registered trade name, Applied Materials, Inc.

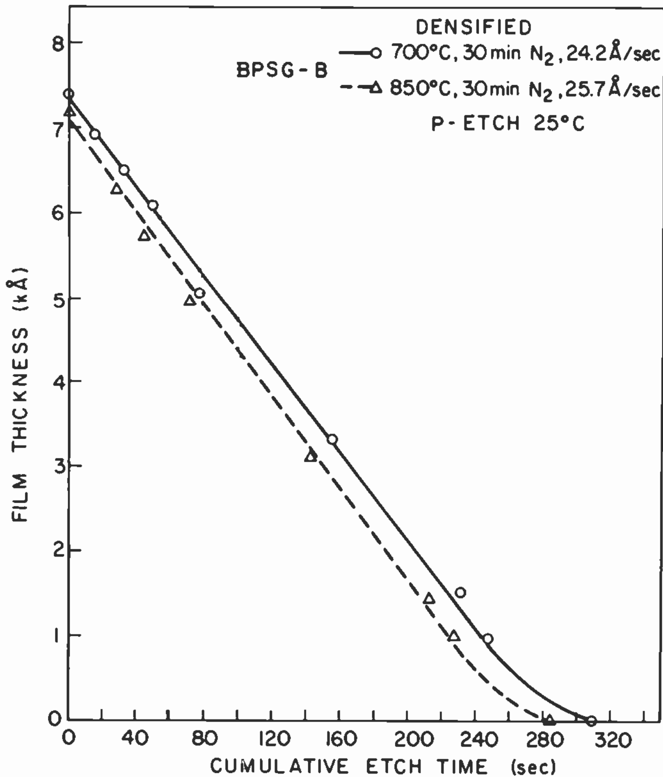

Fig. 14—Same type of plot as in Fig. 13, but for densified and for fused samples of BPSG type B from two different deposition runs.

aluminum dots as the top plate of a capacitor had a CVBT shift of 0.1 V, while those fabricated with a contaminated aluminum filament source had shifts of 15 V. The CVBT bias voltage was +10 V, the temperature 300°C, and the dwell time 3 minutes. The capacitors made from the test wafers with BPSG, fused at 950°C for 20 min in steam, showed a CVBT shift under the same conditions of about 1 V for both clean aluminum and contaminated aluminum dots and continued to shift with increasing bias voltage. The shift at 300°C for 3-minute stress was about 1 V for each 10-V bias voltage increment, indicating a strong polarization effect in BPSG, with masking against the injected contamination from the contaminated aluminum dots. Biasing the film at a constant voltage and increasing the stress time at 300°C in 3-minute intervals also indicated a polarizing effect in the BPSG. The shift was about 0.75 V per 3-minute stress interval at 300°C for a 10-V stress. Samples that were made from as-deposited (not fused) BPSG were unstable, both for clean and contaminated aluminum electrodes.

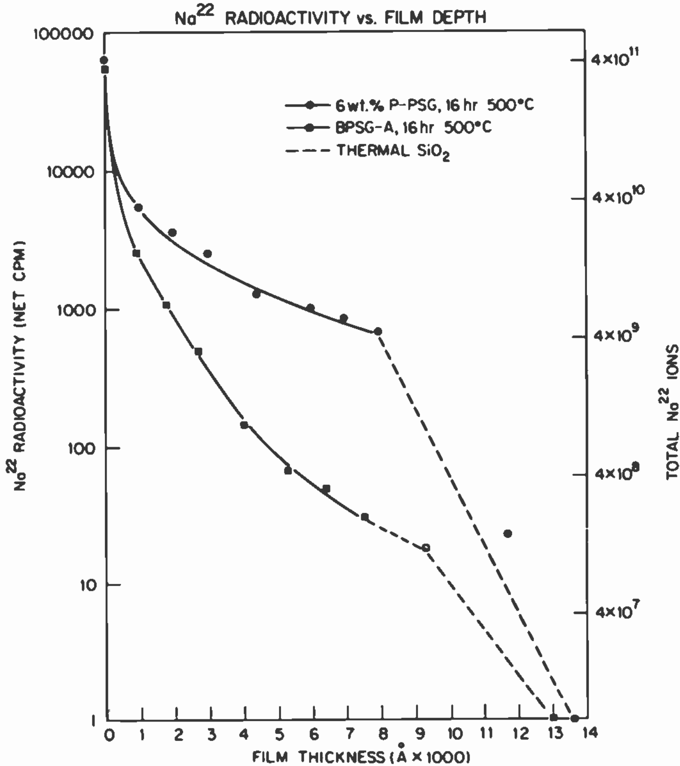

Fig. 15—Penetration of Na^{22} in fused PSG and BPSG layers (kÅ).

It is not yet clear whether the remarkable protective effectiveness of BPSG against sodium is based on gettering or on barrier mechanisms. Further work is in progress in this area to clarify these aspects. Nevertheless, the experimental results from the low-concentration carrier-free Na^{22} radioactivity measurements and those from electrical measurements with samples contaminated with sodium at many orders of magnitude higher concentrations agree in demonstrating the protective capability of BPSG.

4.5 Stress Properties

One of the outstanding properties of BPSG films is their relatively low intrinsic stress. This feature is not unexpected, since increasing the concentrations of both phosphorus in PSG and of boron in BSG allows the deposition of progressively thicker crack-free layers,[24] and stress measurements of PSG show a decreasing intrinsic stress level with increasing P content.[21,49,50] As a consequence, much thicker and crack-

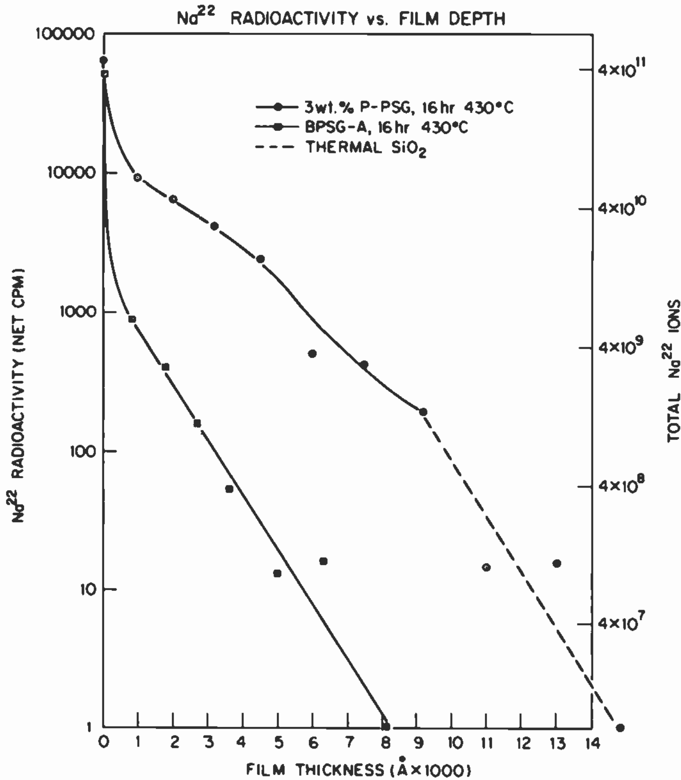

Fig. 16—Penetration of Na^{22} in low-temperature PSG and BPSG layers (kÅ).

free protective passivation layers can be deposited with BPSG over aluminum-metallized devices than is possible with CVD SiO_2 or 3–4 wt% P–PSG. For example, IC wafers with 1.5-μm-thick aluminum interconnections were coated with BPSG type A of 2.0-μm thickness. Thermal stress testing by exposure of the wafers to furnace temperatures ranging from 350 to 550°C, followed by rapid cooling, did not lead to microcracks or other structural defects, in contrast to PSG films of the same phosphorus content.

Similar tests with power device wafers having 4.0-μm-thick aluminum metallization layers that were overcoated with BPSG type A of 1.6-μm thickness withstood alloying in hydrogen at 425°C without cracking. In subsequent heat cycling to 450°C, followed by rapid cooling, devices withstood the treatment successfully despite the large mismatches in the coefficients of thermal expansion of BPSG and aluminum.

Stress in as-deposited BPSG films is tensile, but considerably less so than CVD SiO_2 or PSG films of the same phosphorus content. As in

the case of CVD SiO_2 and PSG films,[21,49] BPSG films[6] decrease significantly in stress level with storage time or on exposure to humidity, changing toward compressive stress.

4.6 Dielectric Properties and Refractive Index

The dielectric breakdown voltage of 50 large-area (65,000 μm^2) capacitors made from 11,000-Å-thick BPSG type A deposited between 1% Si-aluminum films on oxidized silicon averaged 685 V, with a range of 525 to 729 V. The voltage was applied in a ramped mode at 5 V/sec; the measurements were taken at room temperature in room air. No significant differences in breakdown voltage were found under positive or negative biasing conditions.

The dielectric constant at 1 MHz of as-deposited BPSG type A is typically 3.8, changing to a value of 4.5 after fusion. The dielectric constant of fused BPSG type B is 3.8.

The refractive indices of BPSG films on silicon were measured by ellipsometry at a wavelength of 6328 Å. The indices generally exhibit a relatively large range of values from sample to sample and within wafers. Typical refractive index ranges for the three types of BPSG before or after densification at 700°C vary from 1.45 to 1.47. For comparison, CVD films of PSG or BSG have refractive indices of typically 1.42 to 1.45 for analogous as-deposited films and 1.45 to 1.47 for densified films.[5]

5. Patterning Techniques

Delineation of contact openings in fusion-flowed BPSG layers is readily accomplished by either wet chemical etching or by plasma/reactive ion etching techniques.

Wet chemical etching is carried out by using positive or negative photoresists in conjunction with hexamethyldisilazane adhesion promoting agent and ammonium fluoride-buffered hydrofluoric acid solution. It is possible to attain via walls with sufficiently tapered contours that may not require a glass reflow, as shown in the SEM in Fig. 17. However, a reflow treatment is generally preferable to create a softly rounded edge contour, as shown in the examples of the next section.

Dry etching of photoresist-masked wafers is carried out in several types of commercially available plasma etchers using etchant gas mixtures such as C_2F_6, CHF_3, He, and H_2. Etching rates of several thousand angstroms per minute are attainable. The steep via walls (Fig. 18A) resulting from this process must be tapered by reflowing

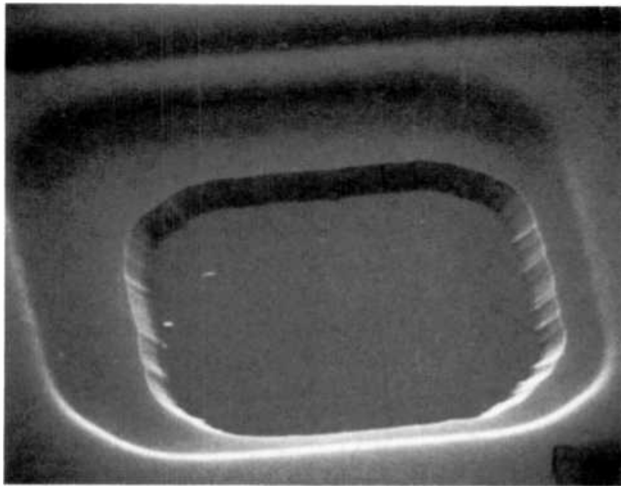

Fig. 17—Contact cut through fused 8,000 Å BPSG type B by chemical etching, not reflowed (SEM 3500×).

the glass under conditions that avoid excessive flow into the exposed contact areas (Fig. 18B).

Patterning of as-deposited BPSG films that may be deposited over aluminum-metallized devices, where no reflow can be applied, is accomplished by wet chemical taper etching techniques.[30,51] Here, a thin, slightly faster etching taper control layer (such as BSG of suitable composition) is deposited over the BPSG. The resulting angle can be predicted from the etch rate relation[52]

$$\theta = \arcsin\left(\frac{R_T}{R_C}\right),$$

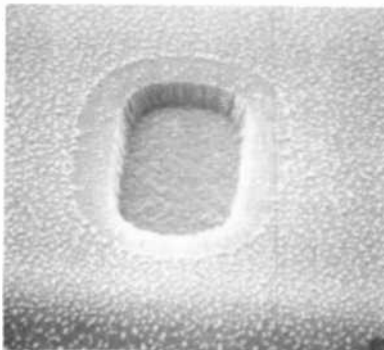

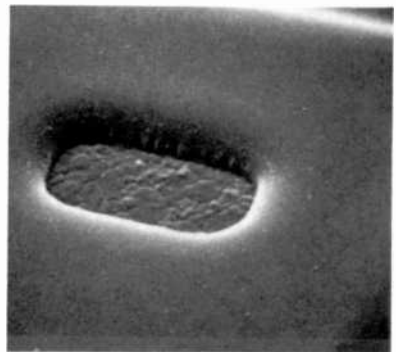

Fig. 18—Contact through 7,000 Å composite of fused BPSG type A over SiO_2 by plasma etching. Resist residue to be removed (A) after etching; (B) after cleaning and fusion reflow. (SEM 5600×).

where R_T is the etch rate of the tapered layer, and R_C is the etch rate of the control layer.

The thickness of the taper control layer is noncritical, but is best kept at about 1500 Å to facilitate deposition control and stripping after use to eliminate the small step formed. Examples of contours achieved by this technique are presented in Fig. 19.

For aluminum-based LSI and VLSI applications where a taper angle steeper than 45° must be attained, plasma etching is simpler to use. Special plasma etching techniques can be applied to produce tapered via walls with rounded edges in a single etching operation.[53]

The removal of photoresist masks after pattern etching of any BPSG film must be done with organic stripping agents, such as Photoresist Stripper A-20 (Allied Chemical Co.) for negative resists and acetone for positive resists. As pointed out in a previous section, the use of hot H_2O-H_2O_2-H_2SO_4 or of H_2O_2-H_2O-NH_4OH should be avoided because of possible leaching effects, especially in the case of undensified films. Extended rinses in hot water should also be avoided for the same reason. Plasma stripping in an oxygen plasma can be used to remove residues from photoresist masking layers. Note that the same considerations hold for PSG and BSG films as well.

6. Applications of BPSG to Silicon Device Fabrication

Borophosphosilicate glass films have been used in or are being considered for use in applications based on four types of properties: (1) lower

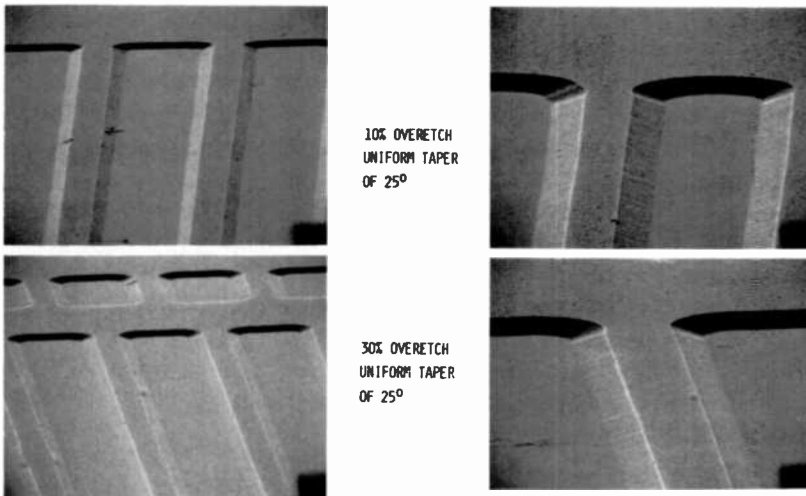

Fig. 19—Etch tapering of BPSG type A by use of a BSG taper control layer (positive resist, BHF; control layer not yet removed; SEM, 85° and 910×, 1820×).

fusion temperature, (2) lower chemical etch rate in ammonium fluoride-buffered hydrofluoric acid solutions, (3) lower as-deposited tensile stress, and (4) lower-temperature doped-oxide diffusion sources.

6.1 Applications for Fusion Tapering

The lower fusion temperature of BPSG films offers a number of significant advantages, including (1) ability to reduce the amount of vertical dopant diffusion that occurs in silicon wafers or lateral diffusion from source and drain regions of MOS ICs during the fusion step; (2) ability to fabricate radiation-hardened devices in which thermally grown SiO_2 is not subjected to excessively high temperature during fusion; (3) ability to reduce crystallographic damage or to avoid reduction in minority carrier lifetime, which could occur during higher temperature processing steps; and (4) reduction in wafer warping and distortion effects. Lower process temperatures are particularly desirable in VLSI/VHSIC applications.

Borophosphosilicate glass is being used by a number of organizations in fabricating silicon-gate MOS ICs in which lower fusion temperature is desirable. Applications have ranged from high-volume production of commercial-grade CMOS RAMs in plastic packages to fabrication of high-speed radiation-hardened silicon-on-sapphire RAMs.

The merits of a lower-temperature fusion glass in fabrication of radiation-hardened ICs have been detailed in several recent papers.[7-9] Examples include a 1 K-bit C^2L RAM[10] (see cover photo) that operates at 10 V up to 5×10^5 Rad(Si), and a 200 K-Rad(Si) 150-nsec 5-V CMOS/SOS 4K RAM.[7] In the SOS radiation-hardened process,[7] the dielectric deposited over polysilicon is flowed at 850°C rather than at 1050°C. Excellent reliability has been obtained on both bulk CMOS[10] and SOS[8,9] static RAMs fabricated by radiation-hardened processes that employ BPSG.

Fused BSPG has also been employed in fabrication of a number of other devices with good results, including developmental high-density RAMs, microprocessors, CCDs, and other advanced silicon-gate devices. Fused BPSG is also applicable to devices with layers of refractory metal or metal silicide layers under the fusable layer. Figs. 20 to 22 provide examples of the application of flowed and/or reflowed BPSG for a number of silicon-gate MOS IC applications. Fig. 23 shows SEMs of a bipolar IC processed with BPSG.

6.2 Use in Low-Etch-Rate Applications

The etch rate of BPSG films in buffered hydrofluoric acid solutions can be comparable to that of undoped SiO_2, and this feature can be

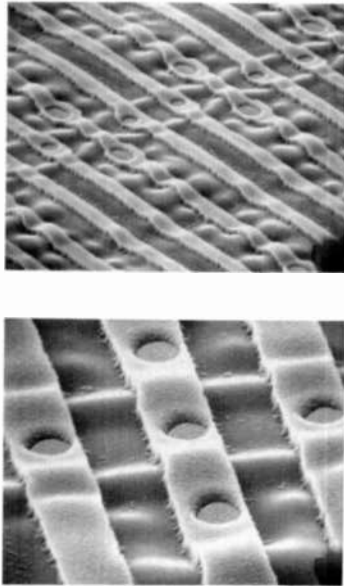

Fig. 20—SEMs of CMOS IC with 7000-Å BPSG type A over oxidized N^+-polysilicon. BPSG was fusion flowed at 950°C in steam to produce a smoothly tapered surface topography. The device wafers were then masked with positive photoresist and etched and reflowed, to round top edges of the via walls. Top metallization is aluminum (Top: 780×; Bottom: 1970×, 65°).

desirable for certain applications.[3] Typical etch rates for as-deposited and densified BPSG films have been listed in Table 4, together with those for SiO_2, BSG, and PSG for comparison.

6.3 Applications as Low-Stress Films

Low-temperature CVD films of SiO_2 tend to be in tensile stress as deposited. The addition of phosphorus oxide or boron oxide to CVD SiO_2 films is known to decrease tensile stress, thus permitting use of relatively thick films on Si without cracking.[24] However, since CVD films with higher phosphorus concentrations can result in Al metal corrosion in plastic-encapsulated devices, the maximum phosphorus content that can be used in low-temperature-deposited (400°C) CVD phosphosilicate glass films over Al metal is approximately 4% P by weight.[21,49,54-56]

Chemical-vapor-deposited BPSG films are in very low tensile stress in the range[6] of 9×10^8 dyne/cm^2 as deposited at 430°C, and thus may be considered for applications in which low stress is desirable.[59] Examples include semiconductor device structures in which very thick

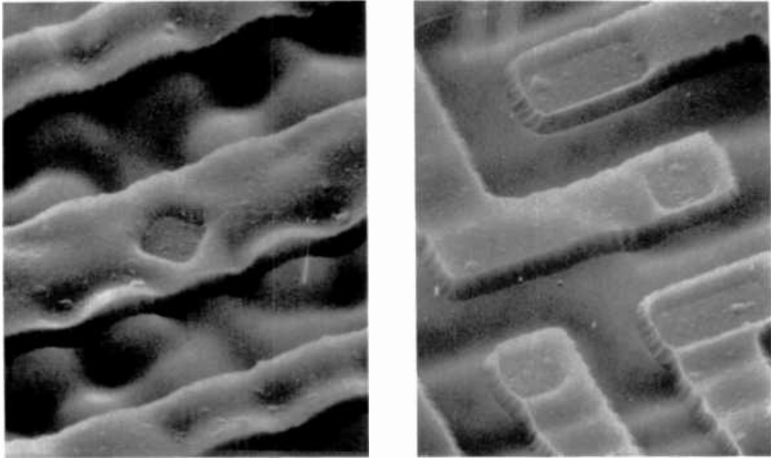

Fig. 21—SEMs showing different areas of an SOS buried-contact IC with 8000-Å BPSG type A on 1000-Å CVD SiO_2: fused 15 min at 950°C in O_2; wet chemically contact-etched; reflowed 15 min at 950°C in O_2; metallized with aluminum; SiO_2 on sapphire substrate is used to enhance bonding of BPSG layer. (1620×).

(>5 μm) dielectric films are used, passivation layers in device structures in which very thick metallization layers (>2 μm) are used, passivation layers over Al metallization in device structures subjected to subsequent high-temperature steps such as frit sealing of packages, and dielectric in devices that are sensitive to piezoelectric effects.

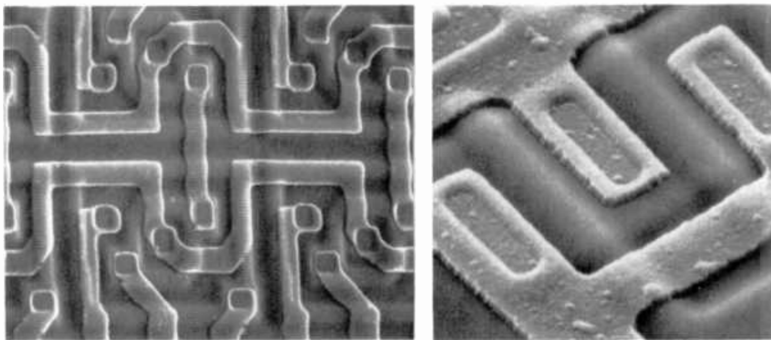

Fig. 22—SEMs of rad-hard C^2L ICs processed with BPSG type B as the fusion-flow layer of 8000-Å thickness. Fusion was done at 850°C in steam. Reflow for edge-tapering of wet-chemically etched via openings was carried out at 850°C in dry N_2/O_2 mixture. Top-level conductor is aluminum. (Left: 500×, 40°; Right: 1000×).

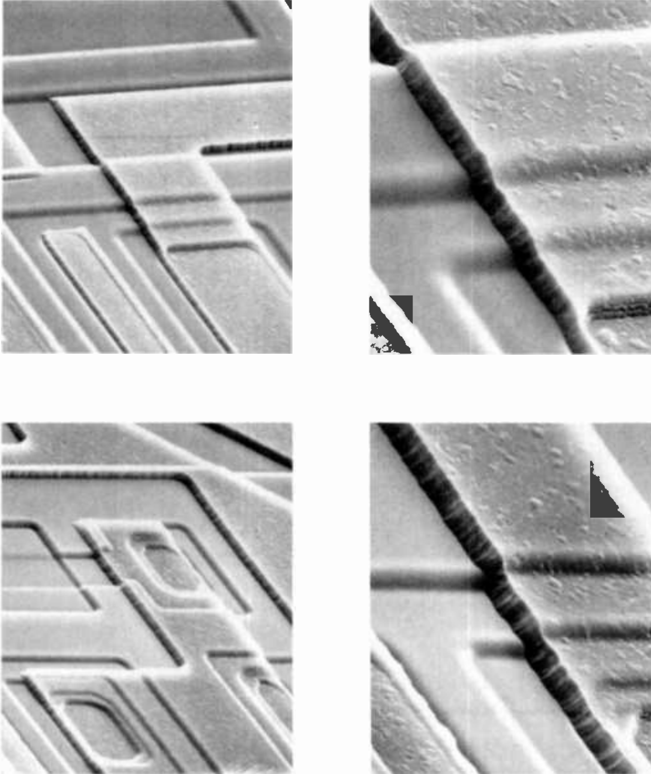

Fig. 23—SEMs of bipolar IC processed experimentally with 7600-Å-thick layer of BPSG type B fusion-flowed in steam at 825°C for 30 min. Reflow at 850°C in dry N_2 for 30 min after wet-chemical contact etching. Cold-deposited aluminum was used as the top-level conductor. (SEMs at 530× and 1580×; top shows contacts closed with oxide during glassing; bottom shows contacts exposed during glassing.)

6.4 Use as Low-Temperature Diffusion Sources

CVD borophosphosilicate glass films can also serve as lower-temperature doped-oxide solid-to-solid diffusion sources. For example, a type A BPSG film, deposited on a 70 ohm-cm p-type wafer and subjected to a 60-min heat treatment at 900°C, produced a 5-ohm/square n-type surface layer. Although the BPSG films are a source of both B and P atoms, the principal dopant in the silicon is P (because of relative differences in the distribution coefficients of the two dopants at the Si-SiO_2 interface). The principal effect of the boron oxide in the glass is to lower the viscosity, thus permitting more phosphorus atoms to reach the Si/SiO_2 interface. A bare silicon wafer adjacent to BPSG in

a furnace will be boron-doped because of the relatively high volatility of boron oxide.

7. Discussion and Conclusions

For over ten years, chemical-vapor deposition based on oxidation of silane has been very widely used in fabrication of silicon devices. Initial use of SiO_2 was followed by use of phosphosilicate glass for over-metal passivation of aluminum-metallized integrated circuits. Shortly thereafter, phosphosilicates were used for fusion flow and/or reflow over silicon-gate MOS integrated circuits. Both applications of phosphosilicate glasses were widely used in the integrated circuit manufacturing industry prior to the appearance of detailed technical papers on chemical vapor deposition of PSG, on properties of thin-film phosphosilicate layers, or on analytical controls for deposited PSG films. Somewhat similarly, borophosphosilicate glass films have been used for several years and are presently in relatively widespread use to achieve lower-temperature flow or reflow glass in silicon-gate MOS integrated circuit manufacture, but detailed technical papers have not appeared prior to 1982.

This paper has surveyed techniques for atmospheric-pressure deposition of BPSG and for analysis of films. Some properties of deposited films have been presented and applications have been outlined. The ternary system B_2O_3-P_2O_5-SiO_2 is obviously more complicated than the binary system P_2O_5-SiO_2, but offers more flexibility, with the possibility of selecting BPSG compositions optimized for specific applications. For example, if an 800°C fusion temperature is desired, a range of glass compositions with different boron and phosphorus contents could be considered. These would have different chemical etch rates, different chemical durability, and would differ in other properties of interest in fabrication of semiconductor devices.

Much work remains to fully characterize the silica-rich borophosphosilicate system. For example, more needs to be known about the corrosion susceptibility[6] of aluminum-metallized devices in the presence of BPSG.

It is predicted that chemical-vapor deposited borophosphosilicate films, because of their significant advantages, will be even more widely used in the future. Moreover, they will be the subject of additional scientific and engineering studies on deposition, topology, composition, properties, analysis, and applications. One large area of application will continue to be to achieve lower-temperature fusion flow. Other applications will be based on lower aqueous chemical etch rates or lower as-deposited intrinsic stress. For applications in which fusion-

flow is not used, techniques other than atmospheric-pressure chemical-vapor deposition will be considered to achieve improved step coverage (plasma-enhanced CVD, photocatalyzed CVD).

Acknowledgments

The authors wish to thank the following persons for their contributions to this project: W. A. Kurylo (experimental CVD and infrared spectroscopy); J. M. Shaw, S. C. Blackstone, and M. Blumenfeld (CVD on large-scale reactor systems); R. E. Berger (chemical etching and instrumental measurements); C. W. Benyon and E. M. Strouse (dielectric measurements); M. T. Duffy and M. F. Leahy (plasma etching); B. Seabury (SEM); E. Botnick, B. Goydish, C. Magee, E. Bertin, and R. Paff (film analyses); D. W. Flatley, S. T. Hsu, S. Policastro, B. Leung, and R. Donnelly for making SEMs of devices processed with BPSG available to us; and N. Goldsmith, J. Shaw, and K. Strater for critically reviewing the manuscript.

References:

[1] W. Kern and R. C. Heim, "Chemical Vapor Deposition of Silicate Glasses for Use with Silicon Devices, I. Deposition Techniques," *J. Electrochem. Soc.*, **117**, p. 562 (1970).

[2] W. Kern, "Silicate Glass Coating of Semiconductor Devices," US Patent 3,481,781, December 2, 1969. (Patent refers to the synthesis of silicate glasses, including BPSG, by chemical vapor deposition from the hydrides.)

[3] C. E. L. Hooker and D. W. Tomes, "Silicon Dioxide Etch Rate Control by Controlled Additions of P_2O_5 and B_2O_3," U.S. Patent 3,913,126, October 14, 1975.

[4] W. Kern and V. S. Ban, "Chemical Vapor Deposition of Inorganic Thin Films," in *Thin Film Processes*, J. L. Vossen and W. Kern, Eds.; Academic Press, New York, 1978, pp. 257–331.

[5] W. Kern, "Chemical Vapor Deposition of Inorganic Glass Films," *Semiconductor International*, **5**, (3), p. 89 (March 1982).

[6] C. Ramiller and L. Yau, "Borophosphosilicate Glass for Low Temperature Reflow," Paper presented at SEMCON/WEST '82, May 25, 1982, San Mateo, CA; Technical Program Proceedings, pp. 29–37.

[7] L. Napoli, R. Smeltzer, J. Yeh, and W. Heagerty, "A 200 KRAD(Si) 150 nsec 5 Volt CMOS/SOS 4K RAM," paper presented at IEEE Annual Conf. on Nuclear and Space Radiation Effects, Las Vegas, NV, July 1982.

[8] J. L. Yeh and R. K. Smeltzer, "A High Density, High Yield, Radiation Hardened, Buried Contact CMOS/SOS Technology," presented as a poster paper at IEEE Annual Conf. on Nuclear and Space Radiation Effects, Las Vegas, NV, July 1982.

[9] H. Veloric, R. Denning, G. Schnable, and J. Yeh, "Reliability of Silicon-On-Sapphire Integrated Circuits," Paper Prepared for Presentation at the 1982 IEEE SOS/SOI Technology Workshop, Provincetown, Mass., October 5, 1982.

[10] L. S. Napoli, R. K. Smeltzer, R. Donnelly, and J. Yeh, "A Radiation Hardened-256 × 4 Bulk CMOS RAM," *RCA Rev.*, **43**, p. 458, Sept. '82.

[11] W. F. Horn and F. A. Hummel, "Notes on the System B_2O_3-SiO_2-P_2O_5: I. The BPO_4-SiO_2 Join," *J. Soc. Glass Technol*, **39**, p. 113T (1955).

[12] W. J. Englert and F. A. Hummel, "Notes on the System B_2O_3-SiO_2-P_2O_5: II. Ternary System," *J. Soc. Glass Technol.*, **39**, p. 121T (1955).

[13] W. F. Horn and F. A. Hummel, "Progress Report on the System BPO_4-SiO_2," *Trans. J. Brit. Ceram. Soc.*, **78**, No. 4, p. 77 (1979).

[14] W. Kern, "Chemical Vapor Deposition Systems for Glass Passivation of Integrated Circuits," *Solid State Technol.* **18,** No. 12, p. 25 (1975).
[15] K. Strater and A. Mayer, "The Oxidation of Silane, Phosphine and Diborane During Deposition of Doped Oxide Diffusion Sources," in *Semiconductor Silicon*, R. R. Haberecht and E. L. Kern, Eds., Electrochem. Soc. Inc., New York, 1969, pp. 469–480.
[16] B. J. Baliga and S. K. Ghandhi, "Growth of Silica and Phosphosilicate Films," *J. Appl. Phys.* **44,** p. 990 (1973).
[17] R. S. Rosler and G. M. Engle, "Plasma Enhanced CVD in a Novel LPCVD-Type System," *Solid State Technol.* **24,** No. 4, p. 172 (1981).
[18] W. Kern and R. S. Rosler, unpublished research results, March 1982.
[19] B. Goydish, "The Quantitative Determination of Boron in Glasses used as Encapsulants for Electronic Devices," *Microchem. Journal* **15,** No. 4, p. 572 (1970).
[20] A. S. Tenney, "Colorimetric Determination of Boron in Aqueous Solutions and in Borosilicate Glass by Solvent Extraction," *J. Electrochem. Soc.* **120,** No. 9, p. 1284 (1973).
[21] W. Kern, R. B. Comizzoli, A. W. Fisher and G. L. Schnable, *Improved CVD Techniques for Depositing Passivation Layers on ICs*, Technical Report AFML-TR-75-160, Oct. 1975, Air Force Matl. Lab., Wright-Patterson AFB, Ohio.
[22] C. Grilletto, "An X-Ray Fluorescence Technique for the Rapid Determination of Phosphorus in PSG Film," *Solid State Technol.*, **20,** No. 2, p. 27 (1977).
[23] W. A. Pliskin, "Comparison of Properties of Dielectric Films Deposited by Various Methods," *J. Vac. Sci. Technol.* **14,** No. 5, p. 1064 (1977).
[24] W. Kern and R. C. Heim, "Chemical Vapor Deposition of Silicate Glasses for Use With Silicon Devices, II. Film Properties," *J. Electrochem. Soc.* **117,** p. 568 (1970).
[25] W. Kern, "Infrared Spectroscopic Method for Compositional Determination of Vapor Deposited Borosilicate Glass Films and Results of Its Application," *RCA Rev.* **32,** No. 3, p. 429 (1971).
[26] A. S. Tenney and M. Ghezzo, "Composition of Phosphosilicate Glass by Infrared Absorption," *J. Electrochem. Soc.* **120,** No. 9, p. 1276 (1973).
[27] W. Kern, "A Technique for Measuring Etch Rates of Dielectric Films," *RCA Rev.* **29,** No. 4, p. 557 (1968).
[28] W. Kern and C. A. Deckert, "Chemical Etching," in *Thin Film Processes*, J. L. Vossen and W. Kern, Eds., Academic Press, New York, 1978; pp. 401–496.
[29] C. T. Naber, "A Technique for Obtaining Tapered Oxide Steps in Silicon-Gate Integrated Circuits," *J. Electrochem. Soc.*, **119** (11), p. 301C, RNP 351 (1972).
[30] W. Kern, J. L. Vossen, and G. L. Schnable, "Improved Reliability of Electron Devices Through Optimized Coverage of Surface Topography," *11th Ann. Proc. Reliab. Phys.*, pp. 214–223 (1973).
[31] J. L. Vossen, G. L. Schnable, and W. Kern, "Processes for Multilevel Metallization," *J. Vac. Sci. Technol.*, **11,** p. 60 (1974).
[32] W. E. Armstrong and D. L. Tolliver, "A Scanning Electron Microscope Investigation of Glass Flow in MOS Integrated Circuit Fabrication," *J. Electrochem. Soc.*, **121,** p. 307 (1974).
[33] P. Balk and J. M. Eldridge, 'Phosphosilicate Glass Stabilization of FET Devices," *Proc. IEEE*, **57,** p. 1558 (1969).
[34] J. M. Eldridge and D. R. Kerr, "Sodium Ion Drift Through Phosphosilicate Glass-SiO_2 Films," *J. Electrochem. Soc.*, **118,** p. 986 (1971).
[35] B. E. Deal, "The Current Understanding of Charges in the Thermally Oxidized Silicon Structure," *J. Electrochem. Soc.*, **121,** p. 198C (June 1974).
[36] E. H. Nicollian and J. R. Brews, *MOS (Metal Oxide Semiconductor) Physics and Technology*, J. Wiley and Sons, New York, 1982, pp. 767–769.
[37] R. H. Dawson and G. L. Schnable, "Passivating Composite for a Semiconductor Device Comprising a Silicon Nitride (Si_3N_4) Layer and Phosphosilicate Glass (PSG) Layer," U.S. Patent 4,273,805; June 16, 1981.
[38] A. C. Adams and C. D. Capio, "Polarization of Phosphorus-Doped Silicon Dioxide," *J. Electrochem. Soc.*, **128,** No. 2, p. 423 (1981).
[39] M. Yamin, "Observations on Phosphorus Stabilized SiO_2 Films," *IEEE Trans. Electron Devices*, **ED-13,** p. 256 (1966).
[40] T. J. Rockett and W. R. Foster, "Phase Relations in the System Boron Oxide-Silica," *J. Amer. Ceram. Soc.*, **48,** p. 75 (1965).

[41] L. D. Pye, V. D. Fréchette, and N. J. Kreidl, Editors, *Borate Glasses: Structure, Properties, Applications*, Plenum Press, New York, N.Y. (1978).
[42] J. R. Van Wazer, *Phosphorus and Its Compounds*, Vol. I: Chemistry, Interscience Publishers, New York, NY., 1958, pp. 550–553.
[43] T.-Y. Tien and F. A. Hummel, "The System SiO_2-P_2O_5," *J. Amer. Ceram. Soc.*, **45**, p. 422 (1962).
[44] K. Takahashi, "Binary Phosphate, Silicophosphate, Borophosphate and Aluminophosphate Glasses, Their Properties and Structure," in *Advances in Glass Technology*, VIth Internatl., Congress on Glass, Washington, D.C., July 1962, Plenum Press, New York, 1962, pp. 366–376.
[45] C. R. Hammond, "Fusion Temperatures of SiO_2-P_2O_5 Binary Glasses," *Phys. and Chem. of Glasses*, **19**, p. 41 (1978).
[46] See, for example:
W. Eitel, "Viscosity of Fused Silicates," in *The Physical Chemistry of the Silicates*, Vol. II, The Univ. of Chicago Press, 1965; pp. 8–66.
R. H. Doremus, "Viscosity," Chapter 6 in *Glass Science*, Wiley-Interscience, New York, N.Y., 1973. pp. 101–114.
W. Eitel, "Viscosity of Molten Glass," in *Glass Science*, Vol. 7, Academic Press, New York, N.Y., 1975.
C. L. Babcock, "Viscosity," Chapter 14 in *Silicate Glass Technology Methods*, John Wiley & Sons, New York, 1977, pp. 222–236.
[47] R. F. Bartholomew, "Water in Glass," in *Treatise on Materials Science and Technology*, Vol. 22, M. Tomozawa and R. H. Doremus, Eds.; Academic Press, New York, 1982, pp. 75–127.
[48] J. C. Mikkelsen, Jr., F. L. Galeener, and W. J. Mosby, "Raman Characterization of Hydroxyl in Fused Silica and Thermally Grown SiO_2," *J. Electronic Materials*, **10**, (4) p. 631 (1981).
[49] G. L. Schnable, W. Kern, and R. B. Comizzoli, "Passivation Coatings on Silicon Devices," *J. Electrochem. Soc.*, **122**, p. 1092 (1975).
[50] W. Kern, G. L. Schnable, and A. W. Fisher, "CVD Glass Films for Passivation of Silicon Devices: Preparation, Composition, and Stress Properties," *RCA Review*, **37**, p. 3 (1976).
[51] L. K. White, "Bilayer Taper Etching of Field Oxides and Passivation Layers," *J. Electrochem. Soc.* **127**, No. 12, p. 2687 (1980).
[52] G. I. Parisi, S. E. Haszko, and G. A. Rozgonyi, "Tapered Windows in SiO_2: The Effect of NH_4F:HF Dilution and Etching Temperature," *J. Electrochem. Soc.*, **124**, No. 6, p. 917 (1977).
[53] M. T. Duffy, RCA Laboratories, private communication.
[54] W. M. Paulson and R. W. Kirk, "The Effects of Phosphorus-Doped Passivation Glass on the Corrosion of Aluminum," 12th Ann. Proc. Reliability Phys., pp. 172–179 (1974).
[55] R. B. Comizzoli, "Aluminum Corrosion in the Presence of Phosphosilicate Glass and Moisture," *RCA Rev.*, **37**, No. 4, p. 483 (1976).
[56] G. L. Schnable, R. B. Comizzoli, W. Kern, and L. K. White, "A Survey of Corrosion Failure Mechanisms in Microelectronic Devices," *RCA Rev.*, **40**, No. 4, p. 416 (1979).
[57] R. B. Comizzoli, L. K. White, W. Kern, and G. L. Schnable, *Corrosion of Metal Films With Defective Surface Protection Layers*, RADC-TR-80-236, Final Techn. Rept., July 1980; Rome Air Development Center, Griffiss Air Force Base, NY.
[58] K. Takahashi, K. Kitajima, and S. Imaoka, "Cracks and Corrosion in PSG Passivation Glass," *Japan. J. Appl. Phys.*, **21**, No. 5, p. 757 (1982).
[59] W. C. Benzing, "Shrinking VLSI Dimensions Demand New Interconnection Materials," *Electronics*, **55**, No. 17, p. 116 (August 25, 1982).

A Radiation Hardened 256×4 Bulk CMOS RAM*

L. S. Napoli and R. K. Smeltzer
RCA Laboratories, Princeton, NJ 08540

R. Donnelly and J. Yeh
RCA Solid State Division, Somerville, NJ 08876

Abstract—A radiation hardened version of the C^2L process has been developed that utilizes all-low-temperature processes subsequent to channel oxidation. This process has been used on 1K RAMS. The RAMs functioned reliably at a dose of 2×10^5 Rad(Si) and failed at a dose of 5×10^5 Rad(Si). The 1K RAM is capable of operating from 7.5 to 12 volts and has an access time from address change of 160 nsec at 10 volts.

Introduction

The radiation hardened C^2L technology discussed in this paper has been described in great detail in an earlier paper by R. E. Stricker.[1] Minor modifications to the process have been made in order to improve yield and reliability. The 1K RAM, which was described in 1979, has been modified to eliminate a system-related pattern-sensitivity problem. The process has been in a manufacturing mode for two years, and data has been collected from 100 lots of 2000 wafers. Of 1276 RAMs sampled from 643 wafers and irradiated to 2×10^5 rads(Si), only 5 failures occurred.

* This work was supported in part by the Jet Propulsion Laboratories in Pasadena, Calif., under Contract No. 954857.

Process Description

The commercial manufacturing process[2] for C^2L includes a silicon gate, has self-aligned sources and drains, and utilizes high-temperature diffusions to dope the gate, source, and drain. It also uses a 1050°C reflow glass to provide a smooth metal step coverage over the interlevel dielectric. The radiation hardened version of C^2L described by Stricker used a channel oxide reduced in thickness from 1000 to 700 Å; the need for high temperature phosphorus and boron diffusions was eliminated by (a) inserting PH_3 in the gas flow during polysilicon deposition and (b) ion implanting sources and drains. No provision was made to smooth the interlevel dielectric for good step coverage. This paper describes results from a revised process that further reduces the channel oxide to 570 Å and replaces the undoped SiO_2 of the interlevel dielectric with a boron and phosphorus doped version (BPSG-B)[3] capable of flowing at 850°C. This allows for smooth contouring of the metal over the poly regions and into the contact cuts. A schematic cross section and a scanning electron micrograph are shown in Figs. 1 and 2.

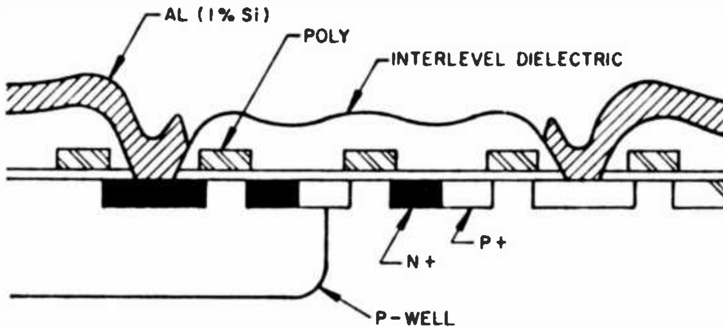

Fig. 1—Cross sectional representation of C^2L wafer.

TCC-244 RAM

The 1K RAM is organized 256 × 4, is identical in pin-out to the CDP 1822, and at 10 volts typically draws less that 1-μA quiescent current. It has an access time of 160 nsec and operates from 7.5 to 12 volts. A system-detected[4] pattern-sensitivity problem, which was later con-

firmed on the J387 Teradyne memory tester, was found to be related to a sagging of the p+ V_{DD} buss in the memory array when rapidly altering between "1" and "0" in the same column of the memory during "read" or "write" operation. The solution, which was to tie the p+ buss to V_{DD} at both ends, eliminated the "false write" problem at normal operating voltage. However, it also prevented writing into the RAM below about 6.5 volts.

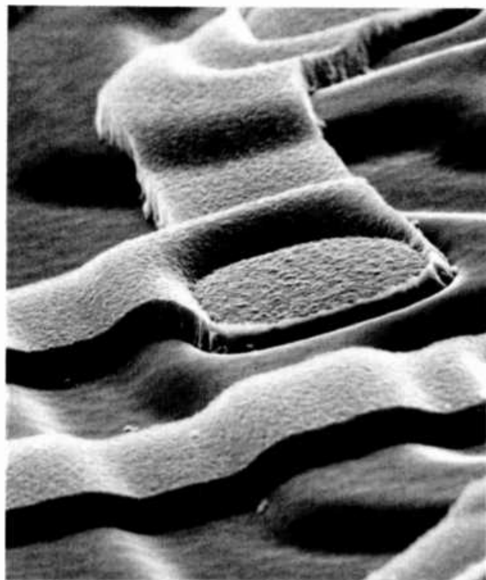

Fig. 2—Scanning electron micrograph showing C^2L topography.

Experimental Results

Based on the threshold voltage behavior with the radiation dose shown in Figs. 3 and 4, the process would produce functioning logic devices out to one megarad (Si). Memory devices, however, are more sensitive to threshold voltage; thus the 1K RAM typically does not function at doses in excess of 5×10^5 rads(Si).

Two variants of the base-line process were examined. One was to deposit undoped LPCVD poly and subsequently dope it in PH_3 for two hours at 850°C. The other was to deposit the interlevel dielectric by introducing CO_2, H_2, and SiH_4 in a flatbed reactor at 950°C. The first was in order to achieve low-resistivity poly at a higher throughput,

and the second was to achieve smooth metal step coverage without the aid of doped oxides. Both variations on the baseline process are acceptable but less desirable than the process described here because of the excessive p-channel threshold voltage shift due to increased temperature and, to a lesser extent, increased time at reduced temperature.

The radiation hardened C^2L process has been running continuously in manufacturing for 5 months, and during that period we have started well in excess of 2000 3-inch wafers. Yield at circuit probe has been good, and hardness to radiation has been consistent and excellent. Of

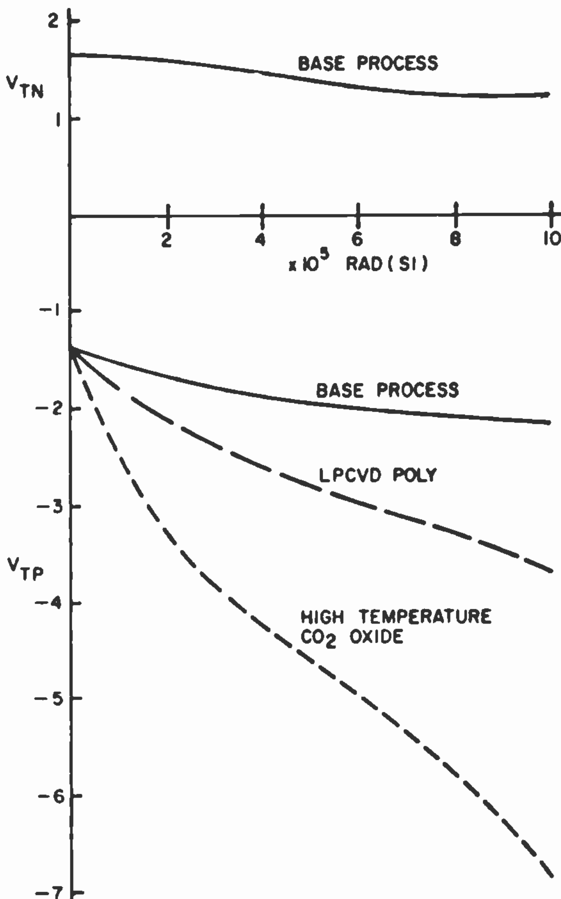

Fig. 3—N-channel and p-channel threshold voltage shift versus total dose radiation with process variation as a parameter.

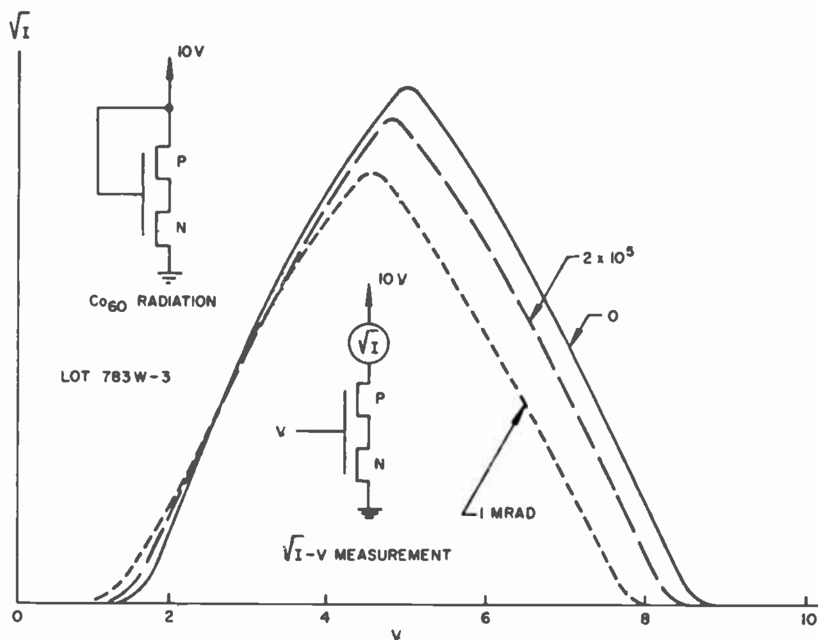

Fig. 4—Family of inverter curves with total dose radiation as a parameter.

Table 1— Pre- and Post-Irradiation Data from ~40 RAMs Sampled from Two-Wafer Lots. All Measurements, As Well As Radiation, Was Done Under 10 Volt DC Bias.

Parameter	Dose in Rads(Si)					Failure Definition
	0		2×10^5		5×10^5*	
TAA (nsec) Access Time	160	+35 −30	165	+35 −30	190	>350
TWW (nsec) Write Pulse	60	+30 −5	85	+30 −5	172	>200
IDN (mA) Output current at 0.5 volts	4.25	+.35 −.45	4.05	+.35 −.45		<2.5
IDP (mA) Output current at 9.5 volts	2.9	+0.2 −0.4	2.85	+0.2 −0.4		<1.5
IDD (μA) Quiescent Current	<1		<1		<1	>200

* A small sample

1276 1K RAMs sampled from 643 wafers, only 5 failed after being subject to a total dose of 2×10^5 rads(Si). None of the five failures were radiation induced. In a few cases, the total dose was brought up to 5×10^5 without failure. Table 1 summarizes typical data from 40 RAMs.

Conclusions

A process has been developed that consistently produces 1K RAMs hard to 2×10^5 Rad with acceptable polysilicon sheet resistance and metal step coverage while minimizing the degradation in radiation hardness. It has been demonstrated that excessive processing time at high temperature or excessive temperature degrades the performance of these devices.

Acknowledgments

The authors acknowledge the superb processing capabilities demonstrated by J. DeCostanzo and F. Hardgrove whose attention to detail resulted in a well-documented and manufacturable process, to V. Giorgio who carefully documented the data and aided in transferring the process successfully to the pilot production line, to W. Kern and J. Shaw who developed and implemented the low temperature glass process, and to J. DiPiazza who made innumerable measurements on irradiated inverters. The authors are grateful to G. Hughes and A. Dingwall for their extremely helpful suggestions and to H. Kressel for the support that was key to the success of this program.

References

[1] R. E. Stricker, A. G. F. Dingwall, S. Cohen, J. R. Adams, and W. C. Slemmer, "A Radiation-Hardened Bulk Si-Gate CMOS Microprocessor Family," NSRE Conference, University of California, Santa Cruz, July 17, 1979.
[2] A. G. F. Dingwall, R. E. Stricker, "C^2L: A New High-Speed, High-Density Bulk CMOS Technology," *IEEE J. of Solid State Circuits*, **SC-12**, No. 4, p. 344, Aug., 1977.
[3] W. Kern and G. L. Schnable, "Chemically Vapor-Deposited Borophosphosilicate Glasses for Silicon Device Application," *RCA Rev.*, **43**, p.423, Sept., 1982 (this issue).
[4] K. Soliman, JPL, Pasadena, California, Private Communication.

Single Sideband, Amplitude Modulated, Satellite Voice Communication System Having 6000 Channels per Transponder

Krishnamurthy Jonnalagadda
RCA Laboratories, Princeton, NJ 08540

Abstract—The use of syllabic compandors and solid-state power amplifiers in satellites makes it possible to transmit about 6000 telephone voice channels using single-sideband amplitude modulation. This high capacity is achievable with presently available technology. This paper shows how the system is designed and how the capacity values are determined, taking into account noise and interference.

1. Introduction

Frequency modulation systems are currently used in satellite communications to transmit frequency division multiplexed (FDM) telephone voice channels. The RCA SATCOM domestic satellite system originally had a capacity of about 1000 channels (half-circuits) in a single FM carrier occupying the full transponder bandwidth of 36 MHz. Use of syllabic compandors[1,2] increased the capacity to about 2000 channels, with the FM carrier continuing to occupy 36-MHz bandwidth.

The Carson's bandwidth of these carriers was made equal to the allocated bandwidth of 36 MHz. Later investigations[1,2] revealed that the Carson's bandwidth can be made larger than 36 MHz with no loss in speech quality and with the allocated bandwidth remaining fixed at 36 MHz. This system, referred to as overdeviated FM, is based on the syllabic compandors providing a subjective advantage not only in the

thermal noise in a channel but also in the baseband intermodulation noise; the latter is due to the filtering of the FM carrier by the satellite and earth station filters. At optimum values of deviation parameters, the overdeviated FM system increased the capacity to 2892 channels.

These capacities were obtained by designing the systems with an average talker level of −15 dBmO, a value that is recommended by the CCIR. Recent studies on speech signal levels in telephone networks[3] have revealed, however, that the average talker level is much lower. If the average talker level is assumed to be −21 dBmO, the overdeviated FM system can increase the capacity to about 3400 channels. Further increases in the capacity are possible by using improved compandors that provide higher subjective noise advantage and by using ideal pre-emphasis and de-emphasis networks. These techniques are not likely to yield capacities of more than 4000 channels (the theoretical limit is 4500 channels) if each channel is allocated a bandwidth of 4 kHz.

The FM systems, being of constant envelope, yield low distortion as the FM signal passes through the satellite amplifier, which has nonlinear gain and phase characteristics. Because of this property, their use is widespread despite the bandwidth expansion inherent in FM. The traveling-wave-tube amplifiers (TWTAs) used in communication satellites have sufficiently degraded nonlinearities that use of an amplitude modulated carrier results in excessive amounts of distortion. Solid state power amplifiers (SSPAs), which have recently been introduced in RCA communication satellites,[4] have much better linearity than TWTAs, and it is therefore possible to employ AM systems and exploit the lower bandwidth (compared to FM) occupied by AM carriers to increase the capacity. A single sideband-amplitude modulated (SSB-AM) system with capacities in excess of 6000 channels is now technically and economically feasible.

The idea of using SSB-AM in satellite communications was first examined in detail in 1964[5] and it was concluded that syllabic compandors with high compression ratios could make SSB-AM feasible. However, the compandors that are commonly available and that have acceptable levels of performance and are economical to use have only 2:1 compression, yielding only 9 to 12 dB net subjective advantage in signal-to-noise ratio (SNR). When these compandors are used with a TWTA, the levels of intermodulation noise generated by the satellite amplifier are sufficiently high to restrict the capacity of the SSB-AM system to less than 4000 channels, as will be shown later. Obviously, improved compandors can give higher capacities, provided either common channel signaling is used or problems related to signaling tones are satisfactorily solved (see Sec. 7).

In the SSB-AM system described here, each voice channel is syllab-

ically companded (using 2:1 ratio compandors) and is frequency division multiplexed with other voice channels. The group of channels thus obtained is translated to the intermediate frequency of 70 MHz through amplitude modulation. Only one of the sidebands generated (upper or lower) is up-converted to rf (6 GHz) and transmitted. Each voice channel is an SSB channel and has an allocated bandwidth of 4 kHz, in which speech occupies only 3 kHz. The theoretical capacity of a transponder of 36-MHz usable bandwidth, then, is 9000 channels. However, due to various transmission impairments, the capacity is restricted to about 6000 channels.

The values of the desired signal-to-noise ratio in each channel are determined in Sec. 2, and the thermal noise and intermodulation noise contributions to each channel are given in Secs. 3 and 4. Sec. 5 contains a detailed analysis of the effects of external interference. In Sec. 6 the SSB-AM capacities are calculated. Finally, in Sec. 7, issues related to signaling tones in each channel are considered.

2. Required SNR in a Voice Channel

A detailed analysis of how a companded system works is given in Ref. [1]. If P_s dBmO is the average power of input speech, the compressor increases this to a value of $P_s + X$ dBmO, where $X = 4$ dB if $P_s = -15$ dBmO and $X = 7$ dB if $P_s = -21$ dBmO. In this paper, we assume that the average speech level $P_s = -21$ dBmO. Companding provides a noise advantage of A dB for speech signals. The value of A for design purposes is 16 dB. Let s be the speech power in a channel at the receiver (expandor input) and n_t be the total noise in a channel. Then, the SNR in a voice channel is s/n_t. The subjectively perceived value of SNR is higher by a factor of $A + w$ dB, where w is the psophometric weighting ($w = 2.5$ dB). If a test tone of 0-dBmO power is introduced into a channel (at the input to the compressor), the received test-tone/noise-power ratio has the subjective value

$$T_T/N = 10 \log(s/n_t) + A + w - (P_s + X) \text{ in dB,} \quad [1]$$

where $P_s + X$ is the speech power at the output of the compressor of 0-dBmO unaffected level.

It should be noted that in deriving Eq. [1] the X dB power increase is exhibited only by speech signals, but not by the 0-dBmO test tone. With $A = 16$ dB, $X = 7$ dB, $P_s = -21$ dB, and $w = 2.5$ dB, Eq. [1] becomes

$$T_T/N = \frac{S}{N} + 32.5 \text{ in dB,} \quad [2]$$

where $S/N = 10 \log(s/n_t)$.

The goal of the SSB-AM system is to provide a value of 50 dB to the subjective T_T/N at all channels, when the noise power n_t is the total value due to thermal noise, intermodulation noise, and external interference. This is equivalent to the requirement that the speech signal-to-noise ratio has the (objective) value of 17.5 dB. If the external interference is excluded, a specification often used[6] is that T_T/N be at least 51.2 dB, i.e., S/N be at least 18.7 dB. Clearly, these values of S/N can be lowered if the compandor provides higher noise advantage than is assumed above.

A detailed account of the contribution of various types of noise is given in Sec. 3, 4, and 5.

3. Thermal Noise

Let the effective isotropic radiated power of the transmit earth station be denoted by EIRP_e. Then the flux density ϕ at the satellite receiver antenna is $\mathrm{EIRP}_e/(4\pi r^2)$, where r is the distance between the earth station and the satellite. The free space loss L_{up} equals $(4\pi r/\lambda)^2$, where λ is the wavelength corresponding to the uplink frequency of 6 GHz. The channel adds noise with flat power spectral density kT_s, where k is Boltzmann's constant and T_s is the effective satellite input noise temperature. The uplink signal-to-noise ratio due to the thermal noise in a channel is

$$(S/N)_{th-up} = \phi + (G_s/T_s) - 10 \log b - 10 \log k + 10 \log(\lambda^2/4\pi) - 10 \log n \text{ in dB,} \quad [3]$$

where ϕ is in dBW/m^2,
- G_s is the satellite receiver antenna gain (dB),
- b is the noise bandwidth (3000 Hz) of a channel,
- n is the number of channels, and
- $10 \log n$ signifies that the desired signal power is distributed equally over n voice channels.

If we define ϕ as the flux density that saturates the satellite amplifier, Eq. [3] reduces to

$$(S/N)_{th-up} = \phi + I_{BO} + (G_s/T_s) - 10 \log n + 156.83 \text{ in dB,} \quad [4]$$

where I_{BO} is the input backoff in dB (negative, if below saturation).

The satellite system parameters used in this paper are shown in Table 1. With these values, the uplink SNR due to thermal noise reduces to

$$(S/N)_{th-up} = 70.83 + I_{BO} - 10 \log n \text{ in dB.} \quad [5]$$

Table 1—Satellite System Parameters

1. Saturating flux density	$= -82.0$ dBW/m^2
2. Satellite G/T	$= -4.0$ dB/K
3. Satellite EIRP	= 36.0 dBW
4. Earth station antenna diameter	= 11.0 to 12.0 m
5. Receive earth station G/T	= 32.4 dB/K
6. Receive earth station antenna gain	= 53.0 dB
7. Transmit earth station antenna gain	= 54.0 dB

It is convenient to define $I_{BO} - 10 \log n$ as the signal power in a voice channel. When referred to the output of the satellite amplifier, this equals $O_{BO} - G_a - 10 \log n$, where G_a is the amplifer gain $O_{BO} - I_{BO}$, and O_{BO} is the output backoff in dB. Then

$$(S/N)_{th-up} = (O_{BO} - 10 \log n) - (G_a - 70.83) \text{ in dB.}$$

The power of the desired signal is denoted by s and that of the thermal noise signal in the uplink by n_{th-up}. Then

$$(S/N)_{th-up} = 10 \log(s/n_{th-up}), \quad [6]$$

$$s = o_{bo}/n, \quad [7]$$

$$n_{th-up} = 10^{-7.083}, \quad [8]$$

where $10 \log o_{bo} = O_{BO}$, $10 \log g_a = G_a$, and $G_a = O_{BO} - I_{BO}$, all in dB.

The downlink SNR, due to thermal noise, can similarly be shown to be (at 4 GHz)

$$\begin{aligned}(S/N)_{th-dn} &= \text{EIRP}_s + O_{BO} - 10 \log k - L_{dn} - 10 \log b \\ &\quad + (G_e/T_e) - 10 \log n, \\ &= \text{EIRP}_s + O_{BO} + (G_e/T_e) - 10 \log n - 2.17 \\ &= 66.23 + O_{BO} - 10 \log n \text{ in dB,}\end{aligned} \quad [9]$$

where EIRP_s is the effective isotropic radiated power of the satellite at full power (in dBW), L_{dn} is the downlink free space loss (in dB), G_e/T_e is the receive earth station G/T value, and the values given in Table 1 are used in deriving the last part of Eq. [9]. This equation can also be written

$$(S/N)_{th-dn} = 10 \log(s/n_{th-dn}) \quad [10]$$

where

$$n_{th-dn} = 10^{-6.623}. \quad [11]$$

The total thermal noise power is denoted by n_{th} and is given by

$$n_{th} = 10^{-7.083} g_a + 10^{-6.623}. \quad [12]$$

The SNR due to the total thermal noise is denoted by

$$(S/N)_{th} = 10 \log(s/n_{th}). \quad [13]$$

4. Intermodulation Noise

The intermodulation (IM) noise generated by the satellite amplifier limits the performance of SSB-AM, restricting the capacity to about 6000 channels. The gain and phase characteristics of a TWTA of the type used in SATCOM I and SATCOM II and of an SSPA of the type described in Ref. [4] are shown in Figs. 1 and 2. The figures show the single carrier input and output characteristics.

The input to the amplifier consists of a large number of voice channels, all of which are assumed to carry speech of the same average

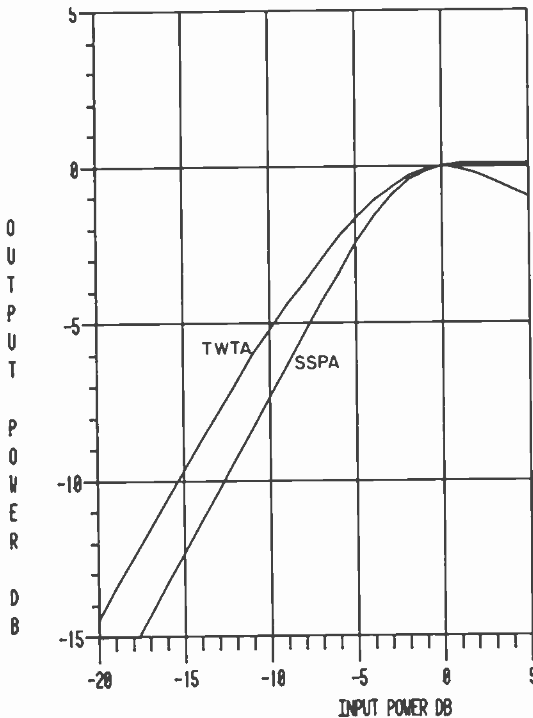

Fig. 1—Gain characteristics of the two amplifiers.

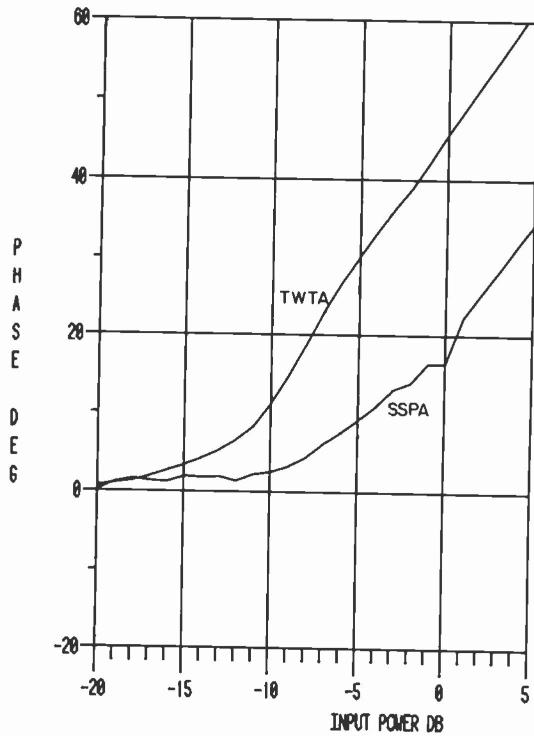

Fig. 2—Phase characteristics of the two amplifiers.

power. The sum of these signals can be approximated by a Gaussian random process of power σ^2. The signal in each channel can be approximated by a sinusoid of random phase and amplitude that can be a constant or a Rayleigh distributed variable, such that the power of the signal is a specified value. The transponder frequency band of 36 MHz is divided into 4-kHz slots, so that there are $m = 9000$ such slots available for placing n voice channels.

Let W be the frequency of the band edge. Then the frequencies of the m 4-kHz slots are $W + k\omega_o$, where $\omega_o = 4$ kHz and $k = 1, 2, \ldots m$. The input to the amplifier is denoted by $s_i(t)$

$$s_i(t) = \sum_{k=1}^{m} A_k \cos[(W + k\omega_o)t + \theta_k]$$

whose power spectral density is the line spectrum,

$$S(\omega) = (\sigma^2/2)[s(\omega) + s(-\omega)].$$

Here

$$s(\omega) \overset{\Delta}{=} \sum_{k=1}^{m} a_k \delta(\omega - k\omega_o - W)$$

$$a_k = \sigma_k^2/\sigma^2, k = 1, 2, \cdots m$$

$$\sigma^2 = \sum_{k=1}^{m} \sigma_k^2$$

and σ_k^2 is the power of kth sinusoid and equals zero if the kth 4-kHz slot is not allocated for a channel.

As all the voice channels are assumed to carry speech of same average power, a_k equals $1/n$ at all the 4-kHz slots that are allocated to the n channels. The Fourier inverse of $s(\omega)$ is denoted by

$$r(\tau)e^{j\psi(\tau)} = \sum_{k=1}^{m} a_k e^{j(W+k\omega_o)\tau}$$

where $r(\tau)$ is real.

It is shown in Ref. [7] that the output of the nonlinear amplifier has the autocorrelation function $R(\tau)$,

$$R(\tau) = \sum_{k=0}^{\infty} G_{2k+1} r^{2k+1}(\tau) \cos \psi(\tau),$$

where $G_{2k+1} = 2 \mid g_k \mid^2/(k + 1)$

$$g_k = \left(\frac{\sigma}{2}\right) \int_0^{\infty} g(A) e^{j\alpha(A)} \frac{A}{\sigma^2} L_k^{(1)} \left(\frac{A^2}{2\sigma^2}\right) f(A)\, dA$$

$$f(A) = \frac{A}{\sigma^2} e^{-A^2/2\sigma^2}$$

$$L_k^{(1)}(x) = \text{generalized Lagurre polynomial}$$
$$= x^{-1} e^x (d/dx)^k (x^{1+k} e^{-x})/k!$$

and $g(A)e^{j\alpha(A)}$ is defined by the input-output relation of the amplifier such that if its input is $A(\tau)\cos[\phi(\tau)]$, the output is $g(A)\cos[\phi + \alpha(A)]$. The input signal has the power σ^2 and this is normalized so that it equals the input backoff value i_{bo}, where

$$i_{bo} = 10^{I_{BO}/10} \qquad [14]$$

and I_{BO} is in dB. Then G_1 is the useful signal power at the output and equals the output backoff value O_{BO}. At the output, desired signal power in a channel consequently equals G_1/n. The constant G_3 represents the total 3rd order intermodulation noise power generated by the amplifier. Higher order intermodulation noise components G_5, G_7,

..., can be neglected, especially for the SSPA, whose nonlinearities are small. The multicarrier gain characteristic (G_1 versus I_{BO}) and the ratio G_1/G_3 are shown in Figs. 3 and 4. As can be seen, the ratio G_1/G_3 is substantially larger in the SSPA than in the TWTA. The values of G_1 and G_3 are also given in Table 2.

The constant G_3 gives the total 3rd order intermodulation noise at the output. To obtain this noise power in a single SSB-AM voice channel, the spectrum of the intermodulation noise is required. This is obtained by expanding $r^3(\tau)\cos\psi(\tau)$ into its Fourier series. To obtain the series, it is seen that $r(\tau)\exp[j\psi(\tau)]$ can be written as $\sum_{k=1}^{m} a_k z^k$, where $z^k = \exp[j(W + k\omega_o)\tau]$. Then

$$r^3(\tau)\exp[j\psi(\tau)] = \left| \sum_{k=1}^{m} a_k z^k \right|^2 \sum_{k=1}^{m} a_k z^k$$

$$= \sum_{k=2-m}^{2m-1} \mathrm{IM}^k z^k$$

where IM_k is the coefficient of z^k in the expansion

$$\left(\sum_{i=1}^{m} a_i z^i \right)^2 \sum_{i=1}^{m} a_i z^{-i} = \sum_{k=2-m}^{2m-1} \mathrm{IM}_k z^k, \qquad [15]$$

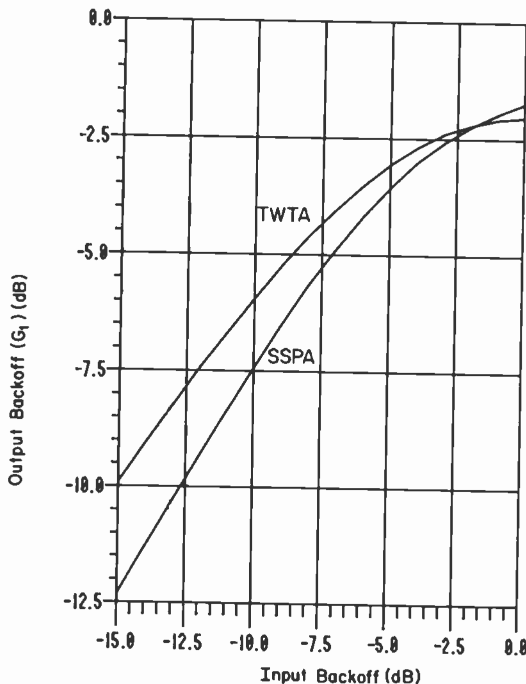

Fig. 3—Multicarrier gain characteristics of the two amplifiers.

Table 2—Amplitude Data (I_{BO} = Input Backoff, G_1 = Output Backoff, and G_3 = Total 3rd Order Intermodulation Power, All in dB)

	TWTA		SSPA	
I_{BO}	G_1	G_3	G_1	G_3
0.0	−2.04	−10.50	−1.76	−11.77
−1.00	−2.09	−11.08	−1.97	−12.59
−2.00	−2.22	−11.80	−2.25	−13.65
−3.00	−2.42	−12.68	−2.60	−15.00
−4.00	−2.71	−13.68	−3.03	−16.67
−5.00	−3.07	−14.78	−3.56	−18.68
−6.00	−3.52	−15.91	−4.18	−21.01
−7.00	−4.04	−17.05	−4.88	−23.57
−8.00	−4.62	−18.17	−5.67	−26.21
−9.00	−5.26	−19.29	−6.52	−28.78
−10.00	−5.95	−20.48	−7.43	−31.28
−11.00	−6.68	−21.83	−8.37	−33.84
−12.00	−7.44	−23.42	−9.34	−36.61
−13.00	−8.24	−25.32	−10.32	−39.70
−14.00	−9.06	−27.57	−11.31	−43.05
−15.00	−9.92	−30.14	−12.31	−46.44

and W is taken to be zero to determine IM_k. It is then seen that

$$r^3(\tau)\cos\psi(\tau) = \sum_{i=2-m}^{2m-1} \mathrm{IM}_i \cos[(W + i\omega_o)\tau].$$

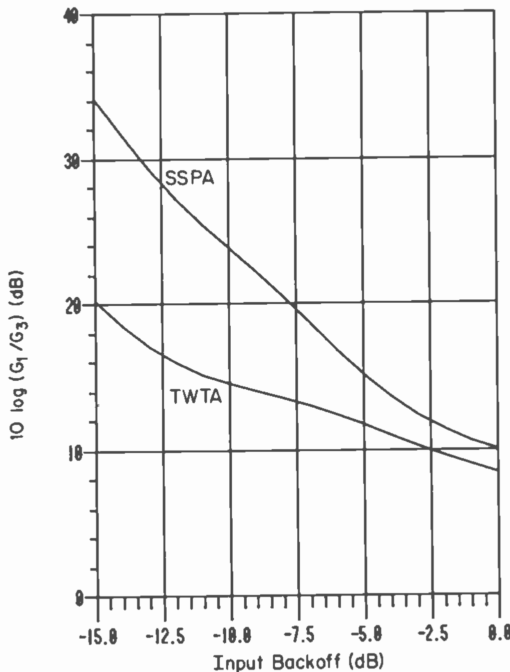

Fig. 4—Ratio of the useful output power to the total 3rd-order intermodulation power.

The intermodulation noise power at the kth 4-kHz slot is given by G_3 IM_k, $k = 1, 2, \cdots m$. However, the speech signal in the 4-kHz slot occupies only 3 kHz, so that the intermodulation power of interest is only 0.75 G_3 IM_k. The SNR due to the intermodulation noise in the voice channel located at the kth 4-kHz slot is

$$S/\mathrm{IM} = 10 \log[G_1/(0.75nG_3\mathrm{IM}_k)] \text{ in dB.} \qquad [16]$$

The noise component has the power

$$n_{im} = 0.75G_3\mathrm{IM}_k. \qquad [17]$$

The value of IM_k is obtained from Eq. [15] using discrete convolutions of the vector $(a_1, a_2, \ldots a_m)$. This vector contains 9000 elements and this leads to a computational problem. A good approximation is to treat blocks of channels (e.g., 60 channels per block) as generating a single sinusoid. These blocks of channels are referred to here as super groups. This reduces the vector size to 150. It is also convenient from a practical point of view to use full super groups (i.e., either all or none of the channels in the super group allocated for the voice signals) in frequency division multiplexing. In assigning channel frequencies, therefore, Eq. [15] is modified by choosing $a_i' = 60/n$, i.e., $1/n'$, with $n' \triangleq n/60$. The number of super groups is n', and the number of super-group slots available in the 36 MHz is $m' = 150$. Then, the coefficients I_k in the following equation are easily determined,

$$\left(\sum_{i=1}^{m'} a_i'Z^i\right)^2 \left(\sum_{i=1}^{m'} a_i'Z^{-i}\right) = \sum_{k=2-m'}^{2m'-1} I_k Z^k, \qquad [18]$$

with

$$Z^k \triangleq \exp[jk60\omega_o\tau].$$

The approximated values of the intermodulation power in m 4-kHz slots are given by

$$\mathrm{IM}_i' = I_k/60, \; i = 1, 2, \ldots m \qquad [19]$$

where k is the integer that yields $(k - 1)60 < i \leq k60$.

The error made in using IM′ in place of IM in Eqs. [16] and [17] is small, as explained in Appendix 1. All the results in this paper are obtained by using this super-group approximation.

The average power of the voice signals in all the channels is the same. It is then desirable that the intermodulation powers also be the same in all the channels. The required uniform spectral density can be closely approximated by putting channels more densely at band edges than at the center. Such a channel assignment is described in Appendix 2, and is the staggered cosine rule given in Ref. [8]. This rule, as well as an iterative technique described later, will make approximately

66.6% of the total intermodulation noise fall inside the frequency band of the transponder. The power spectral density inside the frequency band then is $0.666G_3/36.0$ per MHz. The noise power in one channel of 3-kHz width is

$$n^*_{im} = 0.003(0.666G_3/36.0). \qquad [20]$$

It will be demonstrated later that this simple expression gives values of the capacity of SSB-AM that are very close to those obtained by using the more exact expression of n_{im} given by Eq. [17].

5. External Interference

Terrestrial interference is obtained when terrestrial microwave channels use the same frequency as that of the satellite transponder under consideration. Generally, the interference consists of two strong carriers located at ±10 MHz with respect to the center of the transponder. Consequently, the two frequency bands, −9.25 to −10.75 MHz and 9.25 to 10.75 MHz, are not used for SSB-AM voice channels. In the remaining part of the transponder frequency band, the terrestrial interference is ignored.

Interference also comes from those adjacent transponders of the satellite that are cross-polarized with respect to the desired transponder and that occupy a portion of the desired transponder frequency band. The amount of interference depends on the cross-polarization isolation and the nature of the signals carried by the adjacent transponders. It is assumed that this interference is 26 dB below the carrier power in the desired transponder. If the interference is worse than this value, coordination among the traffic carried by the transponders is necessary to make the interference acceptably low.

External interference from adjacent satellite systems makes the center of the transponder (−1.0 to 1.0 MHz) unusable for SSB-AM. This 2-MHz-wide region is also excluded for SSB-AM signals. The maximum capacity possible with SSB-AM, therefore, is about 7860 channels.

Outside these bands, interference from adjacent satellite systems needs careful attention. We will consider a five-satellite interference model where the satellites are uniformly spaced on the geosynchronous orbit at $D°$ spacing and in which the satellite at the center is the desired satellite and the other four act as interfering systems. First consider the effect of one interfering system, whose satellite is located $D°$ away from the desired satellite. We assume that three transponders of the interfering satellite have frequencies that overlap the frequency band of the desired satellite transponder under consideration. The

center frequency of one of the three coincides with the center frequency of the desired transponder; this will be referred to as the co-frequency interfering transponder. The other two interfering transponders have their center frequencies offset by ±20 MHz from the center frequency of the desired transponder; these will be referred to as offset-frequency transponders. The 18-MHz-wide frequency band to the left or right of the center frequency of the offset-frequency transponders overlaps the desired transponder frequency band. Let the signals carried by these three interfering transponders have power spectral densities $i_1(f)$, $i_2(f)$, and $i_3(f)$ per Hz, where i_1 refers to the co-frequency transponder, and i_2 and i_3 refer to the offset-frequency transponders. The functions $i_1(f)$, $i_2(f)$. and $i_3(f)$ are normalized such that total signal power $\int i(f)\, df$ is unity (or 0 dB), where $i(f) = i_1(f)$, $i_2(f)$, and $i_3(f)$.

Signals from earth stations intended for the interfering satellite are also received by the desired satellite as interference. The SNR due to a single interference component in the uplink can be obtained as follows. Let $EIRP_i$ be the effective isotropic radiated power from the transmit (interfering) earth station, and let G_{ti} be the transmitter gain on axis. Then $EIRP_i - G_{ti}$ is the transmitter power in dBW. The transmitted signals are intended for the interfering satellite that is $D°$ away from the desired satellite. The interference power emitted by the earth station is $EIRP_i - G_{ti} + 32 - 25 \log D$, dBW, where $32 - 25 \log D$ represents the maximum antenna gain allowed at $D°$ off-axis. This interference has an uplink loss of $L_{up(i)}$ dB and is amplified by the desired satellite receiver antenna by a factor of $G_{s(i)}$ dB. The interference signal has a power spectral density of $i(f)$ per Hz at frequency f. Then, the interference power in a frequency band of 3 kHz, centered at f, is given by

$$E(f) = EIRP_i - G_{ti} + 32 - 25 \log D - L_{up(i)} + G_{si} + I(f) + 10 \log 3000, \text{ dBW/3 kHz}$$

where $I(f) = 10 \log i(f)$ and it is assumed that $I(f)$ is constant in the 3-kHz band.

In the same 3-kHz band, the desired (voice) signal has the power $EIRP_e - L_{up} + G_s + O_{BO} - G_a - 10 \log n$, dBW/3 kHz. Assuming that all the satellite systems and earth stations are identical, the SNR due to one interference signal is

$$(S/I)_{up} = O_{BO} - 10 \log n - G_a - 32 + 25 \log D + G_{ti} - I(f) - 10 \log 3000, \text{ in dB}$$

where it is assumed that $EIRP_i = EIRP_e$, $G_s = G_{si}$, and $L_{up} = L_{up(i)}$. Further, assuming the parameters given in Table 1 and $D = 4°$, the

above expression becomes

$$(S/I)_{up} = O_{BO} - 10 \log n - [G_a + I(f) - 2.28] \text{ in dB}.$$

The term $O_{BO} - 10 \log n$ is the signal power at the output of the satellite amplifier. The interference component at frequency f has the power

$$e_{up}(f) = 10^{-0.228} g_a i(f).$$

This is interference power if the earth station is transmitting signals that have the same polarization as that of the desired transponder signals. If they are cross-polarized, $(S/I)_{up}$ increases by P dB, where P is taken to be 10 dB. The value of $e_{up}(f)$ then is

$$e_{up}(f) = 10^{-0.228} g_a p i(f),$$

where $p = 1$ if the desired and interfering signals are copolarized and $p = 0.1$ if they are cross-polarized.

As mentioned earlier, the satellite that is $D°$ away receives three interference components, the sum of which gives

$$e_{up}(f) = 10^{-0.228} g_a [p_1 i_1(f) + p_2 i_2(f) + p_3 i_3(f)],$$

where $p_1 = 1.0, p_2 = 0.1, p_3 = 0.1$ or $p_1 = 0.1, p_2 = 1.0, p_3 = 1.0$ depending on whether the co-frequency transponder is copolarized or cross-polarized.

Similarly the satellite that is $D°$ away, but on the other side of the center (desired) satellite generates three more components: $p_k i_k(f)$, where $k = 4, 5, 6$, with $p_3 = 1.0, p_4 = p_5 = 0.1$ or $p_3 = 0.1, p_4 = p_5 = 1.0$. The combined interference due to the two satellites that are $D°$ away is

$$e_{up}(f) = 10^{-0.228} g_a \sum_{k=1}^{6} p_k i_k(f).$$

There are six more components produced by the two satellites that are $2D°$ away from the desired satellite. When these are also included, the total uplink interference power at frequency f is

$$e_{up}(f) = g_a \left[10^{-0.228} \sum_{k=1}^{6} p_k i_k(f) + 10^{-0.98} \sum_{k=7}^{12} p_k i_k(f) \right]. \quad [21]$$

The downlink equations are similarly obtained with G_{ti} replaced by the receive earth station antenna gain and g_a equal to unity. Assuming that the polarization in the downlink is of the same type as the uplink,

$$e_{dn}(f) = 10^{-0.128} \sum_{k=1}^{6} p_k i_k(f) + 10^{-1.08} \sum_{k=7}^{12} p_k i_k(f). \quad [22]$$

Adding the uplink and downlink interference components, we find that

the total external interference has the power

$$e(f) = (g_a 10^{-0.228} + 10^{-0.128}) \sum_{k=1}^{6} p_k i_k(f) + (g_a 10^{-0.98} + 10^{-1.08}) \sum_{k=7}^{12} p_k i_k(f). \quad [23]$$

As mentioned earlier, the desired signal has the power o_{bo}/n. The SNR due to the external interference is then given by

$$S/I = 10 \log\{o_{bo}/[ne(f)]\}. \quad [24]$$

Clearly S/I depends on the frequency at which the voice channel is located and on the spectra $i_k(f)$, $k = 1, 2, \ldots 12$. We will consider four types of signal spectra for $i(f)$; $i(f)$ is any one of $i_1(f), i_2(f), \ldots i_{12}(f)$. The four spectra are described in Appendix 3 and correspond to TV signals, wideband digital carrier, single-carrier FDM/FM, and two-carrier FDM/FM. All the resulting 4^{12} combinations can give different values for $e(f)$. However, we will consider only the 16 cases obtained under the assumption that all the co-frequency transponders of the interfering satellites carry the same type of traffic and all the offset-frequency transponders carry the same type of traffic. Denoting these by $i_c(f)$ and $i_o(f)$, we arrive at

$$\begin{aligned} e(f) = (g_a 10^{-0.228} + 10^{-0.128})[&i_c(f)(p_1 + p_4) + i_{01}(f)(p_2 + p_5) \\ &+ i_{02}(f)(p_3 + p_6)] \\ &+ (g_a 10^{-0.98} + 10^{-1.08})[i_c(f)(p_7 + p_{10}) + i_{01}(f)(p_8 + p_{11}) \\ &+ i_{02}(f)(p_9 + p_{12})], \end{aligned}$$

where $i_{01}(f)$ is the spectrum of the signal in the −20-MHz offset transponders and $i_{02}(f)$ is the spectrum in the +20-MHz offset transponders. To simplify the model even further, it is assumed that all the interfering satellites have the same polarization plan with respect to the desired satellite. It should be also be noted that the spectrum of $i_{01}(f)$ is zero in the right half of the desired transponder, and that $i_{02}(f)$ is zero in the left half of the desired transponder. In addition, the spectra considered in Appendix 3 are all symmetric about their center. The final expression for $e(f)$ then reduces to

$$\begin{aligned} e(f) = 2[&g_a(10^{-0.228} + 10^{-0.98}) + 10^{-0.128} + 10^{-1.08}] \\ &[qi_c(f) + 0.1 i_o(20 - |f|)/q] \end{aligned} \quad [25]$$

where f is with respect to the center of the transponder, $i_c(f)$ and $i_o(f)$ are functions that are symmetric about zero, $20 - |f|$ is due to the fact that $i_o(f)$ is the spectrum in the offset-frequency transponder, and q is

1 if the desired and co-frequency transponders are copolarized and 0.1 if they are cross-polarized.

The SNR component due to this interference is given by Eq. [24]. The combined noise power due to thermal noise, intermodulation, external interference and adjacent transponders (in the desired satellite) is given by

$$n_t = n_{th-up} + n_{th-dn} + n_{im} + e(f) + n_p, \qquad [26]$$

where n_p is the power of interference generated by cross-polarized adjacent transponders of the desired satellite, and is given by

$$10 \log(s/n_p) = 26.0.$$

The SNR due to all the noise components is

$$S/N = 10 \log(s/n_t),$$

where $s = o_{bo}/n$.

6. Channel Capacities of SSB-AM

First we consider SSB-AM capacities obtained by ignoring external interference and letting SNR at each channel be at least 18.7 dB (i.e., T_T/N is at least 51.2 dB). The thermal noise components have powers n_{th-up} and n_{th-dn} given by Eqs. [8] and [11]. The intermodulation noise power is given by n_{im} (Eq. [17]) or by n^*_{im} (Eq. [20]). The capacities are shown in Table 3. It is seen that the TWTA gives less than 4000-channel capacity, but the SSPA can give about 7100 channels. The capacities are nearly the same whether the expression n_{im} or n^*_{im} is used for the intermodulation noise power in a channel. The channel frequencies can be assigned by using either the staggered cosine rule (Appendix 2), or by using an iterative technique, called "drop" algorithm.

In the drop algorithm, it is initially assumed that all the 150 super

Table 3—SSB-AM Capacities Ignoring External Interference. SNR in Each Channel Is At Least 18.7 dB (Subjective T_T/N = 51.2 dB).

	I_{bo}(dB)				
Amplifier	−6.0	−7.0	−8.0	−9.0	Comment
TWTA	3314	3552	3676	3688	IM power determined by using uniform approx.
SSPA	6409	7102	7135	6560	IM power determined by using uniform approx.
SSPA	6480	7040	7078	6564	Channel assignment using staggered cosine rule
SSPA	6480	7020	7080	6540	Channel assignment using iterative procedure

group slots are allocated for channels, and the SNR values at all the channels are determined. The super group with the lowest SNR value is then dropped. The computations are then repeated with 149 super groups. The iterations are continued, dropping the super group in the most undesirable frequency locations, until the SNR at worst channel location has the specified value. Results shown in Table 3 indicate that the capacity values are virtually the same as those obtained by using the staggered cosine rule. However, if the external interference is included in the computations and if its magnitude is comparable to or worse than the intermodulation noise, the drop algorithm gives higher capacities than the staggered cosine rule.

Consider now the effect of external interference. The required minimum value of SNR is decreased to 17.5 dB. A value of satellite spacing and input backoff is assumed. The total noise power is given by Eq. [26], in which $e(f)$ depends on the signal spectra in co-frequency and offset-frequency transponders, each of which can take one of four possibilities (Appendix 3). In all sixteen cases, the drop algorithm is used to determine the capacities with the channel frequency assignment, avoiding the high interference regions around the center frequency ±10 MHz. Table 4 shows the results of a typical calculation. The worst capacity value will be referred to as due to the "least favorable interference," and the highest capacity value will be referred to as due to the "most favorable interference." Table 5 shows the capacities at 4° and 3° spacing and I_{BO} = −6 to −9 dB. The highest

Table 4—SSB-AM Capacities (Sample Results): Solid-State Power Amplifier; Satellite Spacing, 4.0°; Input Backoff, −7.0 dB; Adjacent Satellite Co-frequency Transponders Co-polarized.

Traffic Co-freq.	Traffic Offset	S/TH[1]	S/Intf[2]	S/IM[3]	S/N[4]	Exact Capacity	Approx. Capacity
1-FM	1-FM	21.33	22.36	23.53	17.54	6420	6300
1-FM	DIG.	21.33	22.28	23.53	17.52	6420	6300
1-FM	TV	21.33	22.36	23.53	17.54	6420	6300
1-FM	2-FM	21.33	22.36	23.53	17.54	6420	6300
DIG.	1-FM	20.65	24.92	22.27	17.51	7500	7500
DIG.	DIG.	20.69	24.74	22.36	17.52	7440	7560
DIG.	TV	20.69	24.53	22.51	17.53	7440	7440
DIG.	2-FM	20.72	24.44	22.45	17.51	7380	7260
TV	1-FM	20.98	23.45	22.80	17.51	6960	6900
TV	DIG.	21.01	23.35	22.88	17.52	6900	6900
TV	TV	21.01	23.49	22.75	17.52	6900	6840
TV	2-FM	21.09	23.56	22.64	17.54	6780	6720
2-FM	1-FM	21.37	22.49	23.31	17.54	6360	6300
2-FM	DIG.	21.37	22.38	23.31	17.51	6360	6300
2-FM	TV	21.41	22.18	23.79	17.58	6300	6240
2-FM	2-FM	21.41	22.06	23.79	17.54	6300	6180

[1] S/TH: Signal-to-thermal-noise ratio, dB
[2] S/Intf: Signal-to-interference ratio, dB
[3] S/IM: Signal-to-intermodulation ratio, dB
[4] S/N: Signal-to-total-noise ratio, dB

Table 5—SSB-AM Capacities: Solid-State Power Amplifier; Satellite Spacing, 4° and 3°; Input Backoff, −6.0 to 9.0 dB; Adjacent Satellite Co-frequency Transponders Co-polarized.

Interference	Spacing	I_{BO}	S/TH	S/Intf	S/IM	Exact Capacity	Approx. Capacity
Least favorable	4.0	−6.0	22.26	23.35	21.51	6240	6180
Most favorable	4.0	−6.0	21.71	25.59	20.84	7080	7020
Least favorable	4.0	−7.0	21.41	22.06	23.79	6300	6180
Most favorable	4.0	−7.0	20.65	24.92	22.27	7500	7560
Least favorable	4.0	−8.0	20.67	22.15	25.28	6120	6060
Most favorable	4.0	−8.0	19.86	24.51	24.25	7380	7380
Least favorable	4.0	−9.0	20.07	22.68	27.55	5700	5700
Most favorable	4.0	−9.0	19.32	24.33	26.24	6780	6720
Least favorable	3.0	−6.0	22.70	22.54	21.75	5640	5640
Most favorable	3.0	−6.0	21.98	24.13	21.24	6660	6480
Least favorable	3.0	−7.0	21.84	21.83	23.43	5700	5700
Most favorable	3.0	−7.0	21.01	23.40	22.79	6900	6780
Least favorable	3.0	−8.0	21.21	21.33	25.51	5400	5400
Most favorable	3.0	−8.0	20.34	22.50	25.41	6600	6540
Least favorable	3.0	−9.0	20.82	21.19	27.45	4800	4860
Most favorable	3.0	−9.0	19.94	22.40	27.50	5880	5880

capacity with least favorable interference is 6300 at 4° spacing and 5700 at 3° spacing. The highest capacity with most favorable interference is 7500 at 4° spacing and 6900 at 3° spacing. It is thus seen that with traffic coordination among the satellite systems, a capacity of 6900 channels is realizable; with no traffic coordination, the capacity is about 6000 channels, if a few of the extreme interference conditions are excluded. Table 5 also shows the capacity values obtained by a

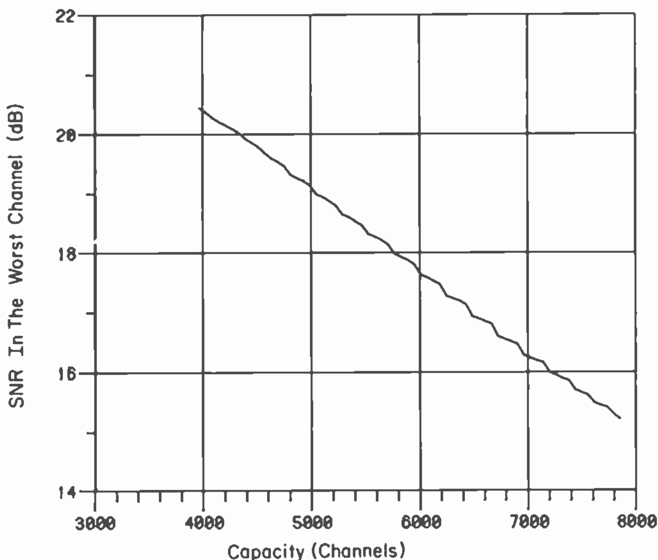

Fig. 5—SNR in the worst channel as a function of capacity: SSPA; I_{BO} = −8 dB; spacing = 4 degrees; 2-FM carriers in all the interfering transponders.

substantially simpler procedure that involves using the constant intermodulation power approximation of Eq. [20]. Then the dependence of SNR on frequency is only through Eq. [25] for $e(f)$. It is thus possible to determine frequency regions in which SNR is at least 17.5 dB, with the capacity given by the number of channels that fit into those frequency regions. This approximate procedure yields virtually the same capacity values obtained by the more exact procedure.

Fig. 5 shows a typical curve of the SNR value at the worst channel as a function of the capacity. The capacity that yields SNR = 17.5 dB is 6120 channels. Fig. 6 shows the values of SNR in all the super groups and where the super groups are located in the frequency band of the transponder.

All the computations made so far assume that the net compandor advantage is 9 dB. The compandor advantage that can give the full capacity of 7860 channel is only 2 to 4 dB higher. Tables 6 and 7 show the compandor advantages required for full capacity when the satellite power amplifier is the TWTA and the SSPA.

7. Effect of Signaling Tones

The highest capacity values of Table 5 are obtained at the optimum values of the I_{BO} and under the assumption that all the channels carry

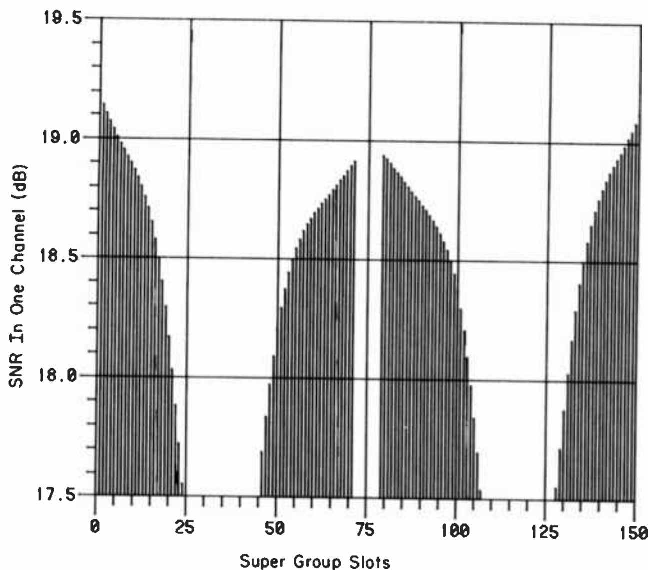

Fig. 6—Variation of SNR as a function of super group position: SSPA; I_{BO} = −8; spacing = 4 degrees; 2−FM carriers in all interfering transponders; capacity = 6120 channels.

Table 6—Compander Advantage (dB) Needed for 7860 Channel Capacity Using SSPA (Net Value That Takes Into Account Increase in Signal Power at Compressor Output) (Adjacent Satellite Co-frequency Transponders Co-polarized)

	Compander Advantage Needed (dB)			
Interference Condition	$I_{BO} = -6.0$	$=-7.0$	$=-8.0$	$=-9.0$
Spacing: 4°				
Least Favorable	10.83	10.91	11.30	11.91
Most Favorable	9.59	9.21	9.28	9.66
Spacing: 3°				
Least Favorable	12.18	12.47	13.00	13.73
Most Favorable	9.90	9.65	9.79	10.29

speech of average power −14 dBmO (at the output of a 0-dBmO unaffected level compressor). The implicit assumption is that the signaling information is conveyed to the receiver using common channel signaling. In RCA SATCOM telephone circuits, however, the idle/busy state of a channel is conveyed to the receiver using in-band single frequency (SF) tones. In the idle state, a continuous SF tone of power −20 dBmO (before compression) is present in the channel. At the output of the compressor the SF tone power is −10 dBmO, and this is 4 dB higher than the average speech level. Consequently, the level of these tones should be reduced to at least that of average speech so that the SSB-AM has a capacity of, say, 6000 channels.

There is, however, a more serious problem due to the generation of the intermodulation noise by the satellite amplifier. Consider the nature of the intermodulation noise produced in a channel (referred to here as the "test" channel) by the other channels. If all the other channels carry speech, the intermodulation noise in the test channel is distributed, nearly uniformly, in the 4-kHz band of the test channel. If all the other channels are idle, they carry SF tones, and hence the (3rd order) intermodulation noise is concentrated as a tone in the test channel. This tone intermodulation (at 2600 Hz) is more annoying to the listener than the spectrally distributed intermodulation noise.

Table 7—Compander Advantage (dB) Needed for 7860 Channel Capacity Using TWTA (Net Value That Takes Into Account Increase in Signal Power at Compresser Output) (Adjacent Satellite Co-frequency Transponders Co-polarized)

	Compander Advantage Needed (dB)			
Interference Condition	$I_{BO} = -6.0$	$=-7.0$	$=-8.0$	$=-9.0$
Spacing: 4°				
Least Favorable	12.20	12.59	12.71	12.96
Most Favorable	12.71	11.94	11.82	11.84
Spacing: 3°				
Least Favorable	13.49	13.61	13.87	14.27
Most Favorable	12.36	12.14	12.07	12.14

Results given in Refs. [9] and [10] indicate that any tone interference should be about 10 dB below the thermal noise in a voice channel (uncompanded). Such a requirement is also necessary in companded circuits, although the subjective effect of the tone is different.

Table 8 gives the values of n_{im}/n_{th} in the worst channel, with the intermodulation noise being the tone and with the assumptions that all the SF tones in the other channels are at −16 dBmO (at the output of the 0-dBmO compressors). The input backoff should be set at −9 dB so that the tone intermodulation will be at least 10 dB below the thermal noise. There is a loss in capacity (600 to 1000 channels, depending on the satellite spacing and interference levels), but a capacity of 6000 channels can still be realized if a few extreme interference cases are excluded at 4° spacing, and full traffic coordination is done at 3° spacing.

It should be noted that in these computations SF tone power is reduced 6 dB, from −10 to −16 dBmO. If the SF tone power can be reduced further, there is no need to operate the satellite amplifier at $I_{BO} = -9$ dB, instead of the optimum capacity value of $I_{BO} = -7$ dB. However, new problems arise if the SF tones are reduced to too low a value. The difficulty is that with low power SF tones, the SF tone-to-noise ratio in the receiver is also low. If this is less than 10 dB, the receiver SF detector circuits are not likely to operate properly, and some modifications are then required in the signaling circuits. The problem is made even worse if compandors with noise advantage

Table 8—Ratio of Intermodulation Noise Power to Thermal Noise Power in the Test Channel for SSPA Under Two Conditions: (a) When All Other Channels Carry Speech Signals of −14 dBmO or (b) All Other Channels Carry SF Tones of Power −16.0 dBmO. Values of I_{BO} Are When All Other Channels Carry Speech; They Decrease by 2.0 dB When All Other Channels Carry SF Tones. Adjacent Satellite Co-frequency Transponders are Co-polarized.

Interference Condition	Spacing	I_{BO} (dB)	Capacity	IM/TH (dB) (a)	IM/TH (dB) (b)
Least favorable	4.0	−6.0	6240	0.75	−3.20
Most favorable	4.0	−6.0	7080	0.87	−3.08
Least favorable	4.0	−7.0	6300	−2.38	−6.34
Most favorable	4.0	−7.0	7500	−1.62	−5.58
Least favorable	4.0	−8.0	6120	−4.61	−9.68
Most favorable	4.0	−8.0	7380	−4.39	−9.46
Least favorable	4.0	−9.0	5700	−7.48	−12.54
Most favorable	4.0	−9.0	6780	−6.92	−11.98
Least favorable	3.0	−6.0	5640	0.95	−3.00
Most favorable	3.0	−6.0	6660	0.74	−3.21
Least favorable	3.0	−7.0	5700	−1.59	−5.55
Most favorable	3.0	−7.0	6900	−1.78	−5.74
Least favorable	3.0	−8.0	5400	−4.30	−9.37
Most favorable	3.0	−8.0	6600	−5.07	−10.14
Least favorable	3.0	−9.0	4800	−6.63	−11.69
Most favorable	3.0	−9.0	5880	−7.56	−12.62

higher than 9 dB are used to increase the capacity. With such compandors the noise level increases, directly contributing to the degradation of SF tone-to-noise ratio.

8. Conclusions

It is now possible to transmit 6000 telephone voice channels economically through a communication satellite of the RCA SATCOM type using currently available compandors and solid-state power amplifiers. The required value of SNR in each voice channel is 17.5 dB. The signal-to-thermal noise ratio is about 20.0 dB, and the signal-to-intermodulation ratio is about 27.0 dB. The rest of the noise is taken up by external interference. Such interference from adjacent satellite systems limits the capacity to about 6000 channels. Careful coordination of traffic of different systems can increase this capacity. Higher values of capacity (7500 channels at 4° spacing of the satellites and 6900 channels at 3° spacing) are possible if the power of the SF tones is reduced significantly and problems related to low SF-to-noise ratio are solved.

Acknowledgments

The author acknowledges the substantial contributions made by Dr. Leonard Schiff of RCA Laboratories.

Appendix 1

This appendix shows that the error in replacing the exact value of the intermodulation power in a channel IM_k, by the approximate value IM'_k, is small. In the notation used, the 4-kHz slots 1 to 60 are in supergroup slot 1, the 4-kHz slots 61 to 120 are in super group 2, etc. As mentioned earlier, either all the 4-kHz slots in a super group are assigned to the voice channels, or all of them are not assigned. Let

$$L(z) \triangleq \sum_{i=1}^{m} a_i z^i.$$

Then the left hand side of Eq. [15] that generates the exact values IM_k is $[L(z)]^2 L(z^{-1})$. Let Z^k equal $\exp[jk60\omega_o\tau]$ and let

$$P(z) = \sum_{k=0}^{59} z^{-k}/60,$$

$$Q(z) = \sum_{s=1}^{m'} a'_s Z^s.$$

Then

$$L(z) = \sum_{s=1}^{m'} \left(\sum_{k=0}^{59} z^{-k}/60 \right) a'_s Z^s$$
$$= P(z) Q(Z).$$

Consequently

$$\left(\sum_{i=1}^{m} a_i z^i \right)^2 \left(\sum_{i=1}^{m} a_i z^{-i} \right)$$
$$= P(z) P(z^{-1}) \left[P(z) \sum_{k=2-m'}^{2m'-1} I_k Z^k/60 \right] \quad [27]$$
$$= P(z) P(z^{-1}) \sum_{i=i_1}^{i_2} \mathrm{IM}'_i z^i$$

where $i_1 = (2 - m')\ 60\text{-}59$ and $i_2 = (2m' - 1)60$. The term $P(z)P(z^{-1})$ can be expanded as

$$P(z)P(z^{-1}) = \sum_{k=-59}^{59} p_k z^k \quad [28]$$

where $p_k = (60 - |k|)/60^2$.

Using Eqs. [15], [18], and [27] we arrive at

$$\mathrm{IM}_i = \sum_{k=-59}^{59} p_k \mathrm{IM}'_{i+k},\ 1 < i < m, \quad [29]$$

which shows that the exact values IM_i are obtained by taking a weighted moving average of the approximate values IM'_i. The width of the smoothing function $P(z)P(z^{-1})$ is that of two super groups minus one. Further, the values of IM′ are constant within a super group. Let s be the super group in which ith 4-kHz slot is located. From Eq. [19], the intermodulation power in any channel in the sth super group is $I_s/60$. Then Eq. [29] can be written

$$\mathrm{IM}_i = (q_o I_s/60) + (q_{-1} I_{s-1}/60) + (q_1 I_{s+1}/60)$$

where $I_{s-1}/60$ and $I_{s+1}/60$ are the intermodulation power values in $(s - 1)$th and $(s + 1)$th super groups, and q_o, q_{-1} and q_1 are non-negative constants such that

$$q_o + q_{-1} + q_1 = 1.$$

The ratio of the exact to the approximate intermodulation power is

$$R = \mathrm{IM}_i/(I_s/60).$$

Then it is easily derived that

$$|10 \log R| < |10 \log(I_{s-1}/I_s)| \quad \text{or} \quad |10 \log(I_{s+1}/I_s)| \qquad [30]$$

whichever is larger. If I_s, I_{s+1}, and I_{s-1} are nearly equal to each other, the error made is nearly 0 dB, i.e., the exact value IM_i and the approximate value $I_s/60$ are nearly equal. The channel assignments are made such that the intermodulation powers in all the super groups are nearly the same (within 0.2 dB). This also assures that the error in using IM_i' in the place of IM_i is also small. In any case, the inequality [30] shows that the error (in dB) is upper bounded by the difference between the intermodulation power at one super group and that at the neighboring super group.

Appendix 2

Let there be n voice channels that need to be distributed among m 4-kHz slots, where $m = 9000$. The staggered cosine rule gives for the channel frequencies

$$f_i = u36[1 - \cos\{(i-1)\pi/(n-1)\}],\ i = 1, 2, \ldots n/2$$
$$= u36[u - (1-u)\cos\{(i-1)\pi/(n-1)\}],\ i = n/2 + 1, \ldots n,$$

where u is a number between 0 and 1, and 36 is the bandwidth of the transponder in MHz.

The results given in Table 1 are obtained by choosing $u = 0.5$. The values of f_i are discretized to the nearest 4-kHz slot frequency.

Appendix 3

The normalized spectrum functions $i_c(f)$ and $i_o(f)$ are as follows.

1. *Single carrier FDM/FM.* A single carrier FDM/FM that carries 1092 channels (uncompanded) has a multichannel rms deviation of about 4 MHz. Then its spectrum is

   $$i(f) = \frac{1}{\Delta\sqrt{2\pi}} e^{-f^2/2\Delta^2},$$

   where $\Delta = 4$ and f is in MHz. This is referred to as $1 - \text{FM}$ in the Tables.
2. *Two carrier FDM/FM.* Consider two-carrier operation with each carrier transmitting 432 (uncompanded) channels and having an allocated bandwidth of 17.5 MHz. The multichannel rms deviation

Δ of each carrier is 2 MHz. The combined spectrum is

$$i(f) = 0.5 \left[\frac{1}{\Delta\sqrt{2\pi}} e^{-(f+10)^2/2\Delta^2} + \frac{1}{\Delta\sqrt{2\pi}} e^{-(f-10)^2/2\Delta^2} \right]$$

where f is in MHz. When such a signal goes through a power amplifier, the I_{BO} of which is taken to be 0 dB, the output backoff is about 1.5 dB. This factor should be taken into account in obtaining the value of $e(f)$. This spectrum is referred to as 2-FM in the Tables.

3. *Wideband Digital Carrier*. The power spectral density is approximated by (see Ref. [11])

$$10 \log i(f) = -17 \text{ dB/MHz if } |f| < 15 \text{ MHz}$$

and decreases linearly from −17 to −33 dB/MHz as $|f|$ changes from 15 to 20. This spectrum is referred to as "digital" in the Tables.

4. *TV Carrier*. The spectrum is given by

$$10 \log i(f) = -14 \text{ dB/MHz if } |f| < 12.5$$

$$= \text{no signal if } |f| > 12.5.$$

In all the above functions, the power spectral density in dB/Hz is given by $10 \log i(f) - 60.0$.

References:

[1] K. Jonnalagadda, "Syllabic Companding and Voice Capacity of a Transponder," *RCA Rev.*, **41**, p. 275, Sept. 1980.

[2] M. R. Freeling and W. H. Braun, "Maximum Transponder Capacity for Transmission of FDM-FM Channels," *RCA Rev.*, **41**, p. 307, Sept. 1980.

[3] W. C. Aherns, F. P. Duffy, and J. A. Maher, "Speech Signal Power in the Switched Message Network," *Bell Sys. Tech. J.*, **57**, p 2695, Sept. 1978.

[4] B. Dornan, et. al, "A 4-GHz GaAs FET Power Amplifier: An advanced Transmitter for Satellite Downlink Communication Systems," *RCA Rev.*, **41**, p. 472, Sept. 1980.

[5] J. A. Stewart and E. A. Huber, "Comparison of Modulation Methods for Multiple-access Synchronous Satellite Communication Systems," *Proc. IEE(London)*, **111**, p. 535, March 1964.

[6] P. L. Bargellini, "The INTELSAT IV Communication System," *COMSAT Tech. Rev.*, **2**, p. 460, Fall 1972.

[7] N. M. Blachman, "The Output Signals and Noise from a Nonlinearity with Amplitude-Dependent Phase Shift," *IEEE Trans. Information Theory*, **IT-25**, p. 77, Jan., 1979.

[8] M. Morita, T. Fulsami, and S. Yamato, "STAR System—Part I: General Description," *NEC Research and Development*, **10**, p 1, 1966.

[9] T. K. Sen, "Masking of Crosstalk by Speech and Noise," *Bell Syst. Tech. J.*, **49**, p. 561, April 1970.

[10] J. E. Hawkins,, Jr., and S. S. Stevens," The Masking of Pure Tones and of Speech by White Noise," *J. Acoust. Soc. of Amer.*, **22**, p. 6, Jan 1950.

[11] R. G. Lyons, "Effects of PSK Spectral Spreading in Satellite Transponders," Int. Conf. on Comm., Minneapolis, Minn. (1974).

Broadband Microwave Power Amplifiers Using Lumped-Element Matching and Distributed Combining Techniques

R. L. Camisa and A. Mikelsons
RCA Laboratories, Princeton, NJ 08540

Abstract—An improved approach is described where submicrometer gate-length devices are lumped-element matched and combined to achieve broadband 0.75-W and 1.5 W amplifiers that cover the 6.5-11 GHz frequency band. An improved mounting procedure was demonstrated where all the device source contacts are joined with a thick gold bridge and soldered to the device carrier. This technique has proven to be important in the flip-chip mounting of large-width GaAs FETs. Also all the microwave-circuit matching and combining was realized in a printed circuit format that has improved the reproducibility of discrete lumped elements.

1. Introduction

There is a great deal of interest in replacing medium power (1–5 W) traveling wave tubes with more reliable, lower cost GaAs FET amplifiers in broadband (6–17 GHz) electronic warfare systems. To achieve broadband power amplification a large number of transistor cells must be efficiently matched and combined. From a bandwidth point of view, impedance matching and cell combining can best be handled in a monolithic format because unwanted circuit parasitics can be minimized, and tuning elements can be made an integral part of the transistor. However, in power amplifier applications monolithic circuit losses are often unacceptably high because thin substrates are required for thermal considerations. The best power amplifiers have therefore been realized using a hybrid microwave integrated circuit approach.

A 1-W multistage amplifier that covers the 6.5–11 GHz frequency band has been described elsewhere.[1,2] It uses two 2.4 mm commercially available devices that are lumped-element matched and combined in a balanced configuration. The lumped elements employ discrete chip capacitors and ribbon inductors, and the circuit topology is such that each tuning element can easily be optimized experimentally. The reproducibility of this approach has also been demonstrated using automated assembly techniques.[3,4]

This paper describes an improved approach where submicrometer devices are lumped-element matched and combined to achieve broadband 0.75-W and 1.5-W amplifiers in the 6.5–11.0 GHz frequency band. The 1.5 W amplifier stage uses four 1.2 mm width transistor cells flip-chip mounted for low source inductance and low device/carrier thermal resistance. An improved device mounting procedure is described where the device sources are joined together with a thick gold bridge and then soldered to the carrier. This improvement is important when flipping large-width transistors. The devices are also lumped-element matched using printed circuit elements on high dielectric constant substrates ($K = 85$). Cell combining and additional matching are realized with uncoupled microstrip transmission lines fabricated on alumina substrates.

2. Devices

During this program, experimental RCA self-aligned and aligned gate GaAs FETs were used exclusively.[5] All devices are mounted in a flip-chip format on copper carriers. Normally, the devices were thermal-compression bonded to the copper carriers, but during the course of this program the bridging of all device sources and soldering them to the copper pedestal was shown to be feasible. This technique is necessary to make reliable source contacts to large-gate-width devices, thereby providing simultaneously a low parasitic source inductance and low thermal resistance. The device was organized into a four-cell 0.6 mm/cell chip, which made it possible to do experiments to find the optimum cell size for maximum output power and efficiency at 11.0 GHz. Early in the program, a cell size of 1.2 mm was chosen as optimum, but as the device mounting techniques improved, a larger 2.4 mm cell size was shown to be feasible.

2.1 Chip Organization

Fig. 1 is an SEM of an FET chip used in this program. The chip is organized into a four-cell, 0.6-mm-per-cell pattern. Each cell consists of four parallel gates, each of which is 0.15 mm long. The source and drain pads in this photograph are plated to a higher level than the

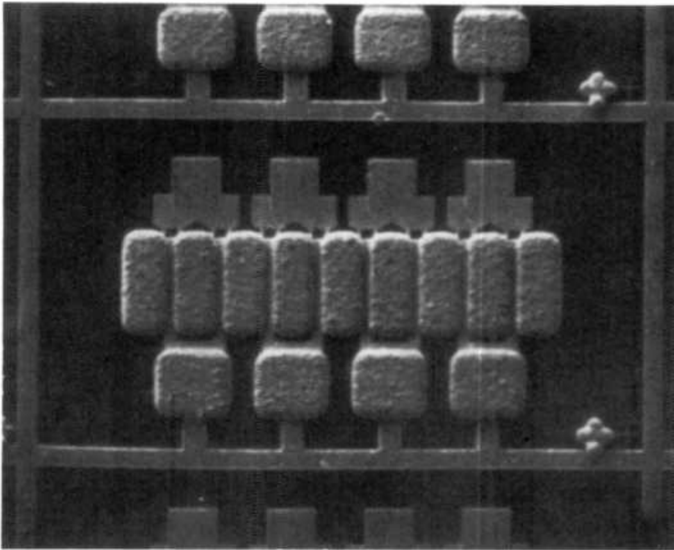

Fig. 1—Four-cell 0.6-mm/cell power FET device layout.

gate pads, and the sources are not joined together on the chip. The chip size is approximately 0.5 mm × 1 mm. Different width devices are formed by interconnecting appropriate gate and drain pads with ribbons on the chip. Ribbons are also used to connect the transistors to the outside world. When the transistors, as described above, are flip-chip mounted, all the sources are joined together by the carrier pedestal. If one source is not grounded, a part of one transistor cell will not be active and it will parasitically load down the rest of the device, which is active. This problem is especially acute for large power transistors that have many sources.

2.2 Metal-Bridged and Soldered Devices

During the course of the program, metal-bridged devices were developed, which greatly enhanced the probability of combining larger devices. Fig. 2a is a photograph of a four-cell chip in which each source contact is joined together with a gold bridge. Fig. 2b is a close-up of the bridged source area, which consists of the ohmic contact metal on the wafer, a plated-up post area, followed by the metal bridge. The post is approximately 12-μm high and the bridge is 25–50 μm thick. In the figure, the gold bridge metal appears not to make contact to the posts below it, but in actuality it does.

The metal bridge guarantees electrical continuity to every source, which is important when working with multicell devices. It provides a

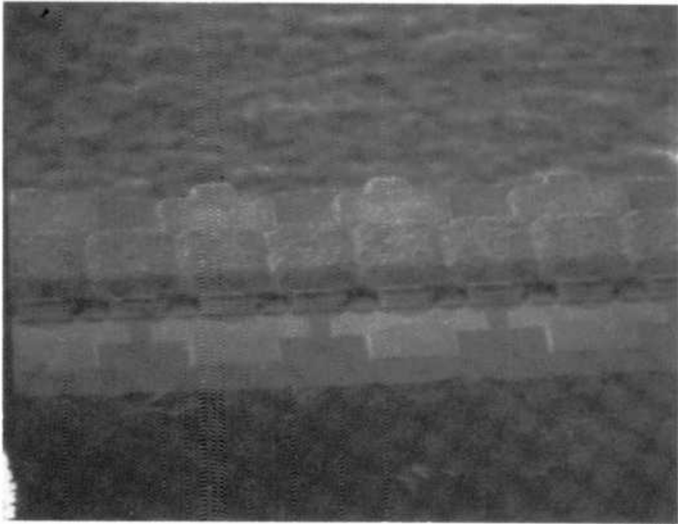

(a)

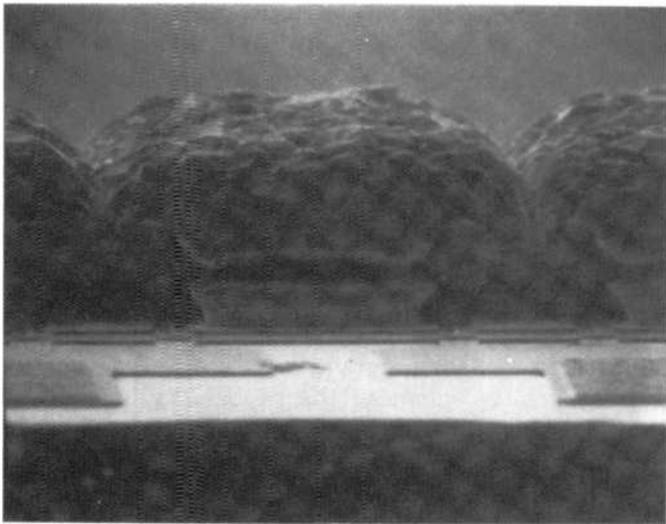

(b)

Fig. 2—2.4-mm 1-W device with bridged source contacts: (a) bridged four-cell device and (b) close-up of bridged sources.

metal cushion between the GaAs device surface and the carrier to which the device is mounted. The bridge also covers the gate area of the device which is otherwise exposed. There was a definite power performance improvement once the metal bridged devices were developed. A second improvement in the flip-chip process was demonstrated when a metal bridged device was soldered onto the copper carrier. Soldering guarantees that the bridge is in intimate contact with the carrier, which simultaneously is a low inductance ground and low thermal resistance heat sink.

2.3 Device Characterization

Table 1 is a summary of the best narrowband output power performance obtained at 11.0 GHz. These data were not taken on one wafer, but on a number of wafers during the course of the year. The larger, higher output power results were obtained with internally-matched devices. Without matching, the performance was much poorer. The results correspond approximately to 0.5 W/mm of source width at a gain of greater than 4.0 dB. The drain potential in all cases was 8.0 V. Higher device efficiency is feasible at lower output power with a lower drain potential.

Fig. 3 is a plot of the small signal input and output impedances for one, two, and four cells mounted on a 0.070-inch wide copper carrier. The reference plane for these measurements is the edge of the copper carrier. The measurements were made using a coaxial test fixture.[3] The real part of the input impedance for one, two, and four cells corresponds approximately to 7.5, 5.0, and 2.5 ohms, respectively. The drain output impedance can be modelled as a parallel *RC* circuit with a small series inductor. These measurements include a ribbon from the device chip to a small standoff and the capacitance of the standoff, which is approximately 0.1 pF.

Initially, when power measurements were made to determine the optimum cell size for 11.0 GHz operation, we could not get output power from more than two cells. At the end of the program, after the solder flip-chip techniques were developed, we were able to combine four cells directly. Because of this, a majority of our matched carrier

Table 1—Summary of Narrowband Output Power Performance at 11 GHz

	Width (mm)	P_o(W)	G(dB)	Efficiency (%)
One Cell	0.6	0.30	4.8	26
Two Cell	1.2	0.46	4.9	22
Four Cell	2.4	1.2	5.8	28
Eight Cell	4.8	1.7	4.5	15

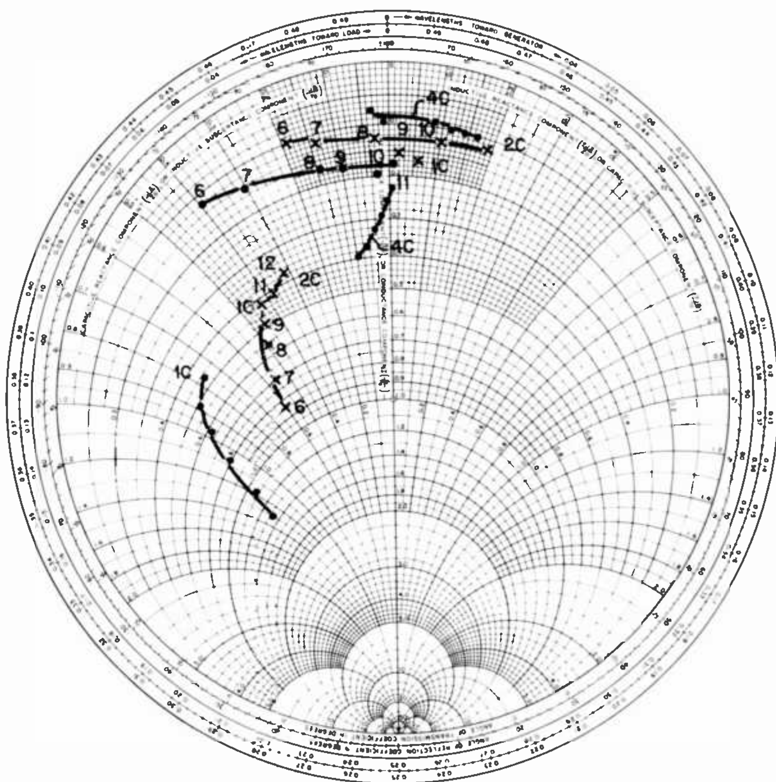

Fig. 3.—Input and output impedances for one, two, and four cells in the 6–12 GHz range.

developments use 1.2 mm, two-cell devices as the fundamental building block.

3. 0.5-W, 1.2-mm-Wide Matched Carrier

In this section, the development of an 0.5-W matched carrier using 1.2-mm wide transistors is described. The transistors consist of two individual cells joined together on the chip with ribbons. All the amplifiers developed use 1.2-mm width GaAs FETs as their fundamental building block. To optimize transistor performance, the gate side of the device is first matched at the high end of the frequency band of interest. Once the input is matched, the optimum load for maximum power-added efficiency is determined using load-pull techniques. It turns out that the optimum load impedance is close to 50 Ω, which makes it simple to correlate the characterization data with an actual amplifier design.

3.1 Impedance Matching with High K Dielectrics

The gate side of the device is impedance-matched to a 50-Ω source impedance using a two-section low-pass filter prototype circuit consisting of two series inductors (L1, L2) and two shunt capacitors. The first inductor in the network is a ribbon from the transistor chip to the input substrate. The two shunt capacitors were printed on the 0.23 mm thick Rutile substrate ($K = 85$). The inductor that joined the two capacitors in initial experiments was a ribbon; later it was printed on the same substrate as the capacitors. The whole input network therefore eventually was printed except for the first inductor.

Fig. 4 summarizes the gate matching network and the corresponding input impedance locus. The two capacitors were 0.38 mm squares with measured values of 0.9 pF. The gap between capacitors and the distance from the transistor was 0.25 mm. Since each transistor consisted of a four-cell 0.6 mm/cell pattern, two 1.2-mm width cells could

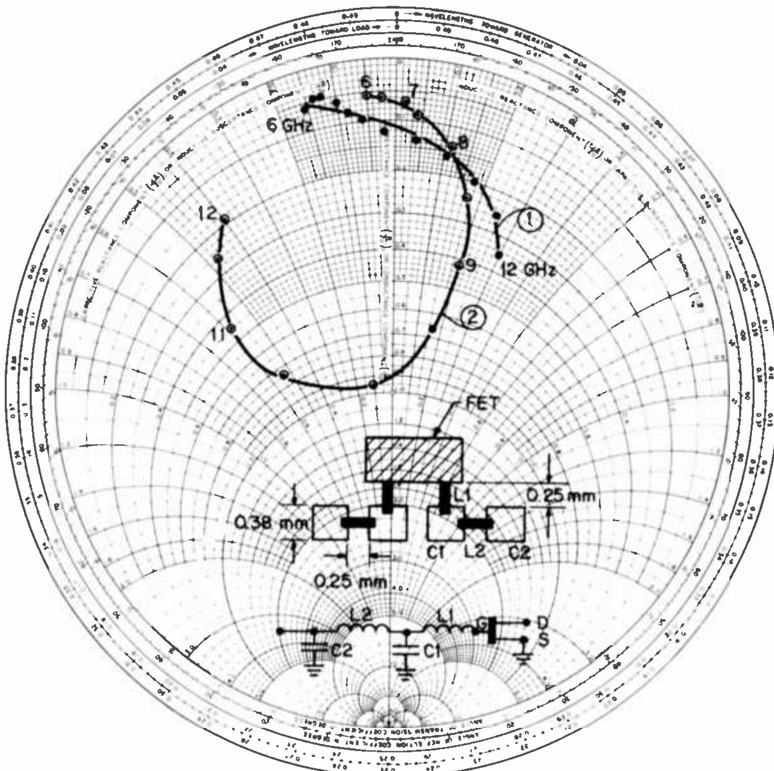

Fig. 4—Matched input impedance locus, matching circuit, and equivalent circuit.

be formed within one chip. The S-parameters for the device alone were first measured by mounting a device with a low value 0.1 pF chip capacitor on the gate side of the device. The S-parameters for a two-cell, 1.2 mm device were presented in an earlier section. The effect of each section of the matching network could be monitored with special fixturing[1] since the capacitors are located on the edge of the transistor carrier. The first inductor and capacitor partially match the device. The addition of the second inductor and capacitor matches the gate input impedance very well at 10 GHz. In Fig. 5 the uniformity within one chip is illustrated with the left-side (LS) and right-side (RS) impedance contours plotted versus frequency from 6–12 GHz. The impedance curves are within measurement accuracy of each other.

3.2 Large-Signal Characterization

After a satisfactory input match was obtained, measurements were made to obtain the output impedance for maximum power added

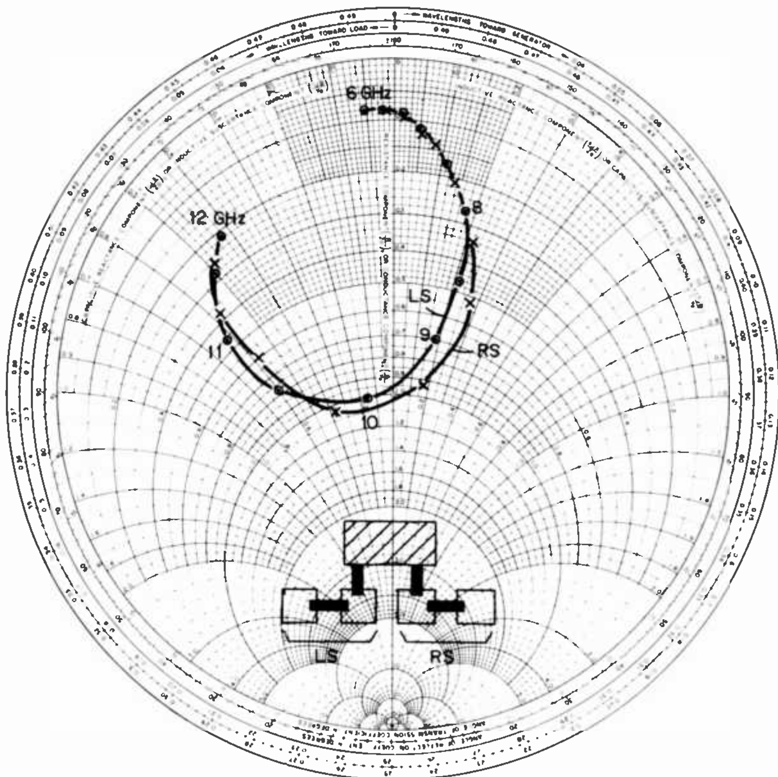

Fig. 5—Matched input impedance for two 1.2-mm cells (LS, RS) within one chip.

efficiency. A computer-controlled X-band load-pull technique developed in our laboratory was used to gather the necessary data. Fig. 6 summarizes typical data obtained by such a system. The small-signal and large-signal optimum load are plotted versus frequency in the 9–11 GHz range. The table below the impedance contours summarizes best device performance when the optimum load for maximum efficiency is presented to the device by the tuner. As one can see, there is a large difference between the conjugate load contour for small-signal and large-signal operation. The data in Fig. 6 is for a device operated with 8 V on the drain and an input power of 0.15 W. The maximum efficiency is typically in the 19–23% range with an output power between 0.4 and 0.5 W. These data were obtained without tuning the input at all. The optimum load measured is very close to 50 Ω. Table 2 summarizes similar data for 8, 9, and 10 V on the drain with an input power of 0.15 W. The output power increases with the drain voltage, the power added efficiency decreases slightly, and the optimum reflection coefficient increases in magnitude.

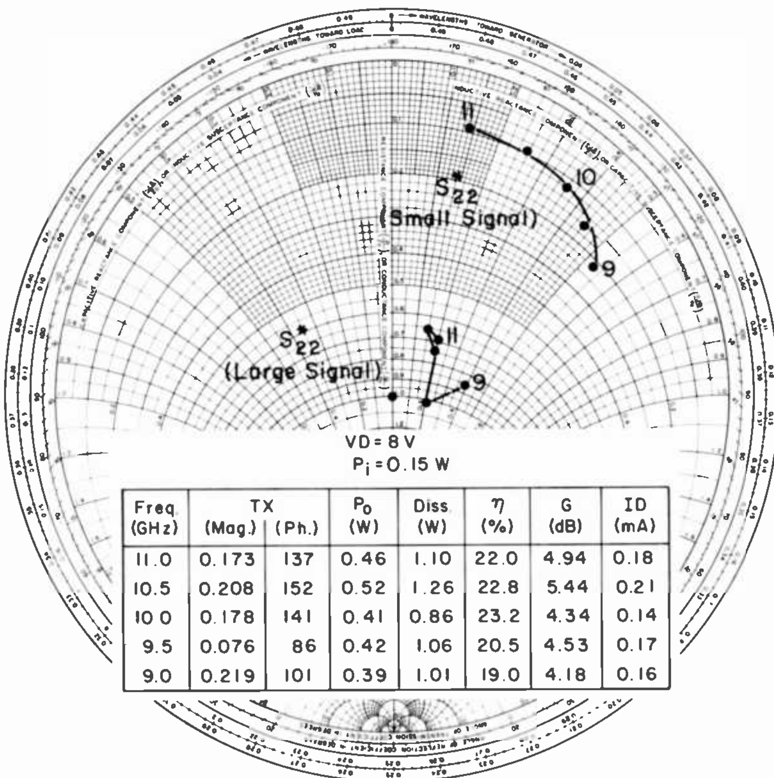

Freq (GHz)	TX (Mag.)	TX (Ph.)	P_o (W)	Diss (W)	η (%)	G (dB)	ID (mA)
11.0	0.173	137	0.46	1.10	22.0	4.94	0.18
10.5	0.208	152	0.52	1.26	22.8	5.44	0.21
10 0	0.178	141	0.41	0.86	23.2	4.34	0.14
9.5	0.076	86	0.42	1.06	20.5	4.53	0.17
9.0	0.219	101	0.39	1.01	19.0	4.18	0.16

Fig. 6—Large-signal load-pull data for a 1.2-mm device B979-55 with 8 V on the drain and an input power of 0.15 W.

Table 2—Load-Pull Data with a Drain Potential of 8, 9, and 10 V [width-1200 μm (two cells), P_i = 0.15 W, no input tuning]

	FREQ. (GHz)	TX (MAG.)	TX (PH.)	P_o (W)	DISS. (W)	EFF. (%)	G (dB)	ID (mA)
VD = 8V	11.0	.173	137	.46	1.10	22.0	4.94	.18
	10.5	.208	152	.52	1.26	22.8	5.44	.21
	10.0	.178	141	.41	.86	23.2	4.34	.14
	9.5	.076	86	.42	1.06	20.5	4.53	.17
	9.0	.219	101	.39	1.01	19.0	4.18	.16
	11.0	.202	139	.52	1.33	21.7	5.39	.19
	10.5	.220	141	.56	1.41	22.7	5.76	.21
VD = 9V	10.0	.156	136	.47	1.08	23.0	4.95	.16
	9.5	.190	136	.47	1.20	21.2	5.01	.17
	9.0	.216	102	.43	1.22	18.4	4.54	.18
	11.0	.202	139	.540	1.51	20.6	5.59	.19
	10.5	.254	141	.580	1.64	21.0	5.93	.21
VD = 10V	10.0	.160	131	.520	1.35	21.6	5.36	.17
	9.5	.190	136	.500	1.43	19.9	5.31	.17
	9.0	.235	107	.440	1.46	16.8	4.72	.18

Since the optimum load is close to 50 Ω for maximum power-added efficiency, the gate matched device was tested as an amplifier with a 50 Ω load impedance over the 9–11 GHz frequency range. Two devices were tested and the power added efficiency and the output power are plotted versus frequency from 9–11 GHz in Fig. 7. With an input power of 0.2 W, a power added efficiency of 16% was measured over most of the frequency band for the two devices measured. The degradation in

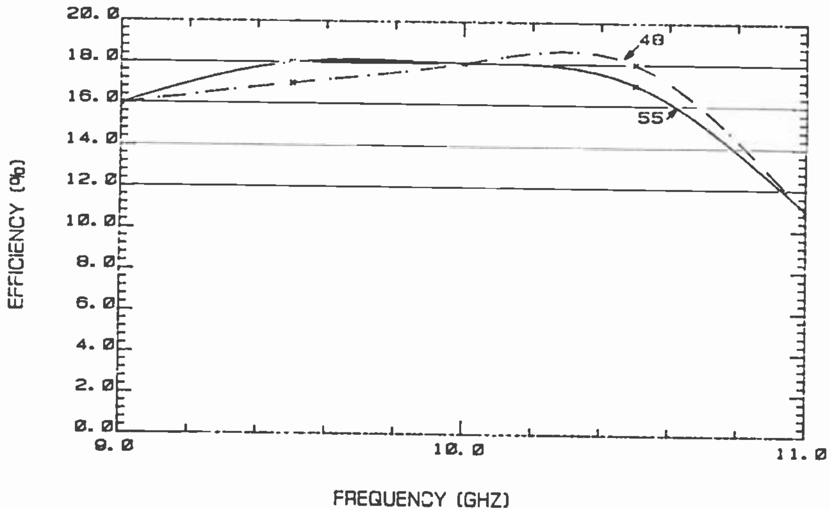

Fig. 7—Power added efficiency versus frequency for a gate-matched device with a 50Ω load impedance.

efficiency from an optimum of 20% is mainly due to the slight deviation from optimum conditions. Overall, the correlation between the two types of measurements is good.

4. Broadband and FET Power Stages

Using lumped-element matched 1.2-mm cells as fundamental blocks, broadband 0.75 W and 1.5 W power stages were developed. The individual transistor cells were further matched and combined using distributed resistor transmission line networks printed on alumina substrates.

4.1 0.75-W, 2.4 mm Amplifier

Table 3 is a summary of the small signal *S*-parameters of two impedance matched 1.2-mm devices within one chip from wafer D1115. The first column corresponds to the magnitude of the input reflection coefficient. The input has a single tuned response with a VSWR of less than 1.2 at 10 GHz. The output (S22) has no matching at all. Using these *S*-parameters, a matching and combining network was designed and optimized on the computer. The final circuit realized is shown schematically in Fig. 8. The two 1.2-mm devices are joined together on the gate side of the device with 3.3 mm long and 3.8 mm wide transmission lines fabricated on 0.63 mm thick alumina substrates. The output of the two devices is connected directly to a two-section transforming network. The first section is 2.8 mm long and 1.6 mm

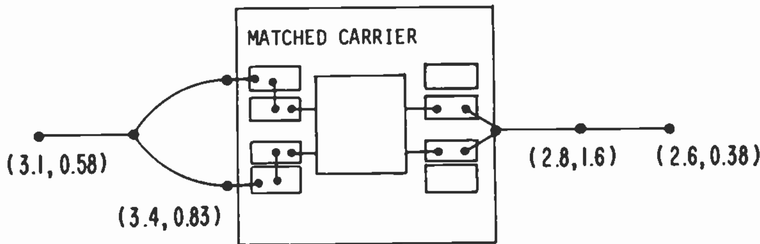

Freq.	S_{11},I,RC X	1.000*	FGAIN PH X	1.000DB	S_{22},O,RC X	1.000*
8.500	.431	-10.90	4.612	-50.04	.758	-25.92
9.000	.400	-84.45	4.784	-92.39	.695	-46.59
9.500	.459	-145.04	5.114	-132.78	.621	-71.67
10.000	.464	159.67	5.357	-177.89	.541	-105.11
10.500	.426	103.26	4.489	134.10	.485	-154.47
11.000	.333	33.01	5.511	86.19	.475	150.79
11.500	.297	-69.29	4.524	32.96	.507	103.92

Fig. 8—Simulation of two matched and combined 1.2-mm width devices. Top shows schematic representation and bottom simulation of circuit.

Table 3—Small-Signal S-Parameters of Two Impedance-Matched 1.2-mm Devices

	S_{11}		S_{21}		S_{12}		S_{22}	
A. ELEMENT #6: D1115-11 RS								
8.500	.631	160.700	1.548	−24.800	.086	−61.400	.788	−134.000
9.000	.432	153.700	1.654	−43.600	.098	−79.900	.797	−142.800
9.500	.239	149.500	1.708	−61.100	.111	−101.300	.792	−151.800
10.000	.083	−102.900	1.749	−85.600	.116	−123.600	.751	−160.200
10.500	.351	−96.100	1.557	−109.600	.112	−146.500	.696	−165.500
11.000	.549	−110.000	1.319	−128.600	.101	−167.700	.640	−168.300
11.500	.680	−126.000	1.103	145.700	.086	175.200	.617	−169.200
B. ELEMENT #10: LS								
8.500	.701	166.300	1.373	−20.000	.075	−55.200	.773	−130.400
9.000	.563	160.000	1.462	−35.900	.091	−70.400	.804	−138.400
9.500	.396	146.000	1.624	−51.200	.104	−92.300	.808	−147.100
10.000	.112	129.000	1.740	−75.900	.113	−114.000	.782	−155.700
10.500	.193	−83.800	1.243	−101.000	.116	−136.700	.732	−162.400
11.000	.435	−100.000	1.426	−122.000	.109	159.500	.765	−166.500
11.500	.603	−118.200	1.204	−142.100	.096	−178.800	.637	−167.900

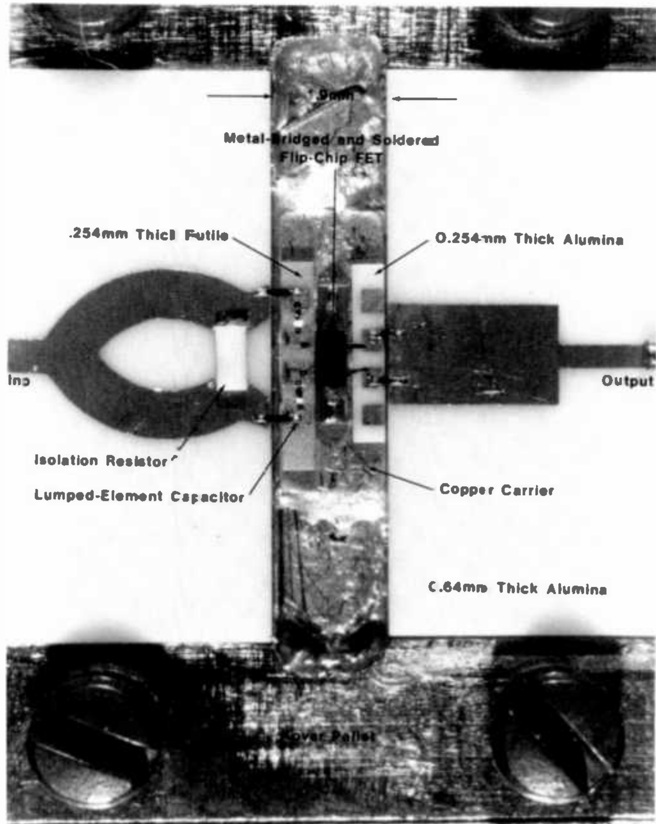

Fig. 9—1-W 2.4-mm circuit.

wide. The second section is 2.6 mm long and 0.38 mm wide. In the optimization of this circuit, the first section of the output transformer was constrained to a maximum value of 1.6 mm. Over the 8.5–11.5 GHz frequency band, a minimum gain of 4.5 dB is predicted by the simulation.

The actual circuit fabricated is shown in Fig. 9. The circuit is completely printed except for ribbons from the device to the carrier and from the carrier to the input and output combiner. In the photo there is also one more ribbon interconnecting tuning pads, which was later eliminated. The device is soldered to the copper carrier. Also, there is an isolation resistor between input gate transmission lines to provide gain stability and high isolation between devices.

The output power versus frequency for this circuit is shown in Fig. 10. Over the frequency band the output power was in excess of 0.75 W. When saturated hard the output power was in excess of 1 W over most of the band. The gain decreased at the upper end of the frequency band and could not be compensated for with external tuning. The circuit was also difficult to tune because of its small size and because most of the impedance matching is accomplished on the high-dielectric-constant substrate very close to the device.

4.2 1.9-W, 4.8-mm Width Device

Using the same techniques as described in the previous section, four 1.2 mm devices were matched and combined. Fig. 11 is a photograph

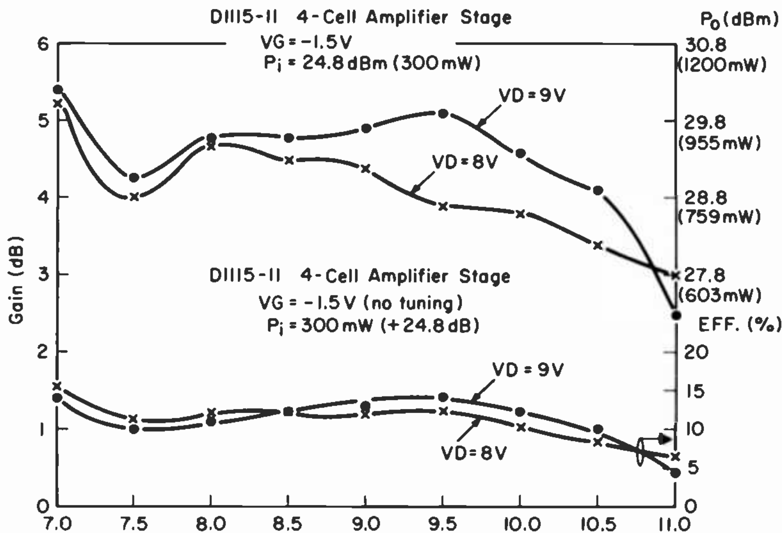

Fig. 10—Performance of the 2.4-mm amplifier over the 7-11 GHz band.

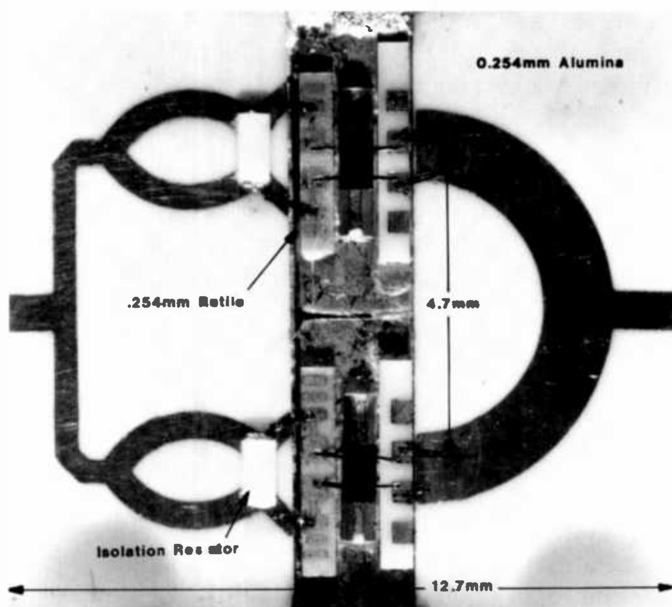

Fig. 11—2-W 4.8-mm circuit.

of the amplifier stage and Fig. 12 is a plot of the gain and power added efficiency from 6.5–11.0 GHz. Over most of the frequency band of interest the output power is well in excess of 1.5 W with 5 dB gain and a power added efficiency of 10%. Again, in the upper end of the frequency band the gain and output power decreased which is unexplained. In this amplifier, tuning pads are provided for on the high dielectric constant material, but trimming did not seem to help.

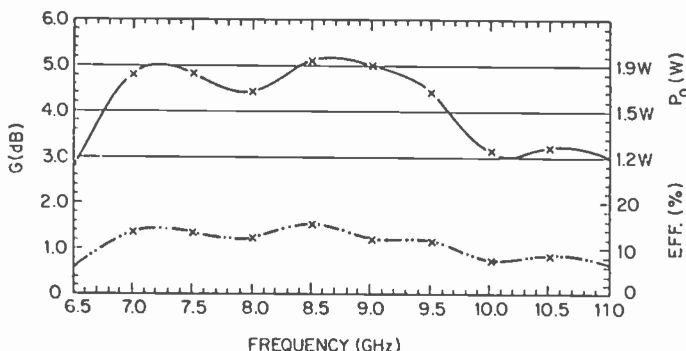

Fig. 12—Performance of the 4.8-mm amplifier over the 6.5-11 GHz band.

5. Conclusions

An improved impedance-matching and cell-combining technique has been demonstrated using completely printed networks on high dielectric constant substrates. Using this approach experimental RCA transistors were operated to obtain broadband 6.5–11 GHz, 0.75-W and 1.5-W amplifier performance. In these amplifier stages, 0.5-W 1.2-mm width devices were used as the fundamental building block. In current work a broadband 3-W power stage using 2.4 mm devices is under development.

Acknowledgments

The authors wish to acknowledge G. Taylor, Y. Yun and W. Reichert who supplied the aligned and self-aligned gate FETs used in this work. The transistors used were assembled by J. Cordas and W. Cvecich. The initial soldered devices were assembled by E. Mykietyn. The authors also wish to acknowledge the encouragement of S. Y. Narayan and F. Sterzer.

References:

[1] R. L. Camisa, J. B. Klatskin, and A. Mikelsons, "Broadband Lumped-Element GaAs FET Power Amplifiers," 1981 International Microwave Symp. Digest, Los Angeles, June 15–19, IEEE Cat. No. 81CH1592-5, pp. 126–128.

[2] R. L. Camisa, J. B. Klatskin, and A. Mikelsons, "Lumped-Element GaAs FET Power Amplifiers," *RCA Rev.* **42**, p. 557, Dec. 1981.

[3] J. B. Klatskin, R. L. Camisa, and D. Haggis, "Fabrication of Lumped-Element Broadband GaAs MESFET Microwave Power Amplifiers," *RCA Rev.* **42**, p. 576, Dec. 1981.

[4] J. B. Klatskin, R. L. Camisa, and D. Haggis, "Design and Fabrication Techniques for Lumped-Element GaAs MESFET Power Amplifiers Using Automated Assembly Procedures," 1982 IEEE MTT-S International Microwave Symp. Digest, June 15–17, Dallas, Texas, IEEE Cat. No. 82CH1705-3, p. 172.

[5] G. C. Taylor, S. G. Liu, and D. Bechtle, "Ion-Implanted K-Band GaAs Power FET," 1981 IEEE MTT-S International Microwave Symp. Digest, Los Angeles, June 15–19, p. 46, IEEE Cat. No. 81CH1592-5.

Offset Near-Field Gregorian Antenna Scanning Beam Analysis

Eugene C. Ngai
RCA Astro-Electronics, Princeton, NJ 08540

Abstract—A method is presented for analyzing the offset near-field Gregorian antenna. The scanning capability of the antenna system (three dimensional) is demonstrated. The analysis employs geometrical optics ray-tracing techniques to transform feed-array amplitude and phase distributions into near-field Gregorian aperture distributions. Reflector-aperture field integration techniques are then employed to compute the related antenna pattern and gain characteristics. A preliminary study of the plane-wave spectrum (PWS) method applied for the near-field offset Gregorian reflectors is also included.

1. Introduction

For satellite communications in the 1980s, there is a strong trend toward wideband communication packages utilizing a multiplicity of narrow high-powered beams. Two classes of satellite-switched time division multiple access (SS-TDMA) have been proposed.[1] The first class is based on the switching occurring between multiple transponders, each with fixed antenna pointing. The second, shown in Fig. 1, incorporates individual transponders with variable antenna pointing (beam switched).

The vital element of the beam-switching approach is the antenna. A large phased-array antenna requires too much power to be practical at its present stage of development; it also adds too much weight to the payload. To obtain the performance of a large-aperture phased array, a small phased array fed into a Gregorian reflector may be used to form a large image of the small array over the main reflector (Fig. 2).

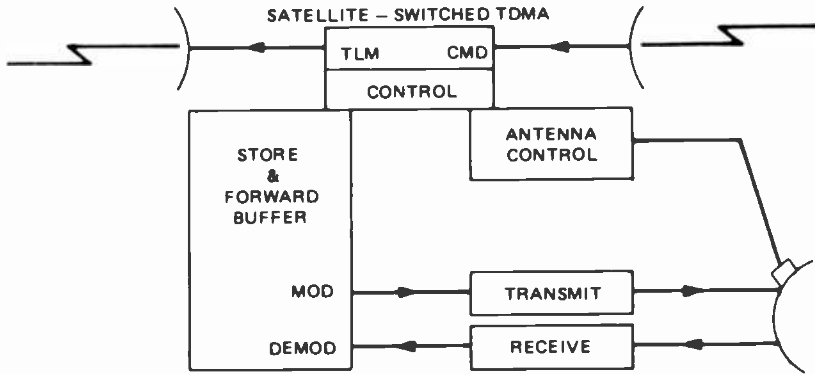

Fig. 1—Single-antenna beam switching.

This dual-reflector antenna, with equivalently longer focal length in a physically compact geometry and with an electronically steerable phased array feed that provides a limited electronic scan capability, is potentially suitable for earth coverage from a geosynchronous communications satellite.

A simplified diffraction analysis of the near-field Gregorian antenna was completed to analyze the scanning capability of the antenna system. The analysis employed geometric optics ray-tracing techniques to transform feed-array amplitude and phase distributions into near-field Gregorian aperture distributions. Reflector-aperture field integration techniques were then employed to compute related antenna

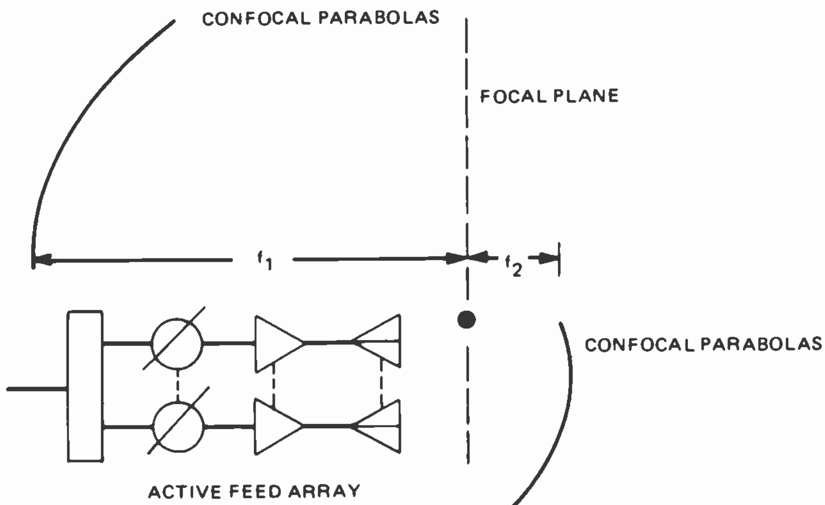

Fig. 2—An offset near-field Gregorian reflector with active feed array.

pattern and gain characteristics, which compared favorably with reported analysis and data of this antenna configuration.[2]

2. Theory

2.1 Feed Formulation

To simplify the analysis, the feed array is usually replaced by a planar feed that is parallel to the focal plane, as shown in Fig. 3. The main dish is described by

$$z = \frac{x^2 + y^2}{4f_1} - f_1, \quad [1]$$

and the subdish is described by

$$z = f_2 - \frac{x^2 + y^2}{4f_2}, \quad [2]$$

where (x, y, z) refer to the OX, OY, OZ coordinate system.

QX_f, QY_f, QZ_f is the coordinate system for the feed array. The two

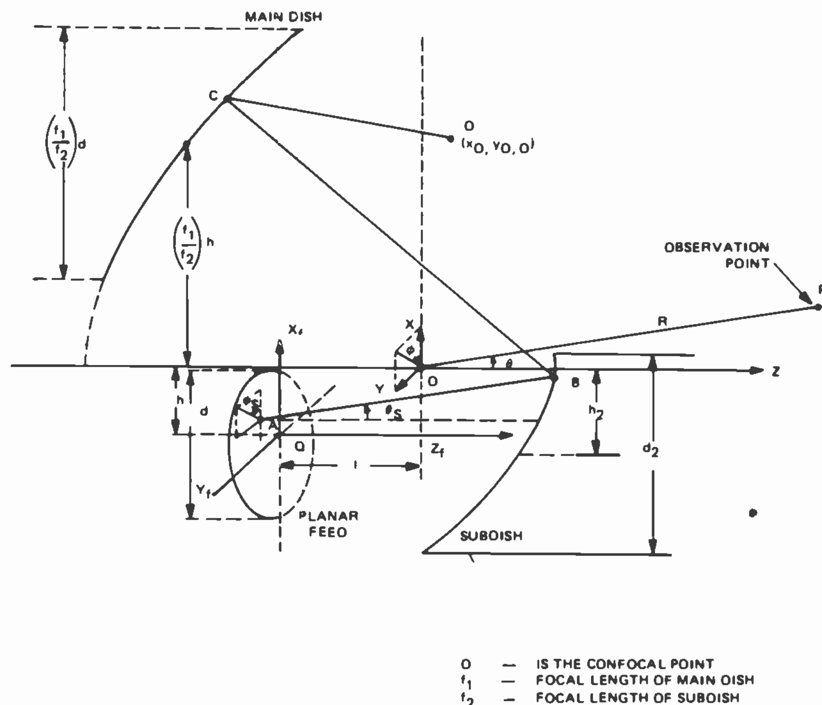

Fig. 3—Offset-feed Gregorian geometry.

coordinate systems are related as follows:

$$
\begin{aligned}
x_f &= x + h \\
y_f &= y \\
z_f &= z + l.
\end{aligned} \quad [3]
$$

The condition for the feed sampling points to fall within the circular aperture is as follows (Fig. 4):

$$x_f(m)^2 + y_f(n)^2 \leq \left(\frac{d}{2f_2}\right)^2, \quad [4]$$

where

$$
\begin{aligned}
x_f(m) &= \left[\frac{2(m-1)}{M-1} - 1\right]\frac{d}{2f_2} \text{ and} \\
y_f(n) &= \left[\frac{2(n-1)}{M-1} - 1\right]\frac{d}{2f_2}.
\end{aligned} \quad [5]
$$

M is the number of sampling points along the diameter of the feed aperture. Since

$$
\begin{aligned}
\Delta x_f &= \frac{1}{2}\left[x_f(m+1) - x_f(m)\right] = \frac{1}{M-1}\frac{d}{f_2} \\
\Delta y_f &= \frac{1}{2}\left[y_f(n+1) - y_f(n)\right] = \frac{1}{M-1}\frac{d}{f_2},
\end{aligned} \quad [6]
$$

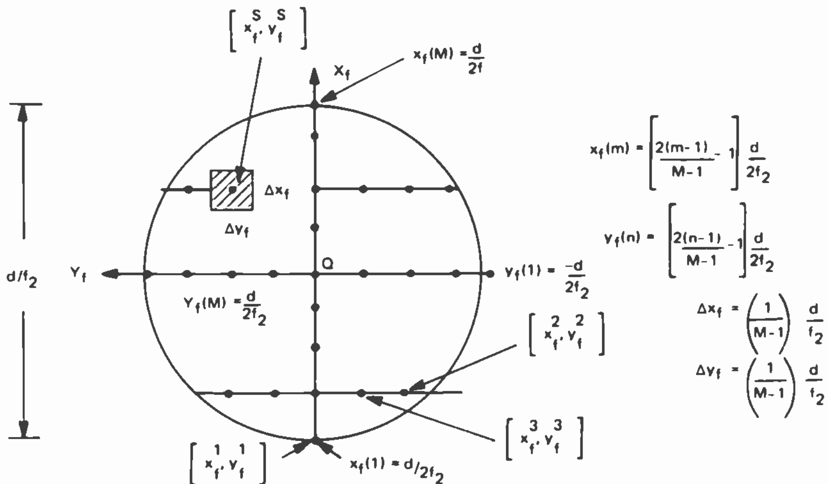

Fig. 4—Subdivision of feed aperture.

the sampling points can be expressed as

$$(x_f^t, y_f^t) = \left\{ [x_f(m), y_f(n)] \| \, t = 1, 2, \cdots, \sum_{m=1}^{M} \left(\sum_{n=1}^{M} \right) \right\} \qquad [7]$$

for those m, n that satisfy Eq. [4]. Note that in Eq. [7], the bracketed summation $\sum_{n=1}^{M}$ varies faster. Superscript t counts all the sampling points that satisfy Eq. [4].

The feed aperture amplitude assumes the following form:

$$E_1(t) = \left[1 - \frac{(x_f^t)^2 + (y_f^t)^2}{(d/2f_2)^2} \right]^K + C. \qquad [8]$$

K and C are preassigned constants; K controls taper and C controls the taper edge level. $K = 0$, $C = 0$ corresponds to a uniform distribution; $K = 1$, $C = 0$ is a $(1 - \rho^2)$ distribution.

The linear phase shift term of the feed can be expressed as

$$\Phi_f^t = \frac{2\pi}{\lambda} (x_f^t \sin\theta_s \cos\phi_s + y_f^t \sin\phi_s \sin\theta_s) \qquad [9]$$

where θ_s and ϕ_s are the scanning angles of the feed. By transformation relation [3], one obtains

$$x_f^t = x_A^t + h \text{ and } y_f^t = y_A^t, \qquad [10]$$

where subscript A denotes point A in Fig. 3. Hence,

$$\Phi_f^t = \frac{2\pi}{\lambda} [(x_A^t + h)\sin\theta_s \cos\phi_s + y_A^t \sin\phi_s \sin\theta_s]. \qquad [11]$$

Note that in Eq. [8], x_f^t and y_f^t are normalized (dividing by f_2), but in Eqs. [9], [10], and [11] they are not normalized.

2.2. Focal Aperture Field Computation

The phase distribution over the focal-plane aperture defined by Φ_F^t is the sum of the linear phase-shift term applied to the feed and the phase difference from the path length $L(t)$. $L(t)$ is computed by ray-tracing techniques (see Appendix.)

$$L(t) = |\,\mathbf{AB}\,| + |\,\mathbf{BC}\,| + |\,\mathbf{CD}\,| \qquad [12]$$

$$\begin{aligned} \Phi_F^t &= \Phi_f^t + \frac{2\pi}{\lambda} L(t) \\ &= \frac{2\pi}{\lambda} \{\sin\theta_s[(x_A^t + h)\cos\phi_s + y_A^t \sin\phi_s] + L(t)\}. \end{aligned} \qquad [13]$$

By ray optics approximation,[3] the focal aperture field $E_2(t)$ is related

to the feed amplitude $E_1(t)$ by

$$[E_1(t)]^2 \Delta x_f \Delta y_f = [E_2(t)]^2 \Delta x_D{}^t \Delta y_D{}^t, \tag{14}$$

where $\Delta x_D{}^t \Delta y_D{}^t$ is the area of the tth subcell of the focal aperture. Therefore

$$E_2(t) = \frac{E_1(t)}{\sqrt{\Delta x_D{}^t \Delta y_D{}^t}} \frac{1}{(M-1)} \frac{d}{f_2}. \tag{15}$$

2.3 Determination of $\Delta x_D{}^t$ and $\Delta y_D{}^t$

In general, the field points on the focal aperture are not linearly distributed, and the area of each subcell can be determined by approximation. Five adjacent focal aperture field points (t, t_1, t_2, t_3, t_4) are shown in Fig. 5. First, each feed point of the feed array is preassigned with a set of unique indexes (r, c), which specifies the location of the feed point with respect to a fixed reference. For instance, (r, c) denotes that the feed point of the feed array is the rth row and cth column from a fixed reference. After double reflection, each of the focal-aperture field points still retains the originally assigned location indexes. Let (r, c) and (r_3, c_3) be the location indexes for the tth and t_3th focal aperture field points. By scanning up and down and left and right from the tth field point (see Fig. 5) on the focal aperture, one can match the indexes such that $r_3 - r = 1$, $c - c_3 = 1$. Once this condition is reached, $\Delta x_D{}^t \, \Delta y_D{}^t$ is computed as follows:

$$\Delta x_D{}^t = x_D{}^{t_3} - x_D{}^t$$
$$\Delta y_D{}^t = y_C{}^{t_3} - y_D{}^t. \tag{16}$$

Note that t_1, t_2, and t_4 can as well be used as reference point for the computation of $\Delta x_D{}^t \, \Delta y_D{}^t$.

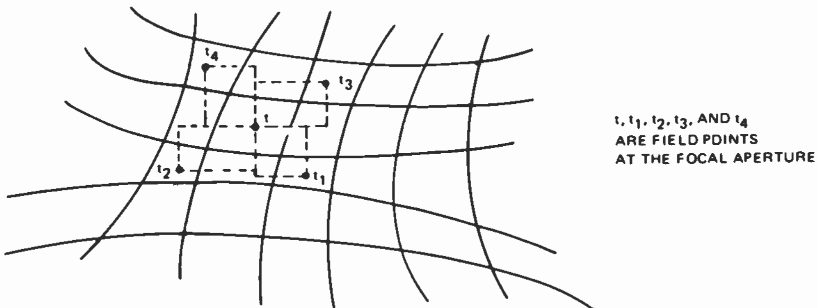

Fig. 5—Subdivision of focal aperture.

2.4 Constraint Posed by the Main Reflector and Subreflector

The subreflector is confined by a cylinder

$$(x + h_2)^2 + y^2 = (d_2/2)^2. \qquad [17]$$

Dividing Eq. [17] by f_2^2.

$$\left(\frac{x}{f_2} + \frac{h_2}{f_2}\right)^2 + \left(\frac{y}{f_2}\right)^2 = \left(\frac{d_2}{2f_2}\right)^2. \qquad [18]$$

Therefore, (x_B, y_B), the subreflector coordinates, must satisfy

$$\left(\frac{x_B}{f_2} + \frac{h_2}{f_2}\right)^2 + \left(\frac{y_B}{f_2}\right)^2 \leq \left(\frac{d_2}{2f_2}\right)^2. \qquad [19]$$

Similarly, the main reflector is confined by a cylinder

$$\left[x - \left(\frac{f_1}{f_2}\right)h\right]^2 + y^2 = \left[\left(\frac{f_1}{f_2}\right)\frac{d}{2}\right]^2. \qquad [20]$$

Dividing Eq. [20] by f_1^2,

$$\left[\frac{x}{f_1} - \left(\frac{h}{f_2}\right)\right]^2 + \left(\frac{y}{f_1}\right)^2 = \left(\frac{d}{2f_2}\right)^2. \qquad [21]$$

Therefore, (x_c, y_c), the main dish coordinates, must satisfy

$$\left(\frac{x_c}{f_1} - \frac{h_2}{f_2}\right)^2 + \left(\frac{y_c}{f_1}\right)^2 \leq \left(\frac{d}{2f_2}\right)^2. \qquad [22]$$

During the ray-tracing process, only those sampling points satisfying Eqs. [19] and [22] are retained.

2.5 Far-Field Computation

By scalar diffraction theory,[4] the far-field term U_p can be approximated by (see Fig. 6)

$$U_p \approx \frac{jk}{4\pi R} \exp\{-jkR\} \cdot (1 + \cos\theta) \int_A U \exp\{jk\rho \cdot \hat{R}_1\}\, ds. \qquad [23]$$

For small values of θ, the obliquity factor $(1+\cos\theta)$ can be approximated by a constant. Therefore, $(1+\cos\theta)$ can be dropped for computing the relative gain. In terms of series summation

$$U_p \approx \sum\sum U \exp\{jk\rho \cdot \hat{R}_1\} \Delta x_s \Delta y_s. \qquad [24]$$

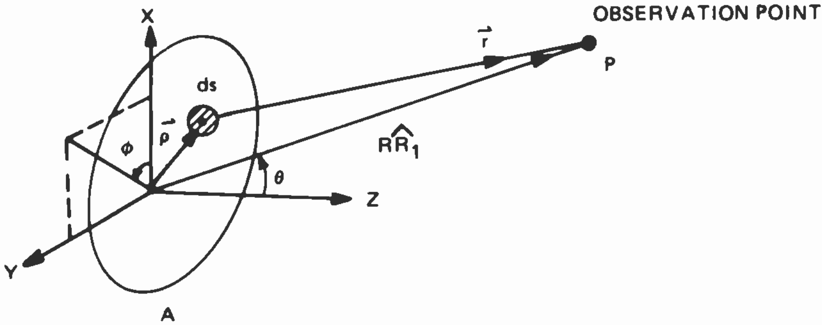

Fig. 6—Scalar diffraction geometry.

Applying Eq. [24] to obtain the far-field pattern $P(\theta, \phi)$, we have

$$U_p = P(\theta, \phi) \quad [25]$$

$$U = E_2(t)\exp\{-j\Phi_f^t\} \quad [26]$$

$$\Delta D_t = \Delta x_s \Delta y_s = \Delta x_D{}^t \Delta y_D{}^t \quad [27]$$

Since ρ lies on the main aperture, $Z_D{}^t = 0$ and therefore

$$\rho \cdot \hat{R}_1 = x_D{}^t \sin\theta \cos\phi + y_D{}^t \sin\theta \sin\phi + z_D{}^t \cos\theta = x_D{}^t \sin\theta \cos\phi + y_D{}^t \sin\theta \sin\phi \quad [28]$$

Substituting Eqs. [25], [26], [27], and [28] into Eq. [24]:

$$|P(\theta, \phi)| = \left| \sum_t \Delta D_t E_2(t) \exp\left\{ j\left[\frac{2\pi}{\lambda} \sin\theta (x_D{}^t \cos\phi + y_D{}^t \sin\phi) - \Phi_F{}^t \right] \right\} \right|, \quad [29]$$

where Φ_f^t and $E_2(t)$ are given by Eqs. [11] and [15], respectively.

2.6 Gain Formulation

Let G_{system} be the gain of the antenna system (Gregorian reflectors), G_{array} be the gain of the feed array (feed planar aperture), and $M = f_1/f_2$ be the magnification of the Gregorian reflectors. Then

$$G_{system} = M^2 G_{array}$$

where $G_{array} = 4\pi A/\lambda^2$, A = area of feed aperture, and [30]

λ = wavelength.

For any scan of the feed array, the maximum of its absolute far-field

value is

$$E_{max} = \left| \sum_{t=1}^{T} B_t \exp\{j\Phi_t\} \right|_{\Phi_t \text{ at beam max.}} \qquad [31]$$

where $t = 1, 2, \cdots, T$ (T = total number of aperture cells in the focal plane) and $B_t = E_2(t)\Delta D_t$ and Φ_t are given by Eq. [29].

For uniform illumination without phase scan, the total far field would be

$$E_{total} = \left| \sum_{t=1}^{T} B_t \right| = \left| \sum_{t=1}^{T} E_2(t)\Delta D_t \right|. \qquad [32]$$

Therefore, the antenna efficiency can be expressed as

$$\eta_a = \left(\frac{E_{max}}{E_{total}}\right)^2 = \left[\frac{\left| \sum_{t=1}^{T} B_t \exp\{j\Phi_t\} \right|_{\Phi_t \text{ at beam max.}}}{\sum_{t=1}^{T} E_2(t)\Delta D_t} \right]^2. \qquad [33]$$

Then for any scan, the gain of the Gregorian reflectors can be expressed as

$$G_s = \eta_a G_{system}, \qquad [34]$$

and the scan loss will be

$$L_s = -(G_{system} - G_s). \qquad [35]$$

3. Program Description

A computer program was developed to analyze the offset near-field Gregorian antenna. A schematic of the offset near-field Gregorian antenna is shown in Fig. 7.

The listed variables in Fig. 7 are input variables except DTF, DEFF, and MAG which are determined from the input variables. The input variables are:

Main reflector:

$F1$ = Main reflector (paraboloid) focal length in inches.

Subreflector:

$F2$ = Subreflector (paraboloid) focal length (in inches).
$D2$ = Effective diameter of the subreflector (in inches).
$H2$ = Displacement of the effective center of the subreflector from the Z-axis (in inches).

Feed aperture:

D = Diameter of the circular feed aperture (in inches).

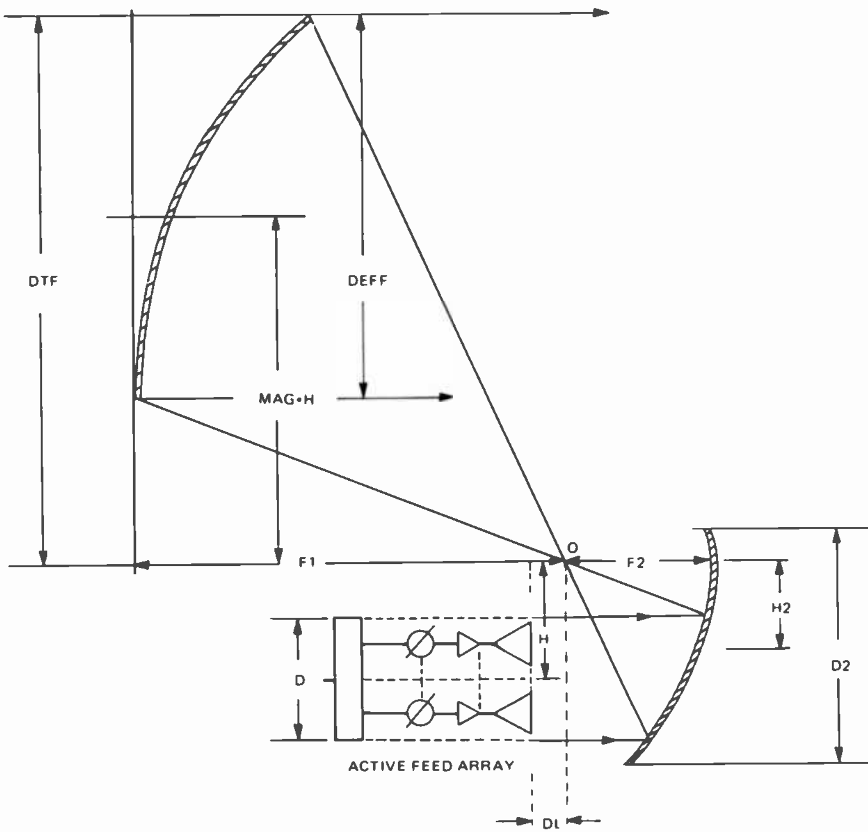

Fig. 7—Schematic description of the offset near-field Gregorian antenna.

H = Displacement of the center of the feed aperture from the Z-axis (in inches).

DL = Displacement of the center of the feed aperture from the confocal point 0 (in inches).

K = Feed array illumination coefficient (refer to Eq. [8]). K controls taper of illumination.

C = Feed array illumination coefficient (refer to Eq. [8]). C controls the taper edge level.

$K = 0$, $C = 0$ corresponds to a uniform distribution whereas $K = 1$, $C = 0$ is a $(1 - \rho^2)$ distribution.

Operation parameter:

FREQ = Frequency of operation (in GHz).

The derived variables are listed as follows:

MAG = Linear magnification factor, MAG = $F1/F2$.

DEFF = Effective diameter of the main reflector, DEFF = MAG $*$ D.

DTF = Height of the main reflector measured from the upper tip of the main reflector to the focal axis DTF = MAG*(H + 0.5 * D).

4. Results

Typical near-field Gregorian patterns computed for a 34-ft-diameter main reflector operating at 3.9 GHz are shown in Fig. 8. The parameters are:

$F1/F2 = 3.0$

$F2/\lambda = 52.5$

$D/F2 = 0.87$

$D2/F2 = 1.60$

$H/F2 = 0.79$

$H2/F2 = 0.60$

$DL/F2 = 0.23$

Tabulated gain and scan loss data are presented for this antenna in Table 1, with feed-array scan angle as a parameter. Scan loss versus array scan angle (ϕ_s = 0°, vertical plane) is shown in Fig. 9. In the

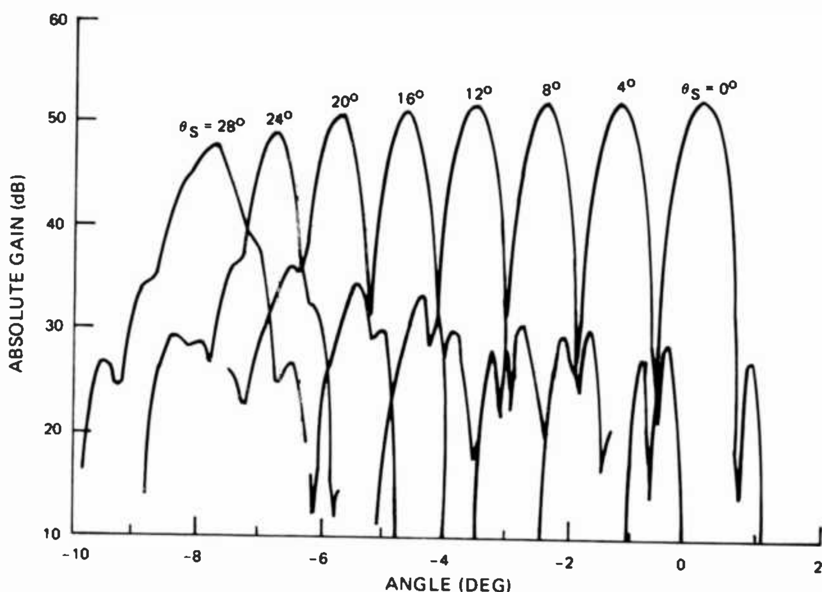

Fig. 8—Computer gain patterns of scanned-beam vertical-plane patterns.

Table 1—Antenna Gain and Scan Loss of Scanned Beam.

Feed-Array Scan Angles (θ_s, ϕ_s)	Antenna Gain (dB)	Scan Loss L_s (dB)	Antenna Efficiency	Antenna Pattern Scan Angles (θ, ϕ)
(0°, 0°)	52.497	0	1.000	(0°, 0°)
(4°, 0°)	52.489	−0.008	0.998	(−1.3°, 0°)
(8°, 0°)	52.453	−0.044	0.990	(−2.5°, 0°)
(12°, 0°)	52.205	−0.292	0.935	(−3.6°, 0°)
(16°, 0°)	51.802	−0.695	0.852	(−4.7°, 0°)
(20°, 0°)	50.995	−1.501	0.708	(−5.8°, 0°)
(24°, 0°)	49.75	−2.747	0.531	(−6.8°, 0°)
(28°, 0°)	47.932	−4.565	0.349	(−7.8°, 0°)

above analysis, *MM*1, the number of the sampling points along the diameter of the feed array, is assumed to be 15. Better results are anticipated when higher values of *MM*1, e.g., 30, are used.

The analysis thus far has demonstrated the scanning capabilities of the three-dimensional offset near-field Gregorian antenna. It is based on ray-tracing techniques and scalar diffraction theory, where we assume that the fields in the near-field region of the fed aperture are accurately determined by ray optics. Therefore, the treatment of the antenna is essentially a geometric optics approach.

However, the geometric optics method, commonly used to analyze reflector antennas, is a high-frequency approximation method and is accurate only when the feed and the reflectors are very large compared to the wavelength. The plane-wave spectrum method, which includes

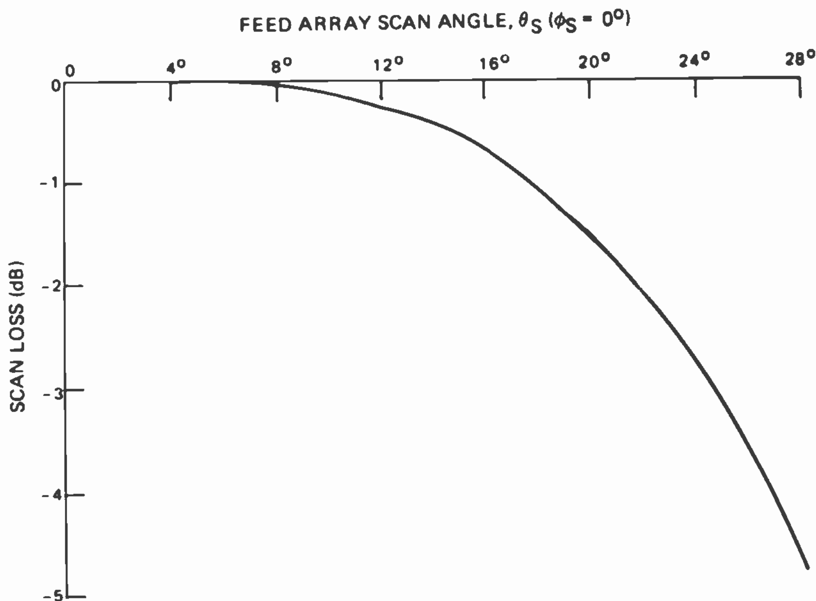

Fig. 9—Scan loss versus array scan angle (ϕ_S = 0°, vertical plane).

frequency dependence, will provide better accuracy than the geometric optics method, and this method will now be discussed.

5. Plane-Wave Spectrum (PWS) Method For The Near-Field Offset Gregorian Reflectors

5.1 Theory

It has been shown by Booker and Clemmow[5] that any electromagnetic field can be represented by a superposition of plane waves including inhomogeneous waves, commonly described as surface waves. The amplitude of these waves can be determined using the Fourier integral technique if either the electric field or the magnetic field is known over the aperture plane.

For a y-polarized field (Fig. 10) the aperture distribution $E_y(x, y, 0)$ is given by[6]

$$E_y(x, y, 0) = \frac{1}{\lambda^2} \int_{-\infty}^{\infty} \int_{-\infty}^{\infty} F(S_1, S_2) \exp\{-jk(S_1 x + S_2 y)\}\, dS_1\, dS_2 \quad [36]$$

where $F(S_1, S_2)$ is the Fourier transform of $E_y(x, y, 0)$ given by

$$F(S_1, S_2) = \int_{-\infty}^{\infty} \int_{-\infty}^{\infty} E_y(x, y, o) \exp\{jk(S_1 x + S_2 y)\}\, dx\, dy \quad [37]$$

where $S_1 = \sin\theta \cos\phi$, and $S_2 = \sin\theta \sin\phi$.

To satisfy Maxwell's equations, the electric field can be expressed in terms of $F(S_1, S_2)$ as[6]

$$\mathbf{E}(x, y, z) = \frac{1}{\lambda^2} \int_{-\infty}^{\infty} \int_{-\infty}^{\infty} (C\, \hat{a}_y - S_2 \hat{a}_z)\, F(S_1, S_2) \exp\{-jk(S_1 x + S_2 y + cz)\}(dS_1 dS_2)/C \quad [38]$$

where $C^2 = 1 - S_1^2 - S_2^2$ and $\hat{a}_y$, $\hat{a}_z$ are the unit vectors in the directions of y and z axes, respectively.

5.2 Equivalence of PWS Formulation and Conventional Aperture Integration Method

By conventional aperture integration method, the electric field of an aperture antenna with only the magnetic current density **M** is given in

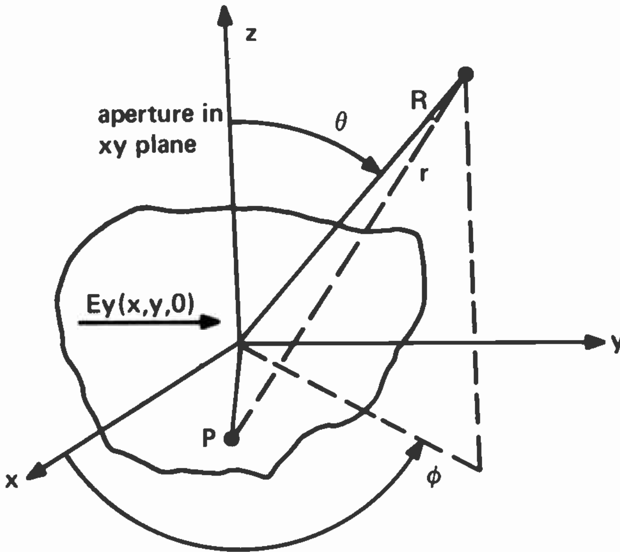

Fig. 10—Coordinate system showing the aperture in xy plane.

Ref. 7. **J** = 0 for an electric conductor; hence,

$$\mathbf{E} = \frac{-1}{4\pi} \iint_s \mathbf{M} \times \nabla\psi \, dA$$
$$= \frac{1}{4\pi} \iint \left(jk + \frac{1}{r}\right) \mathbf{M} \times \hat{r}(\exp\{-jkr\})/r \, dA \quad [39]$$

where $\hat{r}$ is the unit vector along r, $\psi = (\exp\{-jkr\})/r$.

The integral representation of the scalar free-space Green's function if given by[8, 9]

$$\exp\{-jkr\}/r = \frac{1}{2\pi j} \iint_{-\infty}^{\infty} \frac{1}{k_z^*} \exp\{-j[k_x(x - x')$$
$$+ k_y(y - y') + k_z^* z]\} dk_x dk_y \quad [40]$$

where $k = 2\pi/\lambda = \sqrt{k_x^2 + k_y^2 + k_z^2}$ is the free space propagation constant, and

$$k_x = k \sin\theta\cos\phi$$
$$k_y = k \sin\theta\sin\phi$$
$$k_z = k \cos\theta \quad [41]$$
$$k_z = \begin{cases} \sqrt{k^2 - k_x^2 - k_y^2} & \text{if } k_x^2 + k_y^2 < k^2 \\ -j\sqrt{k_x^2 + k_y^2 - k^2} & \text{if } k_x^2 + k_y^2 \geq k^2 \end{cases}$$

Substituting Eq. [40] into [39].

$$\mathbf{E} = \frac{-1}{4\pi} \iint \mathbf{M} \times \nabla\, (\exp\{-jkr\})/r\; dA$$

$$= \frac{-1}{8\pi^2 j} \iint_S \iint_{-\infty}^{\infty} \frac{1}{k_z} \mathbf{M}$$

$$\times \nabla \exp\{-j[k_x(x - x') + k_y(y - y') + k_z^* z]\} dk_x dk_y$$

where * stands for complex conjugate.
Hence,

$$\mathbf{E} = \frac{1}{8\pi^2} \iint_S \iint_{-\infty}^{\infty} \frac{1}{k_z^*}$$

$$\exp\{-j[k_x(x - x') + k_y(y - y') + k_z z]\}\mathbf{k} \qquad [42]$$

$$\times \mathbf{M}(x', y')\; dk_x\; dk_y\; dx'\; dy'$$

The equivalent magnetic current density for the field of an aperture in an infinite ground plane can be expressed in terms of the aperture electric field as

$$\mathbf{M}(x', y') = 2\,\mathbf{E} \;\; | \;\times \hat{n}_{\text{at the aperture}} \qquad [43]$$

where the unit normal vector $\hat{n}$ in this case is the unit vector $\hat{a}_z$. The factor *2* in Eq. [43] is due to the use of image theory together with the equivalence principle.

E at the aperture is given to be y polarized; therefore, $\mathbf{M}(x', y')$ the magnetic current density is x polarized.

$$\mathbf{E}|_{\text{at the aperture}} = E_y(x', y')\hat{a}_y \qquad [44]$$

Hence, Eq. [42] reduces to

$$\mathbf{E} = \frac{1}{4\pi^2} \iint_S \iint_{-\infty}^{\infty} \frac{1}{k_z^*} \exp\{-j[k_x(x - x') + k_y(y - y')$$

$$+ k_z z]\}(k_x\hat{a}_x + k_y\hat{a}_y + k_z\hat{a}_z)$$

$$\times \hat{a}_x E_y(x', y')\; dk_x\; dk_y\; dx'\; dy' \qquad [45]$$

$$= \frac{1}{4\pi^2} \iint_{-\infty}^{\infty} \frac{1}{k_z^*} \exp\{-j(k_x x + k_y y + k_z z)\}$$

$$(k_z\hat{a}_y - k_y\hat{a}_z)F(k_x, k_y)\; dk_x\; dk_y$$

where $F(k_x, k_y)$ the angular spectrum of the plane wave is the Fourier transform of the aperture electric field $E_y(x', y')$ and is given by

$$F(k_x, k_y) = \iint_S E_y(x', y')\exp\{j(k_x x' + k_y y') \, dx' \, dy' \qquad [46]$$

Equation [45] is the PWS formulation for the fields of an aperture distribution E_y. Thus the equivalence of PWS formulation and the conventional aperture integration method is verified.

6. Feed Modeled by the PWS Method

6.1 Formulation of the Problem

M. Chen and G. Tsandoulas employed the PWS method to study the boresight gain of the near-field offset Gregorian reflectors.[10] The geometric optics method is a high-frequency approximation method and is accurate only when the feed and reflectors are very large compared to the wavelength. The plane-wave spectrum method includes frequency dependence and gives greater gain loss toward the lower frequencies because of the presence of essentially divergent input plane waves in the field expansion (see Fig. 11).

Let $E_y(x')$, a y-polarized electric field, be the feed source at the feed

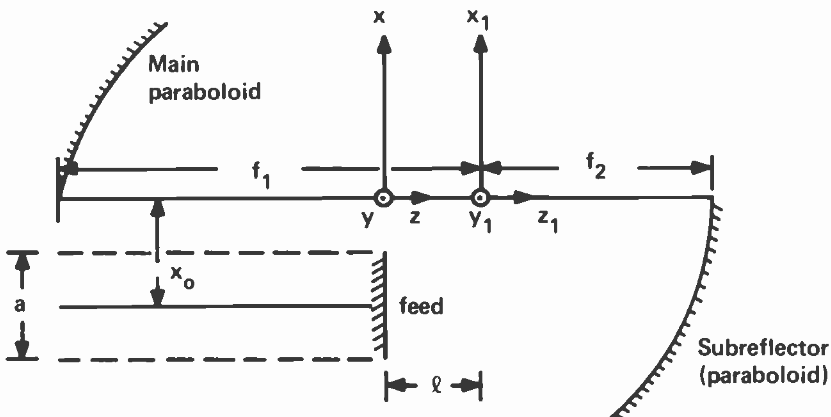

Fig. 11—Offset Gregorian reflector with feed modeled by PWS method.

array aperture. For the two-dimensional analysis, Eq. [45] reduces to

$$E_y(x, z) = \frac{1}{2\pi} \int_{-\infty}^{\infty} F(k_x) \exp\{-j(k_x x + k_z z)\}\, dk_x \quad [47a]$$

$$F(k_x) = \int_{x_0-(a/2)}^{x_0+(a/2)} E_y(x') \exp\{jk_x x'\}\, dx' \quad [47b]$$

where $k_x^2 + k_z^2 = k^2$, $k_z = \sqrt{k^2 - k_x^2}$, and k_z is real if $k_x < k$.

For a uniform illuminated aperture

$$E_y(x') = 1,\ x_0 - \frac{a}{2} \le x' \le x_0 + \frac{a}{2}. \quad [48]$$

Substituting Eq. [48] into [47b],

$$F(k_x) = \int_{x_0-(a/2)}^{x_0+(a/2)} \exp\{jk_x x'\}\, dx' = \int_{x_0-(a/2)}^{x_0+(a/2)} \cos k_x x'\, dx'$$

$$= \frac{\sin k_x x'}{k_x} \Bigg|_{x_0-(a/2)}^{x_0+(a/2)}$$

$$= \frac{\sin k_x[x_0 + (a/2)] - \sin k_x[x_0 - (a/2)]}{k_x},$$

that is,

$$F(k_x) = \frac{2 \sin[k_x(a_0/2)]\cos(k_x x_0)}{k_x}$$
$$= [\cos(k_x x_0)] \frac{\sin[k_x(a_0/2)]}{k_x/2}. \quad [49]$$

Put Eq. [49] into [47a]:

$$E_y(x, z) = \frac{1}{2\pi} \int_{-\infty}^{\infty} [\cos(k_x x_0)]$$
$$\frac{\sin[k_x(a_0/2)]}{k_x/2} \exp\{-j(k_x x + k_z z)\}\, dk_x. \quad [50]$$

When $E_y(x, z)$ is evaluated at (x', o), theoretically we will get $E_y(x')$ $= 1$ provided that the limits of integral are from $k_x = -\infty$ to $k_x = \infty$. However, if we truncate Eq. [50] by varying the limits of integral from $k_x = -k$ to $k_x = k$, we can filter off some of the unwanted spectrum of

the plane wave. Eq. [50] can be expressed in series form:

$$E_y(x, z) = \sum_{n=1}^{N} F(k_{x_n})\exp\{-j(k_{x_n}x + \sqrt{k^2 - k_{x_n}^2}z)\}\Delta k_{x_n} \qquad [51]$$

where

$$F(k_{x_n}) = \cos(k_{x_n}x_0)\frac{\sin k_{x_n}(a_0/2)}{k_{x_n}/2},$$

n is the nth interval, and N is the total number of intervals chosen.

If we limit k_x to be in the range $(-k, k)$, the surface waves (unwanted wave spectrum) are filtered off (Fig. 12). Then

$$\Delta k_{x_n} = \frac{2k}{N}, \qquad k = \frac{\pi}{\lambda}. \qquad [52]$$

If we limit the coverage to $-60° \leq \Theta \leq 60°$, which is adequate for the analysis,

$$k_x = k \sin 60° = 0.866\ k \text{ and}$$

$$\frac{\Delta k_{x_n}}{2} = \frac{0.866k}{N} \qquad [53]$$

6.2 General Procedure for Solving the Problem

Refer to Fig. 13. Let A be the phase center of the plane-wave spectrum. E_{A_0} is the component of the plane-wave spectrum corresponding to $\theta = 0°$ and E_A' is the component of plane-wave spectrum corresponding to $\theta = \theta_i$.

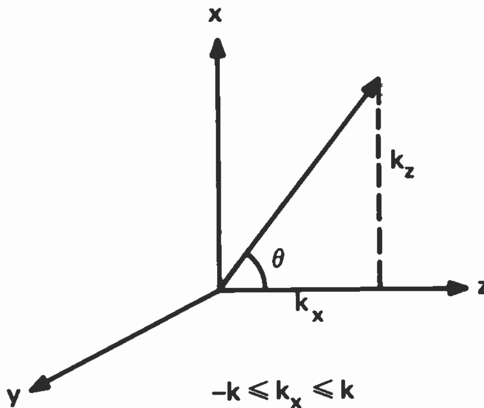

Fig. 12—Region of k_x.

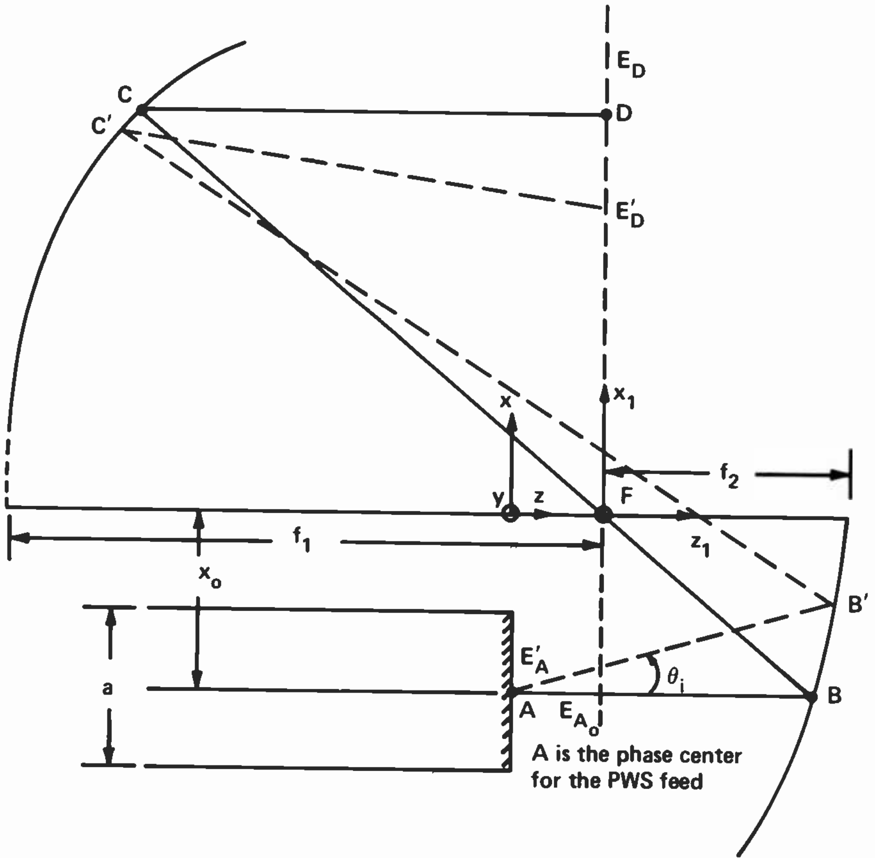

Fig. 13—Ray-tracing technique for near-field Gregorian reflector with PWS feed.

Each component of the plane-wave spectrum is treated as input to the Gregorian system. By the ray-tracing technique (see Fig. 13), we can make the following assumptions concerning the range of the plane-wave and spherical-wave propagation:

$$\left\{\begin{matrix} AB' \\ AB \end{matrix}\right\} \text{ plane-wave range,}$$

$$\left\{\begin{matrix} B'C' \\ BC \end{matrix}\right\} \text{ spherical-wave range, and}$$

$$\left\{\begin{matrix} C'D' \\ CD \end{matrix}\right\} \text{ plane-wave range.}$$

Hence, we have

$$E_D \approx \frac{E_{A_0}}{|BC|}, \qquad E_{A_0} = \text{aperture field at } \theta = 0^\circ$$
$$E_D' \approx \frac{E_A'}{|B'C'|}, \qquad E_A' = \text{aperture field at } \theta = \theta_i \qquad [54]$$

where

$$\mathbf{E_A} = E_{A_0} \angle 0^\circ + E_A' \angle \theta_i + \cdots \qquad [55]$$

From Fig. 14 the far field at point P can be expressed as

$$E_p \approx c \int E_D' \psi \, dx_1 \quad \text{(collapsed to line source)} \qquad [56]$$

where c is a constant and

$$\psi \approx \frac{\exp\{-jkR'\}\exp\{jk(x' \cos\theta \cos\phi)\}}{R'}. \qquad [57]$$

7. Conclusion

The offset near-field Gregorian antenna, with equivalently longer focal length in a physically compact geometry and an electronically steerable phased array feed providing a limited scan capability, is potentially suitable for earth coverage from a geosynchronous communications satellite. A conventional equivalent parabola technique cannot be applied in a straightforward manner to predict the scan loss and pattern shape for this kind of dual-offset-fed reflector antenna.

In this paper, a geometric optics solution for the offset near-field Gregorian antenna was assumed. The analysis employed geometric optics ray-tracing techniques to transform feed-array amplitude and phase distributions into near-field Gregorian aperture distributions. The beam scanning characteristics then follow by using the reflector aperture field integration techniques.

The geometric optics method, however, is a high-frequency approximation accurate only when the feed and the reflectors are very large compared to wavelength. The plane-wave spectrum (PWS) method, which includes frequency dependence, will provide better accuracy than the geometric optics method. A preliminary study of the PWS method applied to the near-field offset Gregorian reflector is included. Plane waves are treated as inputs to the feed array. With one plane wave incident on the subreflector, a corresponding field distribution on the main reflector aperture is obtained by the ray-tracing technique. Superposing the contribution from N plane waves, one obtains the total field in the main reflector aperture for subsequent radiation pattern computation.

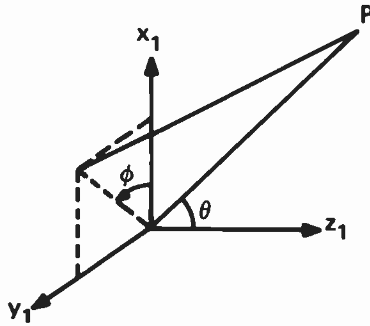

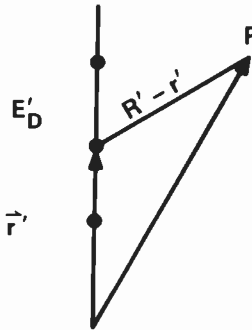

$$\psi = \frac{e^{-j\vec{k}\cdot(\vec{R}'-\vec{r}')}}{\vec{R}'-\vec{r}'}$$

$$\approx \frac{e^{-jkR'}e^{jk[x'\cos\theta\ \cos\phi]}}{R'}$$

far-field approximation

Fig. 14—Far-field computation.

Acknowledgements

The author wishes to express his gratitude to C. E. Profera for his suggestions, support, and encouragement. The author also wishes to thank his colleagues, and particularly Daniel V. Wylde, for useful discussions.

Appendix—Ray-Tracing Technique

Referring to Fig. 3, the path length is given by

$$L(t) = |\mathbf{AB}| + |\mathbf{BC}| + |\mathbf{CD}|. \quad [58]$$

$(x_A, y_A, -l)$, (x_B, y_B, z_B), (x_C, y_C, z_C), and $(x_D, y_D, 0)$ designate points A, B, C, and D, respectively.

$$\mathbf{AB} = (x_B - x_A)\hat{a}_x + (y_B - y_A)\hat{a}_y + (z_B + l)\hat{a}_z. \quad [59]$$

$$\widehat{AB} = \mathbf{AB}/|\mathbf{AB}|. \quad [60]$$

$\widehat{AB}$ is a unit vector in the direction of **AB**. In terms of the scan angles θ_s and ϕ_s, $\widehat{AB}$ can be expressed as

$$\widehat{AB} = \sin\theta_s\cos\phi_s\hat{a}_x + \sin\theta_s\sin\phi_s\hat{a}_y + \cos\theta_s\hat{a}_z. \quad [61]$$

Solving Eqs. [60] and [61], one obtains

$$(x_B - x_A)\tan\phi_s = y_B - y_A \quad [62]$$

$$\frac{x_B - x_A}{\tan\theta_s\cos\phi_s} = (z_B + l). \quad [63]$$

From Eq. [2], the subdish is described by

$$z_B = f_2 - \frac{x_B^2 + y_B^2}{4f_2}. \quad [64]$$

Solving Eqs. [62], [63], and [64] yields point B of the subdish as follows:

$$x_B = \frac{-\beta \pm \sqrt{\beta^2 - 4\alpha\gamma}}{2\alpha} \quad [65]$$

$$y_B = y_A + (x_B - x_A)\tan\phi_s \quad [66]$$

$$z_B = f_2 - \frac{x_B^2 + y_B^2}{4f_2} \quad [67]$$

where

$$\alpha = 1 + \tan^2\phi_s \quad [68]$$

$$\beta = 2y_A\tan\phi_s - 2x_A\tan^2\phi_s + \frac{4f_2}{\tan\theta_s\cos\phi_s} \quad [69]$$

$$\gamma = y_A^2 + x_A^2\tan^2\phi_s - \frac{4f_2x_A}{\tan\theta_s\cos\phi_s} - 4f_2(f_2 + l) - 2x_Ay_A\tan\phi_s. \quad [70]$$

By applying Snell's law of reflection at point B, one obtains

$$\widehat{BC} = \widehat{AB} - 2\hat{N}_s(\hat{N}_s \cdot \widehat{AB}). \quad [71]$$

The unit normal of the subdish is

$$\hat{N}_s = -\frac{1}{\Delta_s}(x_B\hat{a}_X + y_B\hat{a}_y + 2f_2\hat{a}_z) \quad [72]$$

where

$$\Delta_s = \sqrt{x_B^2 + y_B^2 + 4f_2^2}. \quad [73]$$

By substituting $\hat{N}_s$ and $\widehat{AB}$ into Eq. [71], the components of $\widehat{BC}$ follow as

$$\widehat{BC}_x = \sin\theta_s\cos\phi_s - \frac{2x_B}{(\Delta_s)^2}\sigma_s \quad [74]$$

$$\widehat{BC}_y = \sin\theta_s\sin\phi_s - \frac{2y_B}{(\Delta_s)^2}\sigma_s \quad [75]$$

$$\widehat{BC}_z = \cos\theta_s - \frac{4f_2}{(\Delta_s)^2}\sigma_s \quad [76]$$

where

$$\sigma_s = x_B\sin\theta_s\cos\phi_s + y_B\sin\theta_s\sin\phi_s + 2f_2\cos\theta_s. \quad [77]$$

By definition

$$\widehat{BC} \equiv \frac{\mathbf{BC}}{|\mathbf{BC}|} = \frac{(x_C - x_B)\hat{a}_x + (y_C - y_B)\hat{a}_y + (z_C - z_B)\hat{a}_z}{\sqrt{(x_C - x_B)^2 + (y_C - y_B)^2 + (z_C - z_B)^2}} \quad [78]$$

Equating Eqs. [74], [75], and [76] to [78], one obtains

$$\frac{\widehat{BC}_y}{\widehat{BC}_x}(x_C - x_B) = y_C - y_B \quad [79]$$

$$\frac{\widehat{BC}_z}{\widehat{BC}_x}(x_C - x_B) = z_C - z_B \quad [80]$$

From Eq. [1], the main dish is described by

$$z_C = \frac{x_C^2 + y_C^2}{4f_1} - f_1. \quad [81]$$

Solving Eqs. [79], [80], and [81] yields point C of the main dish as

follows

$$x_C = \frac{-\delta \pm \sqrt{\delta^2 - 4\zeta\xi}}{2\zeta} \quad [82]$$

$$y_C = y_B + \frac{\widehat{BC}_y}{\widehat{BC}_x}(x_C - x_B) \quad [83]$$

$$z_C = \frac{x_C^2 + y_C^2}{4f_1} - f_1, \quad [84]$$

where

$$\delta = 2y_B\frac{\widehat{BC}_y}{\widehat{BC}_x} - 2x_B\left(\frac{\widehat{BC}_y}{\widehat{BC}_x}\right)^2 - 4f_1\frac{\widehat{BC}_z}{\widehat{BC}_x} \quad [85]$$

$$\zeta = 1 + \left(\frac{\widehat{BC}_y}{\widehat{BC}_x}\right)^2 \quad [86]$$

$$\xi = 4f_1x_B\frac{\widehat{BC}_z}{\widehat{BC}_x} - 2x_By_B\frac{\widehat{BC}_y}{\widehat{BC}_x} + x_B^2\left(\frac{\widehat{BC}_y}{\widehat{BC}_x}\right)^2 + y_B^2 - 4f_1(f_1 + z_B). \quad [87]$$

By applying Snell's law of reflection at point C, one obtains

$$\widehat{CD} = \widehat{BC} - 2\,\widehat{N}_m(\widehat{N}_m \cdot \widehat{BC}). \quad [88]$$

The unit normal of the main dish is

$$\widehat{N}_m = \frac{-1}{\Delta_m}(x_C\hat{a}_x + y_C\hat{a}_y + 2f_1\hat{a}_z) \quad [89]$$

where

$$\Delta_m = \sqrt{x_C^2 + y_C^2 + 4f_1^2}. \quad [90]$$

Substituting $\widehat{N}_m$ and $\widehat{BC}$ Eqs. [89, 90, 74, 75, 76] into [88], the components of CD follow as

$$\widehat{CD}_x = \widehat{BC}_x - \frac{2x_C}{(\Delta_m)^2} \cdot \sigma_m \quad [91]$$

$$\widehat{CD}_y = \widehat{BC}_y - \frac{2y_C}{(\Delta_m)^2} \cdot \sigma_m \quad [92]$$

$$\widehat{CD}_z = \widehat{BC}_z + \frac{4f_1}{(\Delta_m)^2} \cdot \sigma_m \quad [93]$$

where

$$\sigma_m = x_C\widehat{BC}_x + y_C\widehat{BC}_y - 2f_1\widehat{BC}_z. \quad [94]$$

By definition

$$\widehat{CD} \equiv \frac{\mathbf{CD}}{|\mathbf{CD}|}$$

$$= \frac{(x_D - x_C)\hat{a}_x + (y_D - y_C)\hat{a}_y + (z_D - z_C)\hat{a}_z}{\sqrt{(x_D - x_C)^2 + (y_D - y_C)^2 + (z_D - z_C)^2}}. \quad [95]$$

By slight manipulation of Eq. [95], one arrives at

$$x_D = x_C - \frac{\widehat{CD}_x}{\widehat{CD}_z} z_C \quad [96]$$

$$y_D = y_C + \frac{\widehat{CD}_y}{\widehat{CD}_x}(x_D - x_C). \quad [97]$$

Since point D is at the focal aperture, $z_D = 0$. Point $A(x_A, y_A, -l)$ is arbitrarily assigned; coordinates B, C, and D follow as prescribed above. Thus $|\mathbf{AB}|$, $|\mathbf{BC}|$ and $|\mathbf{CD}|$ are determined.

References

[1] Communication Satellite Developments: Systems, Vol. 41, *Progress in Astronautics and Aeronautics*, 1976, published by the American Institute of Aeronautics and Astronautics in cooperation with the MIT press, p. 139.

[2] W. D. Fitzgerald, "Limited Electronic Scanning with an Offset Fed Near-Field Gregorian System," MIT Lincoln Labs, Tech. Report 486, Sept. 1971, DPC AD-736029.

[3] S. Silver, *Microwave Antenna Theory and Design*, McGraw-Hill Book Co., pp. 112–114, 1949.

[4] See Ref. [3], p. 165–167, Eq. 124.

[5] H. G. Booker and P. C. Clemmow, "The Concept of an Angular Spectrum of Plane Waves and Its Relation to That of Polar Diagram and Aperture Distribution," *Proc.* IEE, (1950), 97, Part III, p. 11.

[6] J. Brown, "Theoretical analysis of some errors in Aerial Measurement," IEE Monograph No. 285R, pp. 343–351, Feb. 1958.

[7] D. C. F. Wu and R. C. Rudduck, Electro Science Lab., Ohio State University, Columbia, Ohio, Final Report 2969-4, pp. 7–10, March 1971.

[8] E. Lalor, "Conditions for the validity of the angular spectrum of plane waves," *J. Opt. Soc. Am.*, **58**, no. 9, p. 1235, Sept. 1968.

[9] R. F. Harrington, *Time Harmonic Electromagnetic Field*, McGraw-Hill Book Co., Inc., New York, 1961, p. 188.

[10] M. H. Chen and G. N. Tsandoulas, "A Dual-Reflector Optical Feed for Wide-Band Phased Arrays," *IEEE Trans. Antennas Propag.*, **AP-22**, No. 4, p. 541, July 1974.

A Simplified Real Frequency Technique for Broadband Matching a Complex Generator to a Complex Load

B. S. Yarman
RCA Laboratories, Princeton, NJ 08540

Abstract—This paper presents a new computer-aided design procedure, a simplified "Real Frequency" technique, for the solution of the general matching problem. The design procedure requires no knowledge of the algebraic form of transfer function or circuit topology. Examples are given to show the merit of this technique over the analytic and other CAD procedures. An FET amplifier was designed employing the new technique and built successfully.

1. Introduction

In the design of communication networks, the fundamental problem is to realize lossless matching networks or equalizers so that the transfer of power from source to load is maximized over a prescribed frequency band. Here, the major problem is "double matching" power transfer from a complex generator to an arbitrary (complex) load (Fig. 1). In this paper, we introduce a new computer-aided design procedure, a simplified "real frequency" technique for double-matching problems, then present examples to show the merit of the technique. Finally, the design of an FET amplifier by this new method is discussed.

The method described here is an alternate version of the "direct computational" technique,[3] which is the generalized form of "real frequency matching" introduced by Carlin.[1,2] This new method has all the merits of these applications: (1) there is no need to choose an algebraic transfer function as a measure of performance; (2) it is not necessary to assume an equalizer topology in advance; (3) there is no

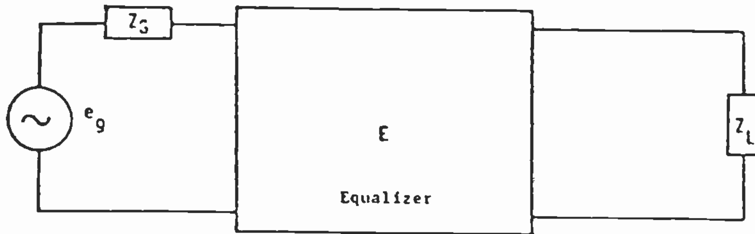

Fig. 1—Double matching problem.

need to determine an equivalent circuit for the devices; and (4) the real frequency or experimental data for the devices are processed directly. The final result is an optimized physically realizable real (or unit) normalized reflection coefficient (e_{11}) that describes the equalizer alone. In addition, as contrasted with Ref. [1]-[3], the new design procedure described here eliminates the need for numerical evaluation of the Hilbert transformation, since the use of minimum reactance or minimum susceptance immitance function to describe the lossless matching network is omitted. Thus the computational efficiency is significantly improved. Furthermore, just as in the other versions of the "real frequency" method, equalizers are generally simpler and have superior gain properties compared to structures obtained by the analytic procedure.[4]

2. Real Frequency Matching Via Scattering Approach

The heart of the technique resides in the generation of the real (or unit) normalized scattering parameters [$\{e_{ij}\}$, $i,j = 1, 2$] of the lossless equalizer E from the given (initialized) numerator polynomial $h(s)$ of the unit normalized input reflection coefficient $e_{11}(s) = h(s)/g(s)$. Later $h(s)$ will be chosen as the unknown and determined to optimize the transducer gain. For the sake of simplicity, E is assumed to be a minimum phase structure with transmission zero only at $\omega = \infty$, $\omega = 0$. Employing the well known Belevitch[5] representation, the scattering parameters $\{e_{ij}\}$ are written

$$e_{11}(s) = h(s)/g(s),\ e_{12}(s) = e_{21}(s) = \pm\, s^k/g(s) \qquad [1]$$
$$e_{22}(s) = -(-1)^k h(-s)/g(s),$$

where $k \geq 0$ is an integer. Since the matching network is lossless, it follows that

$$g(s)g(-s) = h(s)h(-s) + (-1)^k s^{2k}. \qquad [2]$$

The Hurwitz denominator polynomial $g(s)$ can explicitly be computed if $h(s)$ is known. Thus, employing Eq. [1], bounded-real (BR) scattering parameters $\{e_{ij}\}$ of the lossless equalizer E are generated from the initialized numerator polynomial $h(s) = h_0 + h_1 s + \cdots + h_n s^n$ of $e_{11}(s) = h(s)/g(s)$. Based upon the above discussion, the transducer power gain $T(\omega)$ of the doubly terminated structure (Fig. 1) may be generated as a function of e_{ij} and the complex terminations using the following algorithm.

Algorithm:

Computation of $T(\omega)$ from the given numerator polynomial $h(s)$ of the input reflection coefficient $e_{11}(s)$.

Inputs:

n = degree of polynomial $h(s) = h_0 + h_1 s + \cdots + h_n s^n$

k = degree of the numerator polynomial of $e_{21}(s) = e_{12}(s) = \mp s^k/g(s)$, where $k = 0$ for low pass ladder and $k > 0$ for bandpass ladder.

$h_0, h_1 \cdots, h_n$ = initialized real coefficients of $h(s)$

$S_G(j\omega)$ = real normalized reflection coefficient of the source network. $S_G(j\omega)$ is assumed to be BR, or corresponding $Z_G = (1 + S_G)/(1 - S_G)$ is positive real (PR).

$S_L(j\omega)$ = real normalized reflection coefficient of the load network. S_L is assumed to be BR or corresponding $Z_L = (1 + S_L)/(1 - S_L)$ is PR.

Computational Steps:

1. Generate the even polynomial $g(s)g(-s) = h(s)h(-s) + S^{2k} = G_0 + G_1 s + G_2 s^2 + \cdots + G_n s^n$.
   where
   $G_0 = h_0^2$
   $G_1 = h_1^2 + 2h_2 h_0$
   $\vdots$
   $G_i = h_i^2 + 2(h_{2i}h_0 + \sum_{j=2}^{i} h_{j-1}h_{2i-j+1})$
   $\vdots$
   $G_k = G_i|_{i=k} + 1$
   $\vdots$
   $G_n = h_n^2$
2. Find the roots of $g(s)g(-s)$.
3. Choosing the L.H.P. roots of $g(s)g(-s)$, form the polynomial* $g(s) = g_0 + g_1 s + \cdots + g_n s^n$.

* It should be noted that the roots of $g(s)g(-s)$ have the mirror symmetry, in $s = \sigma + j\omega$ complex plane with respect to the $j\omega$, unless there are roots at $\omega = 0$ whenever $h_0 = 0$ for $k > 0$. Therefore, for the $k > 0$ case, h_0 must not be zero in order to guarantee the Hurwitzness of $g(s)$.

4. Construct the real normalized scattering parameters from $h(s)$ and $g(s)$:

$$e_{11}(s) = \frac{h(s)}{g(s)}, \qquad e_{21} = e_{12}(s) = \mp\frac{s^k}{g(s)}$$

$$e_{22}(s) = -(-1)^k \frac{h(-s)}{g(s)}.$$

5. Knowing $E = \{e_{ij}\}$, $(i, j = 1, 2)$, compute the transducer power gain $T(\omega)$:

$$T(\omega) = T_g \frac{|e_{21}|^2 |l_{21}|^2}{|1 - e_{11}S_G|^2 |1 - \hat{e}_{22}S_L|^2} \qquad [3]$$

where

$$T_g = 1 - |S_G|^2,$$

$$|e_{21}|^2 = 1 - |S_L|^2,$$

$$\hat{e}_{22} = e_{22} + \frac{e_{21}{}^2 S_G}{1 - e_{11}S_G}$$

Now, the coefficients h_i are chosen as the unknown and the above algorithm is combined with a nonlinear optimization routine to determine the unknown coefficients h_i so that the $T(\omega)$ is optimized. Once the final form of $e_{11}(s)$ is computed, corresponding input impedance $Z = (1 + e_{11})/(1 - e_{11})$ is generated and it is realized by the Darlington method as a lossless two port with resistive termination. Thus, the circuit topology of the matching network is obtained as a result of the design procedure.

3. Numerical Work

Based upon the approach described above, a computer program has been developed to compute the unknown coefficients h_i of the numerator polynomial $h(s)$ of the input reflection coefficient $e_{11}(s) = h(s)/g(s)$. In the optimization scheme, an ideal form of the transducer power gain may be approximated in the least squares sense. In that case, the objective function δ may be defined as

$$\delta = \sum_{j=1}^{m} [T(\omega_j, h_i) - \hat{T}]^2; \qquad i = 1, 2, .. n, \qquad [4]$$

where m is the number of sampling frequencies in the passband, $\hat{T}$ may be the desired maximum flat gain level to be approximated, and $T(\omega_j, h_i)$ is the actual transducer power gain generated in terms of the unknown polynomial $h(s)$ (as in the algorithm given in the previous

section). Any iterative, nonlinear optimization algorithm can be used to minimize δ. In this work, it was found that modified Levenberg-Marquand technique provides satisfactory results.[6]

At each iteration, coefficients $(h_{io} + \Delta h_i)$ are corrected to minimize the objective function δ where h_{io} is the initial guess to h_i and Δh_i is the increment obtained during the optimization process. Computations may be terminated when δ becomes sufficiently small.

It is important to note that there is no restriction other than that the unknown coefficients (h_i, $i = 0, . , n$) are real. Realizability is simply achieved by choosing the denominator $g(s)$ as a Hurwitz polynomial. Therefore, any unconstrained, straightforward optimization routine can be used to determine the unknown coefficients h_i.

As is usually the case, an intelligent initial guess is important in efficiently running the program. In the present problem, the following initialization proved highly successful. We presume that the problem under consideration is a single-matching problem, i.e., source or load network is resistive. Then, employing the real frequency technique for single-matching problems,[1] input impedance Z (or equivalently input admittance Y) of the lossless matching network with resistive termination is computed, and corresponding reflection coefficient $e_{11} = h(s)/g(s) = (Z - 1)/(Z + 1)$ is generated.

An ad hoc direct choice for coefficients h_i (e.g. $h_i = 1$ or -1) is, of course, not precluded in simpler problems.

4. Examples

In this section, examples are presented to show the application of the simplified real frequency technique. In the literature, it has usually been assumed that the "best" analytic theory has to offer, even in simple cases, is the Chebyshev response.[4] The first example given shows, however, that if the analytic theory is capable of solving the problem, the solution obtained via the simplified real frequency technique yields superior gain response, which agrees with the results given in Ref. [4] for single-matching problems. In the second example, it would hardly be possible to solve the double-matching problem via analytic theory, whereas we had no difficulty in implementing the simplified real frequency technique. Furthermore, the choice of circuit topology, which here is obtained as a result of the design procedure, may not be straightforward enough to initiate a commercially-available CAD program such as COSMIC or COMPACT to optimize the element values.

Last, an example is given of the use of the new method in the design of an FET amplifier.

Example 1: It is desired to design a matching network, shown in Fig. 2, to optimize the transducer power gain.

Inputs:

Generator (S_G) and Load (S_L) are as shown in Fig. 2.

$n = 3$; degree of the numerator polynomial $h(s)$ of $e_{11}(s) = h(s)/g(s)$, which determines the complexity of the matching network: three-element ladder.

$k = 0$; degree of the numerator of $e_{21}(s)$, contributes to the complexity of the matching network: low pass ladder.

$\hat{T} = 0.95$; estimated flat gain level (see Eq. [4])

Initial guess:

$$h_0 = 1, h_1 = -1, h_2 = 1, h_3 = -1.$$

Passband: $0 \leq \omega \leq 1$, where ω is the normalized frequency.

$m = 10$; number of evenly distributed sampling frequencies in the passband, chosen for the least-square optimization (See Eq. [4]).

Result of Optimization:

$$e_{11}(s) = \frac{0.1395 - 0.3225S + 0.1596S^2 - 2.093S^3}{1.001 + 2.476S + 3.001S^2 + 2.093S^3}.$$

Performance of the matched structure:

$$T(\omega) \approx 0.96 \pm 0.0215; \qquad 0 \leq \omega \leq 1.$$

Synthesis of the matching network:

Input impedance $Z(s) = [1 + e_{11}(s)]/[1 - e_{11}(s)]$ is synthesized as a lossless ladder with resistive termination by continuous fraction expansion. Removal of this 1-ohm resistance yields the desired matching network

Discussion: The same problem was also solved analytically by Fielder[7] employing Chebyshev transfer function. The gain-bandwidth constraints could only be satisfied if at least one type-C section was used in the matching network which reduces the gain. With three reactive elements in the matching network (counting also the coupled coils of

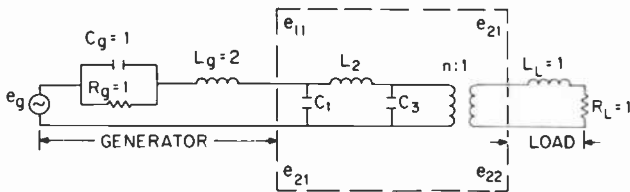

Fig. 2—Solution to example 1: $C_1 = 1.322$, $L_2 = 2.475$, $C_3 = 1.113$, and $n = 1.15$.

type-C section) the performance of the Fielder's solution is given as:

$$T(\omega) \cong 0.92 \pm 0.076.$$

Clearly, with the same number of elements in the matching network, the simplified real frequency technique offers a better performance, yet the circuit topology is simpler (no coupled coils in the matching network).

Example 2: Referring to Fig. 3, we wish to construct a matching network to optimize the gain of the system.

Inputs:

Generator (S_G) and Load (S_L) are as shown in Fig. 3.

$n = 4$; four-element ladder.

$k = 2$; two high pass elements are permitted in the matching network (series capacitors, shunt inductors).

$\hat{T} = 0.765$; estimated flat gain level, approximated in the least-square sense.

Initial guess:

$$h_0 = 1,\ h_1 = -1,\ h_2 = 1,\ h_3 = -1,\ h_4 = -1.$$

Passband: $0.3 \le \omega \le 1$; ω is the normalized frequency.

$m = 20$; number of evenly-distributed frequencies.

Result of optimization:

$$e_{11}(s) = \frac{0.254 - 0.365S + 1.356S^2 - 1.398S^3 - 0.79S^4}{0.254 + 0.793S + 2.3345S^2 + 0.279S^3 + 0.79S^4}.$$

Performance of the matched structure:

$$T(\omega) = 0.765 \pm 0.02$$

Synthesis of the matching network:

$$Z(s) = \frac{1 + e_{11}(s)}{1 - e_{11}(s)} \text{ is synthesized as a ladder network.}$$

The final circuit is shown in Fig. 3.

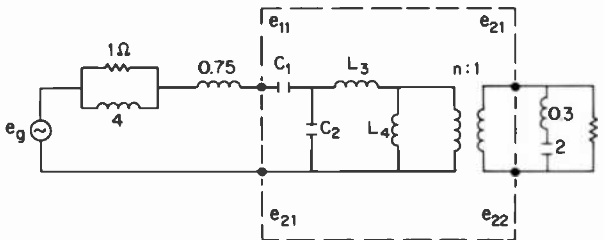

Fig. 3—Solution to example 2: $C = 2.28$, $C_2 = 2.26$, $L_3 = 0.717$, $L_4 = 1.024$, and $n = 1.024$.

Discussion: This example is quite an unusual one. The generator and load networks are chosen such that they include all the possible conventional real frequency transmission zeros, namely at dc, infinity, and at a finite frequency $\omega_0 = 1.29$ (Fig. 3). In this case, the analytic theory is not applicable because of the difficulty in choosing a usable transfer function. Furthermore, if one employs a commercially-available CAD program, such as COSMIC,[8] a circuit topology for the matching network must be chosen. But, for this specific problem, the choice of topology is not straightforward. Even if the circuit topology is chosen, it would not be clear how to initialize the element values of the chosen topology for a nonlinear optimization program. We had no difficulty in computing $e_{11}(s) = h/g$, which also yielded the circuit topology. In this example, we also tried to improve the performance by optimizing the element values obtained by simplified technique using COSMIC. However, there was no significant improvement observed in the gain response.

Example 3: In this example, the design of a single-stage FET amplifier for 50-Ω terminations using the FET MGF-2124F by Mitsubishi over the passband 10.9 GHz $\leq f \leq$ 11.7 GHz is considered.

The complete design may be performed in two steps. As a first step, the front-end matching network is designed when the output of the FET is terminated in 50 ohms (Fig. 4a). In this case, the transducer power gain $T_1(\omega)$ is given as

$$T_1(\omega) = \frac{|e_{21_F}|^2 |f_{21}|^2}{|1 - e_{22_F} f_{11}|^2},$$

where $\{f_{ij}\}$ and $\{e_{ij_F}\}(i, j = 1, 2)$ are the 50-ohm, normalized scattering

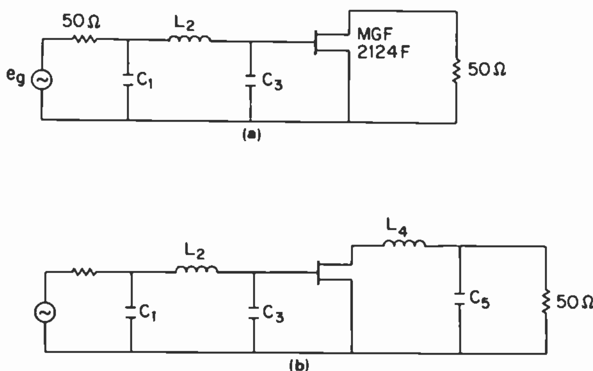

Fig. 4—Design of the FET amplifier for example 3: (a) $C = 0.256$ pF, $L_2 = 0.658$ nH, and $C_3 = 0.838$ pF and (b) $L_4 = 1.97$ nH and $C_5 = 0.565$ pF.

parameters of the FET and the front-end matching network, respectively. In the second step, the 50-ohm termination is removed and the back-end matching network is designed (Fig. 4b). Here, the transducer power gain T_2 of the overall amplifier is given as follows:

$$T_2(\omega) = T_1(\omega)\frac{|e_{21_B}|^2}{|1 - e_{11_B}S_G|^2},$$

where

$$S_G = f_{22} + \frac{f_{12}f_{21}}{1 - f_{11}e_{22_F}}e_{22_F},$$

$T_1(\omega)$ is the transducer power gain (computed in the previous step) and $\{e_{ij_B}\}$, $i, j = 1, 2$ are the 50-ohm normalized scattering parameters of the back-end matching network.

At step i, the transducer gains $T_i(\omega)$, $i = 1, 2$ may be optimized in the least-squares sense as in Sec. 3. The objective function δ_i is defined as

$$\delta_i = \sum_{j=1}^{m} (T_i(\omega) - \hat{T}_i)^2, \qquad i = 1, 2,$$

where $\hat{T}_i$ is the desired flat gain level to be approximated. At the first step, $\hat{T}_i$ may be estimated assuming the amplifier is perfectly matched at the input:

$$\hat{T}_1 \approx \text{minimum}\left\{\frac{|f_{21}|^2}{1 - |f_{11}|^2}\right\}$$

over the passband. Similarly, at the second step $\hat{T}_2$ may be estimated by assuming perfect match at the output:

$$\hat{T}_2 \approx \text{minimum}\left\{T_1\frac{1}{1 - |f_{22}|^2}\right\}$$

over the passband.

Following the above steps, a computer program has been developed to approximate the desired gain levels $\hat{T}_1$ and $\hat{T}_2$ sequentially, yielding the realizable reflection coefficients $e_{11_F}(s)$ and $e_{11_B}(s)$. The result of the computations is summarized as follows:

Step 1: Compute the front-end matching network ($e_{11_F}(s)$).

Inputs:

$\{f_{ij}\}$, $i, j = 1, 2$; measured scattering parameters of the FET-MGF-2124F (not given here).

$n = 3$; three-element ladder.

$k = 0$; low-pass design.

$h_0 = 0$; fixed design with no transformer.

Initial guess:

$$h_1 = -1, h_2 = 1, h_3 = -1$$

Passband: 10.9 GHz $\leq f \leq$ 11.7 GHz
m = 10; number of evenly-distributed sampling frequencies.
Result of optimization:

$$e_{11_F}(s) = \frac{0 - 1.527S + 1.036S^2 - 1.403S^3}{1 + 2.495S + 1/947S^2 + 1/4\text{-}3S^3}.$$

Performance of this step:

$$T_1(\omega) \approx 2.81 \pm 0.48 \text{ dB},$$

$$Z_F(s) = [1 + e_{11_F}(s)]/[1 - e_{11_F}(s)].$$

Notice that since $h_0 = 0$ is fixed, there is no transformer in the matching network (Fig. 4a).
Step 2:
Compute the back-end matching network ($e_{11_B}(s)$).
Inputs:
$\{f_{ij}\}$, i, j = 1, 2; given as in Step 1.
n = 2; two-element ladder,
k = 0; low-pass design.
h_0 = 0; fixed design with no transformer,
$\hat{T}_2$ = 5.6 dB, estimated flat gain level.
Initial guess:

$$h_1 = -1, h_2 = 1.$$

Passband: 10.9 GHz $\leq f \leq$ 11.7 GHz
m = 10
Result of the optimization:

$$e_{11_B}(s) = \frac{0 - 0.894S + 0.3S^2}{1 + 1.183S + 0.3S^2}.$$

Performance of the amplifier:

$$T_2(\omega) \cong 5.33 \pm 0.61 \text{ dB}.$$

$Z_B(s) = [1 + e_{11_B}(s)]/[1 - e_{11_B}(s)]$ is synthesized (Fig. 4b) as a low-pass ladder.

Thus the circuit topology for the matching networks is resolved. The amplifier was actually built at RCA. Lumped capacitors were made on rutile substrates and inductors were realized by bond wires. The schematic and the picture of the amplifier are shown in Figs. 5 and 6, respectively. The computed and measured performance of the amplifiers is shown in Fig. 7. This example clearly shows that the

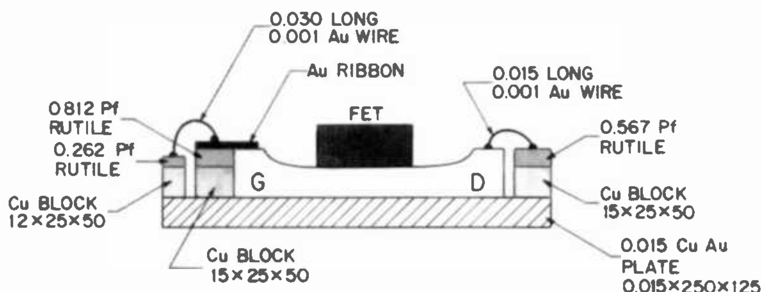

Fig. 5—Schematic of the amplifier designed for example 3.

matching networks obtained by the simplified real frequency technique are realizable.

In the course of the above design process, the gain taper of the FET is compensated at the front-end matching network. The back-end matching network provides further improvement in the overall transducer power gain. It should be noted that the nonunilateral behavior of the FET is taken into account.

The design technique that has been discussed is applicable to

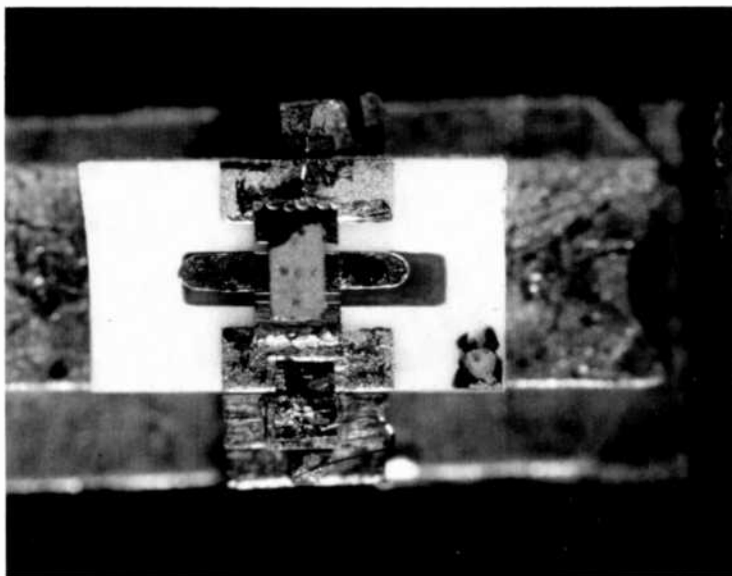

Fig. 6—Photograph of FET amplifier designed for example 3.

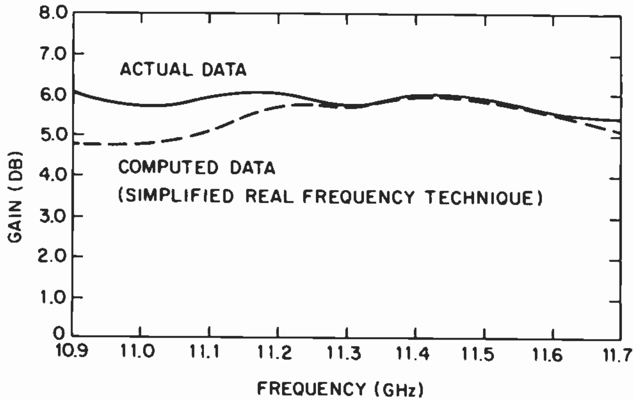

Fig. 7—Performance of amplifier designed for example 3.

optimizing a variety of objective functions, as in Ref. [2]. Thus, it can be used, for example, for maximizing the minimum passband gain or for minimizing maximum noise figure or high-gain flat-noise-figure design.

5. Conclusion

This paper presents a new CAD technique for designing matching networks. The procedure requires no decision to be made in advance as to algebraic form of transfer functions or circuit topology. Furthermore, matching networks are generally simpler with superior gain properties as compared to structures obtained by the analytic procedure. The technique may be applied to various kinds of problems. Examples have been presented to exhibit the application of the technique. Finally, an FET amplifier has been designed and built to emphasize the practical use of the technique.

Acknowledgment

Gratitude is extended to Professor H. J. Carlin who has been a source of encouragement and insight to the author during his doctoral and postdoctoral research at Cornell University. Many thanks are extended to Dr. H. Huang who supported the development of the software at Microwave Technology Center, RCA, Princeton. The author also thanks E. Mykietyn and P. Czajkowski for their help in building the actual amplifier.

References:

[1] H. J. Carlin, "A New Approach to Gain-Bandwidth Problems," *IEEE Trans. CAS*, **23**, p.170, April 1977.

[2] H. J. Carlin, and J. J. Komiak, "A New Method of Broadband Equalization Applied to Microwave Amplifiers," *IEEE Trans. MTT*, **27**, No. 2, p. 93, Feb. 1979.
[3] B. S. Yarman, *Broadband Matching a Complex Generator to a Complex Load*, Ph.D. Thesis, Cornell University, Ithaca, NY, Jan. 1982.
[4] H. J. Carlin, and P. Amstutz, "On Optimum Broadband Matching," *IEEE Trans. CAS*, **28**, No. 5, p. 401, May 1981.
[5] V. Belevitch, "Elementary Application of the Scattering Formalism to Network Design," *IRE Trans. Circuit Theory*, **CT-3**, No. 2, June 1956.
[6] K. M. Brown and J. E. Dennis, "Derivative Free Analogues of the Levenberg-Marquardt and Gauss Algorithms for Nonlinear Least Square Approximations," *Numerische Mathematik*, **18**, p. 289.
[7] D. C. Fielder, "Broadband Matching between Load and Source Systems," *IRE Trans. Circuit Theory*, **CT-8**, p. 138, June 1961.
[8] B. S. Perlman, private communication.

The Photoresponse of Thin-Film PtSi Schottky Barrier Detector with Optical Cavity

Hammam Elabd and Walter F. Kosonocky
RCA Laboratories, Princeton, NJ 08540

Abstract—Recently, high performance Schottky-barrier IR-CCD imagers have been developed utilizing thin-film Schottky barrier detectors (SBDs) with an optical cavity. The external quantum efficiency achieved for these PtSi-SBDs without AR coating is 2% at 4 μm. AR-coating improves the sensitivity by more than 30%. A model for the photoyield of a thin SBD is described. The model is in good agreement with experimental data and predicts that further improvement in photoyield can be expected by optimization of the detector structure to increase the optical absorptance and/or to enhance the anisotropy in the direction of hot-hole motion.

Introduction

The PtSi and Pd_2Si Schottky barrier IR-imaging technologies[1,2] are based on relatively sensitive thin-film Shottky barrier detectors (SBDs) formed on silicon. The thin-film PtSi-SBDs constructed with optical cavity exhibit a quantum efficiency (Q.E.) of a few percent in the 3 to 5 μm band. This quantum efficiency is sufficient in most staring infrared focal-plane-array (IR-FPAs) applications, where the upper limit for the useful quantum efficiency range is set by the limited charge-handling capacity of the CCD and the high 300-K background radiation.

Detector Structure and Responsivity Measurement

The construction of a thin-film SBD with optical cavity is shown in Fig. 1. The PtSi film thickness is 20–100 Å. A 2000–10000 Å dielectric layer is deposited on the silicide film followed by an aluminum mirror. The back side of the silicon substrate is AR coated. The structure is back illuminated and is designed to induce (1) an enhanced optical absorptance as a result of a multiple pass of the light in the film and (2) an increase in the injection (emission) efficiency of hot holes into the substrate. The increase in the injection efficiency is the result of hot-hole scattering (reflection) at the silicide-dielectric interface and will be referred to as the internal quantum-efficiency gain.

Measured responsivity of a thin PtSi-SBD with optical cavity is shown on Fig. 2. This sample was not AR-coated. AR-coated detectors show about 30% higher responsivity at the center of the band. This spectral responsivity data corresponds to a quantum efficiency of 2% and 10% at 4.0 μm and 2.45 μm, respectively. As is described later, the experimental points in Fig. 2 are compared with the theoretical curves for responsivity, $R = Y/h\nu$ where $h\nu$ is the photon energy and Y is the external photoyield.

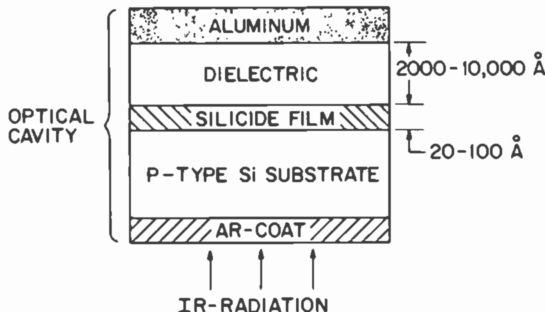

Fig. 1—Cross-sectional view of thin silicide SBD with optical cavity.

Photoyield Model

A simplified energy band diagram of the PtSi p-type-silicon Schottky-barrier detector is shown on Fig. 3. The absorption of IR-radiation in the PtSi film excites valance electrons in the metal silicide to states above the fermi level, leaving behind holes. The hot holes are those that have energies higher than the barrier height, ψ_{ms}. The cold holes are those that have energies below ψ_{ms}. For typical infrared light frequencies the photon energy, $h\nu$, is much smaller than the fermi energy, $h\nu \ll E_f$, and it is reasonable to assume that the density of

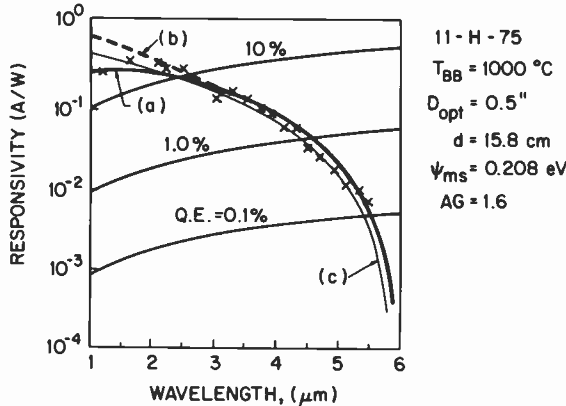

Fig. 2—Measured values of responsivity and quantum efficiency (Q.E.) of thin-PtSi SBD with optical cavity (but without AR coating) compared with computed curves: (a) for Eq. [2] with ψ_{ms} 0.208 eV and AG = 1.6, and (b) and (c) for Eq. [3] with ψ_{ms} = 0.208 eV and C_1 of 0.95 eV^{-1} and 0.54 eV^{-1}, respectively.

states, N, and the probability of excitation are constants over the excitation range.[3]

The internal quantum efficiency, Y_i, can be described as the ratio of the number of states from which hole emission across the barrier may occur to the total number of possible excitated states.

$$Y_i = \frac{\int_{\psi_{ms}}^{h\nu} NP(E)\, dE}{Nh\nu} = \frac{G}{2}(1 - \cos\theta_0)^2 \qquad [1]$$

where $P(E)$ is the escape (emission) probability, which is defined by the momentum criterion at the interface; θ_0 is the critical escape angle, which is defined as $\cos\theta_0 = (\psi_{ms}/h\nu)^{1/2}$; and G is the internal quantum-efficiency gain factor. G represents the improvement in internal quantum efficiency due to the hot holes that are reflected (scattered) at the PtSi-dielectric interface.[3-7]

The external quantum efficiency (photoyield) may be expressed as

$$Y = AY_i = \frac{AG}{2}(1 - \cos\theta_0)^2 \qquad [2]$$

where A is the optical absorbtance in the spectral window of the detector, defined as the ratio of the IR radiation power absorbed in the silicide film to the incident IR radiation power. For photon energies close to the barrier height, i.e., $h\nu < 2\psi_{ms}$, Eq. [2] can be approximated by the commonly used Fowler equation for SBD photoyield,[8]

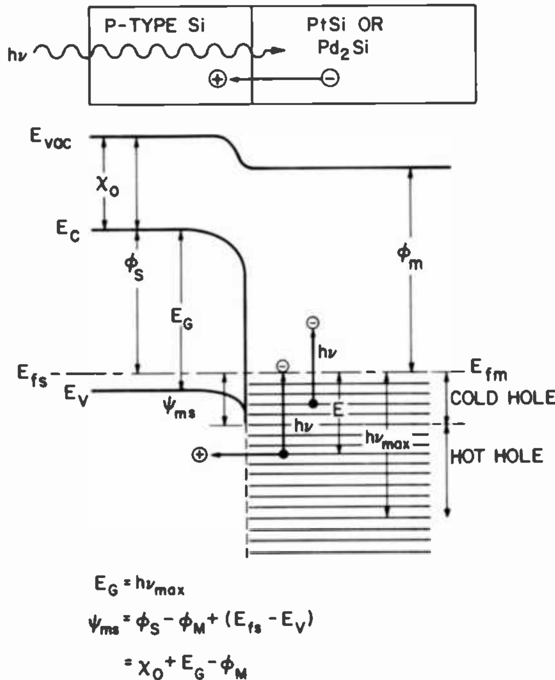

Fig. 3—Energy diagram illustrating the operation of PtSi or Pd_2Si SBD on p-type Si substrate.

$$Y = \frac{AG}{8\psi_{ms}} \frac{(h\nu - \psi_{ms})^2}{h\nu} = C_1 \frac{(h\nu - \psi_{ms})^2}{h\nu}. \quad [3]$$

According to Eq. [3], the quantum efficiency coefficient, C_1, is

$$C_1 = \frac{AG}{8\psi_{ms}}. \quad [4]$$

Eq. [4] can be simplified to

$$C_1 = \frac{A}{8\psi_{ms}} \frac{sL}{t}, \quad [5]$$

where L is the mean free path of hot holes projected on the direction normal to the surface of the silicide, t is the thickness of the silicide layer, and s is a constant for each $h\nu$.[8]

Discussion

The responsivity data of Fig. 2 is fitted to the responsivity as shown by curve (a) calculated from Eq. [2] for $AG = 1.6$ and $\psi_{ms} = 0.208$ eV. Eq. [2] predicts the saturation of SBD responsivity in the SWIR band

as is observed experimentally. This should be compared with curves (b) and (c) for the commonly used Fowler photoyield expression following Eq. [3]. It should be noted that according to Eq. [4], the quantum efficiency coefficient C_1 should be 0.95 eV^{-1} if AG is a constant and equals 1.6 across the band (see curve (b)). However, a least squares fit to the data of Fig. 2 between 3.0 and 6.0 μm yields C_1 of 0.54 eV^{-1} (see curve (c)). The difference between $C_1 = 0.54$ eV^{-1} and $C_1 = 0.95$ eV^{-1} is due to the inaccuracy of Eq. [4] below 4.0 μm and AG variations across the band.

To illustrate the possible optimization of the SBD photoyield, Fig. 4 shows the curve of absorptance A of PtSi, the curve of the internal quantum efficiency gain G, and the curve of the product AG as a function of thickness of the PtSi layer normalized to the absorption length and L from Eq. [5]. The curve for the absorptance A, computed using Fresnel equations for the case of a PtSi film on a silicon substrate, is compared here with measured experimental points. It should be noted that for a thick PtSi film, the value of A approaches 5.0%. The computed quantum efficiency gain G, curve (b) in Fig. 4, is compared to two experimental points (solid circles).[8] These points are estimated

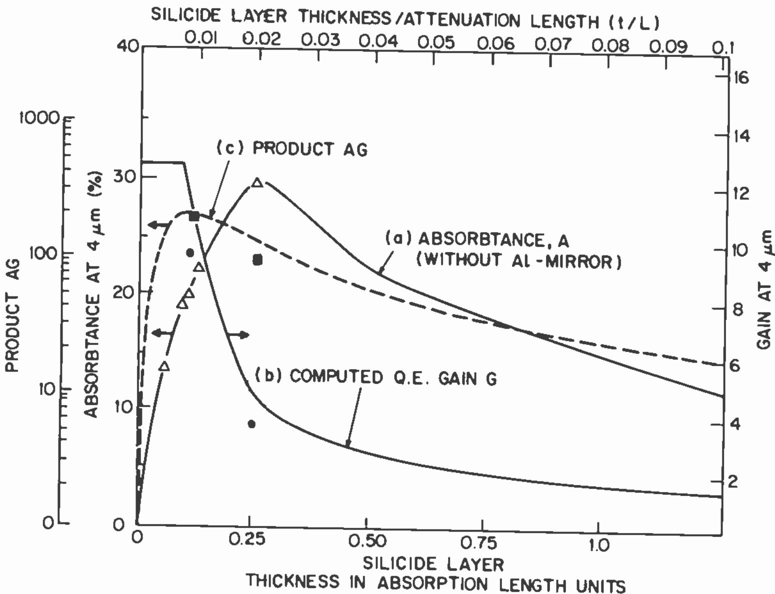

Fig. 4—Calculated and measured absorptance A for PtSi SBD without a reflector showing computed quantum efficiency gain factor G, and two experimental data points (solid circles). Also shown are computed AG product and two experimental points (solid squares) as a function of thickness of PtSi.

from Eq. [3] for measured values of photoyield (Q.E.) at a wavelength of 4.0 μm and computed values of absorptance A for two different thin-PtSi SBDs with optical cavity. The absorptance of the two SBDs with optical cavity is only somewhat higher in this case than the computed absorptance of Fig. 4.[1,8] Inspection of Fig. 4 shows the peak of the optical absorptance for the PtSi film occurs at a thickness corresponding to one quarter of an absorption length. The optimal thickness of the PtSi layer is around one eighth of an absorption length, as shown by the curve of the product AG.

According to Eq. [3], the external quantum efficiency at 4.0 μm for thick PtSi is 0.06% based on $G = 1$, $A = 0.05$, and $\psi_{ms} = 0.22$ eV.[1,8] It follows that the Q.E. of the SBD in Fig. 2 is higher than that of a thick PtSi SBD by a factor larger than 32. A factor of 3.46 is attributed to the improvement in the optical absorptance and a factor of 9.25 is attributed to the gain factor G, i.e., the improvement due to the hot-hole reflections at the silicide-dielectric interface. Further improvement in quantum efficiency of thin-PtSi SBDs can be expected by optimizing the absorptance of the detector structure shown in Fig. 1 by introduction of AR coating and by using an optimum thickness of the dielectric layer between the PtSi film and the aluminum mirror.

References:

[1] W. F. Kosonocky, H. Elabd, H. G. Erhardt, F. V. Shallcross, G. M. Meray, T. S. Villani, J. V. Groppe, R. Miller, V. L. Frantz, M. J. Cantella, J. Klein, and N. Roberts, "Design and Performance of 64X128-Element PtSi Schottky-Barrier IR-CCD Focal Plane Array," SPIE's Tech. Symp. East'82, Arlington, VA, May 3-7, 1982.

[2] H. Elabd, T. S. Villani, and J. R. Tower, "High Density Schottky-Barrier IRCCD Sensors for SWIR Applications at Intermediate Temperature," SPIE's Tech. Symp. East'82, Arlington, VA, May 3-7, 1982.

[3] R. J. Archer and J. Cohen, U.S. Patent 3,757,123.

[4] R. W. Taylor, L. H. Skolnik, B. R. Capone, W. Ewing, F. D. Shepherd, S. A. Roosild, B. Cochrun, M. Cantella, J. Klein, and W. F. Kosonocky, "Improved Platinum Silicide IRCCD Focal Plane," PSIE's Tech. Symp. on Advances in Focal Plane Technology, Los Angeles, CA, Feb. 4-5, 1980.

[5] W. F. Kosonocky, H. G. Erhardt, G. M. Meray, F. V. Shallcross, H. A. Elabd, M. J. Cantella, J. Klein, L. H. Skolnik, B. R. Capone, R. W. Taylor, W. Ewing, F. D. Shepherd, and S. Roosild, "Advances in Platinum-Silicide Schottky-Barrier IR-CCD Image Sensors," SPIE Vol. 225, p. 69, *IR-Image Sensor Tech.* (1980).

[6] M. Kimata, M. Denda, T. Fukumoto, N. Tsubouchi, S. Uematsu, H. Shibata, T. Higuchi, T. Saheki, R. Tsunoda, and T. Kanno, "Platinum Silicide Schottky-Barrier IR-CCD Image Sensors," *J. Proc. 13th Conf. on Solid State Devices*, p. 231, Tokyo, 1981.

[7] W. F. Kosonocky, H. Elabd, H. G. Erhardt, F. V. Shallcross, T. Villani, G. Meray, M. J. Cantella, J. Klein, and N. Roberts, "64 × 128-Element High-Performance PtSi IR-CCD Image Sensor," 1981 IEDM, Washington, DC, Dec. 7, 1981.

[8] H. Elabd and W. F. Kosonocky, to be published.

Theory of Large-Angle Deflection of Electrons in the Magnetic Field Inside a Television Tube

Basab B. Dasgupta
RCA Consumer Electronics, Indianapolis, Indiana 46201

Abstract—In current wide-angle television tubes the electron beams have to be deflected by rather large angles in order for them to reach points at or near the screen boundary. A new perturbative technique is developed for determining the trajectories of electrons inside the TV tube for such large-angle deflections. The method is based on solving the Euler-Lagrange equations in cylindrical coordinates. This technique is applied to calculate the convergence errors between the three primary beams at a corner point on the screen. The results are analyzed in terms of the contributions from the various harmonic components of the field.

1. Introduction

Present-day color TVs almost exclusively use in-line guns and yokes with large corner-to-corner deflection angles (90°–110°). The third-order aberration theory[1] is inadequate to explain or predict the performance of such yokes, especially the convergence errors between the electron beams when they strike points at or near the screen boundary. Recently, very sophisticated computer programs have been developed[2,3] that numerically calculate the magnetic field and hence the electron trajectories inside the TV tube, but even the predictions of these programs disagree drastically with the experimentally measured values for the microconvergence errors at the corners of the TV screen.[2]

The present paper provides a simple analytical approach for treating

very large angles of deflection of the electrons. Specifically, we develop a theory for calculating the trajectories of electrons that are deflected to a corner point and, hence, the misconvergence at the corner. The same idea can also be applied to calculate the misconvergence at the 3 o'clock or 12 o'clock positions on the screen. It can be considered as a perturbation theory where the "unperturbed" trajectory is taken to be a known curve. Taking this curve as the "zeroth order" path the first-order correction to the path is obtained by solving the Euler-Lagrange equations in cylindrical coordinates.

The remainder of the paper is organized as follows. In Sec. 2 we derive the Euler-Lagrange equations in cylindrical coordinates. The "first-order" solutions to these equations are obtained in Sec. 3 in terms of integrals of the various field components. Sec. 4 is devoted to a qualitative physical interpretation of the results. We conclude in Sec. 5 by summarizing our findings and discussing the merits of the analysis.

2. Mathematical Formulation

The key to treating large-angle deflections is the harmonic analysis where the current distributions in the horizontal and vertical coils are expanded in Fourier series in the polar angle about the yoke axis. It is appropriate, therefore, to formulate the whole problem in cylindrical (ρ, θ, z) coordinates from the outset, z being the yoke axis. In this section we derive the Euler-Lagrange equations for the motion of electrons.

As usual, we start from the Fermat's principle[4] which states that the following integral is a minimum for the actual path of the electrons between two points P_1 and P_2:

$$J \equiv \int_{P_1}^{P_2} n \, ds, \qquad [1]$$

where ds is an element of path length given by

$$ds = dz(1 + \rho'^2 + \rho^2\theta'^2)^{1/2} \qquad [2]$$

and n is the effective refractive index given by

$$n = \sqrt{V} - \eta(\mathbf{A}\cdot\mathbf{S}). \qquad [3]$$

Here $\eta = (e/2m)^{1/2}$(e-charge, m-mass of electron)
V is the electrostatic potential measured from the cathode
$\mathbf{A}$ is the magnetic vector potential
$\mathbf{S}$ is a unit vector in direction of the path.

The primes in Eq. [2] and in our subsequent discussion indicate derivatives with respect to z. The integral J can be rewritten in terms

of the independent variable z as

$$J = \sqrt{V} \int_{z_0}^{z_s} G(z, \rho, \rho', \theta, \theta')\, dz, \tag{4}$$

where

$$G = (1 + \rho'^2 + \rho^2\theta'^2)^{1/2} - k(A_\rho \rho' + A_\theta \rho \theta' + A_z) \tag{5}$$

$$k = \eta/\sqrt{V} \tag{6}$$

and z_0, z_s are, respectively, the gun and screen locations along the z-axis. The Euler-Lagrange equations can now be written as

$$\frac{\partial G}{\partial \rho} - \frac{d}{dz}\left(\frac{\partial G}{\partial \rho'}\right) = 0, \tag{7}$$

$$\frac{\partial G}{\partial \theta} - \frac{d}{dz}\left(\frac{\partial G}{\partial \theta'}\right) = 0. \tag{8}$$

Taking the indicated derivatives and using the fact that the magnetic field **B** is related to **A** by the relation

$$\mathbf{B} = \nabla \times \mathbf{A}, \tag{9}$$

Eqs. [7] and [8] can be easily recast into the following forms:

$$\frac{d}{dz}\left[\frac{\rho'}{(1 + \rho'^2 + \rho^2\theta'^2)^{1/2}}\right] = -kB_z\rho\theta' + kB_\theta + \frac{\rho\theta'^2}{(1 + \rho'^2 + \rho^2\theta'^2)^{1/2}} \tag{10}$$

and

$$\frac{d}{dz}\left[\frac{\rho^2\theta'}{(1 + \rho'^2 + \rho^2\theta'^2)^{1/2}}\right] = kB_z\rho\rho' - k\rho B_\rho. \tag{11}$$

3. First-Order Solution at Corner

Let θ_s be the polar angle of the corner point which lies in the first quadrant of the TV screen. For a screen with a 3:4 aspect ratio, θ_s is approximately 37°. As a zeroth order solution to Eqs. [10] and [11] we can take the beam-path as computed by the first-order aberration theory which will be written as

$$\rho(z) = \rho_0(z) \tag{12}$$

$$\theta(z) = \theta_0(z). \tag{13}$$

These functions can be calculated either analytically by taking some model expression for the first harmonic field or numerically by the

methods described in Refs. [2] and [3]. In any event these are assumed to be accurately known functions. The function $\theta_0(z)$ is almost a constant in the first-order aberration theory over the region where the magnetic field is significant, as shown in Fig. 1 for the blue beam. θ_0 is close but not equal to θ_s.

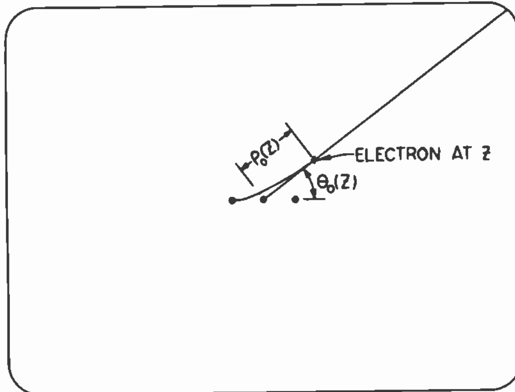

Fig. 1—The projection of the "unperturbed" path of electrons on the TV screen for the "blue" beam.

We can now solve Eqs. [10] and [11] by perturbative approximations. In Eqs. [10] and [11] we put

$$\rho(z) = \rho_0(z) + \rho_1(z) \qquad [14]$$

$$\theta(z) = \theta_0(z) + \theta_1(z), \qquad [15]$$

where ρ_1 and θ_1 are assumed to be small quantities whose second and higher powers can be neglected. It is also convenient to write the potentials ϕ and ψ due to the horizontal and vertical coils, respectively, as

$$\phi(\rho, \theta, z) = \sum_{m=1,3,5\cdots} a_m(\rho, z)\sin m\theta \qquad [16]$$

$$\psi(\rho, \theta, z) = \sum_{m=1,3,5\cdots} b_m(\rho, z)\cos m\theta \qquad [17]$$

where $\mathbf{B} = -\mu_0\nabla(\phi + \psi)$. Eqs. [10] and [11] then reduce to

$$\frac{d}{dz}\left[\frac{\rho_1'(1 + \rho_0^2\theta_0'^2)}{(1 + \rho_0'^2 + \rho_0^2\theta_0'^2)^{3/2}}\right] = -\left(\frac{k\mu_0}{\rho_0}\right) \sum_{m=3,5\cdots} m[a_m(\rho_0, z)\cos m\theta_0 - b_m(\rho_0, z)\sin m\theta_0] \qquad [18]$$

and

$$\frac{d}{dz}\left[\frac{\rho_0{}^2\theta_1{}'}{(1+\rho_0{}'^2+\rho_0{}^2\theta_0{}'^2)^{1/2}}\right]=$$

$$-k\mu_0 \sum_{m=3,5\ldots}\left[\left(\frac{\partial a_m}{\partial z}\right)_{\rho=\rho_0}\rho_0\rho_0{}'\sin m\theta_0\right.$$

$$+\left(\frac{\partial b_m}{\partial z}\right)_{\rho=\rho_0}\rho_0\rho_0{}'\cos m\theta_0 \qquad [19]$$

$$-\left(\frac{\partial a_m}{\partial \rho}\right)_{\rho=\rho_0}\rho_0\sin m\theta_0$$

$$\left.-\left(\frac{\partial b_m}{\partial \rho}\right)_{\rho=\rho_0}\rho_0\cos m\theta_0\right].$$

Here μ_0 is the permeability of free space. Note that the summations over m in Eqs. [18] and [19] start with $m = 3$ because the $m = 1$ terms are cancelled by the unperturbed functions on the left-hand side of Eqs. [10] and [11].* The term $kB_z\rho_0\theta_0{}'$ on the right-hand side of Eq. [10] has been neglected because it is very small; it can easily be included if desired. Also note that the terms linear in ρ_1 on the right-hand sides of Eqs. [18] and [19] either cancel out or are small compared to the other terms.

We can write the formal solutions of Eqs. [18] and [19] as

$$\rho_1(z) = -k\mu_0\int_{z_0}^{z} dz'\,\frac{[1+\rho_0{}'(z')^2+\rho_0{}^2\theta_0{}'^2]^{3/2}}{1+\rho_0{}^2\theta_0{}'^2}\int_{z_0}^{z'} dz'' \qquad [20]$$

$$\times\sum_{m=3,5\ldots}\frac{m[a_m(\rho_0,z'')\cos m\theta_0 - b_m(\rho_0,z'')\sin m\theta_0]}{\rho_0(z'')}$$

* This statement is not quite correct because the first-order aberration theory is not synonymous with the first harmonic theory but involves additional assumptions about the smallness of deflection and its slope. Terms involving the first harmonic are, therefore, necessary on the right hand sides of Eqs. [18] and [19] to take this difference into account. We will, however, ignore these terms which are somewhat cumbersome to write because (a) one important effect of these terms is a nonlinearity of the scan that is eliminated by electronic means and (b) these terms do not change our qualitative conclusions. Inclusion of these additional terms if need arises is straightforward.

and

$$\theta_1(z) = -k\mu_0 \int_{z_0}^{z} dz' \frac{[1 + \rho_0'(z')^2 + \rho_0'\theta_0'^2]^{1/2}}{\rho_0(z')^2} \int_{z_0}^{z'} dz''$$

$$\times \sum_{m=3,5\cdots} \left[\rho_0(z'')\rho_0'(z'') \left\{ \left(\frac{\partial a_m}{\partial z''}\right)_{\rho=\rho_0(z'')} \sin m\theta_0 \right.\right.$$

$$\left. + \left(\frac{\partial b_m}{\partial z''}\right)_{\rho=\rho_0(z'')} \cos m\theta_0 \right\} - \rho_0(z'') \left\{ \left(\frac{\partial a_m}{\partial \rho}\right)_{\rho=\rho_0(z'')} \right.$$

$$\left.\left. \times \sin m\theta_0 + \left(\frac{\partial b_m}{\partial \rho}\right)_{\rho=\rho_0(z'')} \cos m\theta_0 \right\} \right]. \qquad [21]$$

Here the notation $a_m(\rho_0, z'')$ means $a_m\{\rho_0(z''), z''\}$ and a similar comment applies for $b_m(\rho_0, z'')$.

Although these expressions look rather involved, the main point to make here is that all the functions appearing on the right-hand sides of Eqs. [20] and [21] can be determined either analytically or numerically, and the integrations can be carried out using a computer. The conditions for perfect convergence without any coma or aberration error are given by

$$\rho_1{}^B(z_s) = \rho_1{}^G(z_s) = \rho_1{}^R(z_s) \qquad [22]$$

$$\theta_1{}^B(z_s) = \theta_1{}^G(z_s) = \theta_1{}^R(z_s) \qquad [23]$$

where the superscripts B, G, and R indicate the blue, green, and red beams. Since $\rho_1(z_s) = 0$ and $\theta_1(z_s) = 0$ correspond to a Gaussian convergence of all three beams on the screen, we will refer to ρ_1 and θ_1 as convergence error in the following discussion.

4. Physical Interpretation

In this section, we analyze the role of various harmonics in determining the convergence errors at the corners so that we know which harmonics to vary in order to attain the conditions expressed by Eqs. [22] and [23]. The first point to note is that although the third harmonic components a_3 and b_3 of the potential appear in Eqs. [20] and [21], their amounts are essentially determined by the convergence requirements along the major and minor axes, and hence they are not of much help in solving the problems of corner errors.

Next we observe that for $\theta_0 \approx \theta_s$, $\cos 5\theta_0 \approx -1$, $\sin 5\theta_0 \approx 0$, $\cos 7\theta_0 \approx 0$, and $\sin 7\theta_0 \approx -1$. So the expression for $\rho_1(z)$ contains a_5 and b_7, but negligible amounts of b_5 and a_7 and the converse is true for $\theta_1(z)$. This means that $\rho_1(z_s)$ can be controlled by the fifth harmonic of the

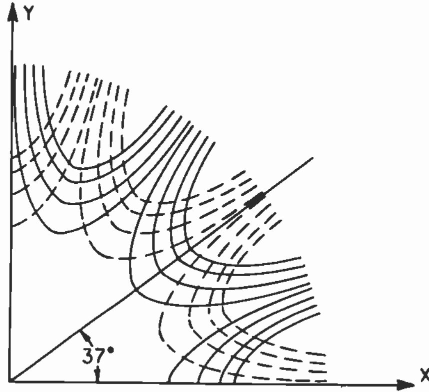

Fig. 2—Sketch of the field lines for the fifth harmonic component of the magnetic field. Solid lines correspond to the horizontal coil and dashed lines correspond to the vertical coil.

horizontal deflection field and/or the seventh harmonic of the vertical field whereas $\theta_1(z_s)$ can be controlled by the fifth harmonic of the vertical field and/or the seventh harmonic of the horizontal field.

This relationship between the convergence errors at the corner and the harmonics can be understood in a simple way from Figs. 2 and 3. Fig. 2 shows a sketch of the magnetic field lines for the fifth harmonic component of both the horizontal and vertical fields in the (ρ, θ) plane, and Fig. 3 is a similar sketch for the seventh harmonic. For an electron beam that is going to hit the corner, the electron motion can be resolved into two components—a motion along the z-axis and a motion at an angle of about 37° in the (ρ, θ) plane. Hence the magnetic field lines that point in the $\theta = 37°$ direction would have the largest effect on the movement of the beam in a perpendicular (i.e., tangential)

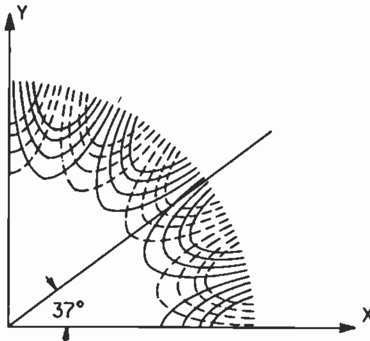

Fig. 3.—Sketch of the field lines for the seventh harmonic component of the magnetic field. Solid lines correspond to the horizontal coil and dashed lines correspond to the vertical coil.

direction and hence on controlling the error θ_1. By inspection of Figs. 2 and 3, we see that such field lines, are produced by the fifth harmonic of the vertical field (whose radial component is a maximum at $\theta = 36°$) and the seventh harmonic of the horizontal field (whose radial component is maximum at $\theta = 38.5°$). On the other hand, the radial error ρ_1 can be controlled by producing field lines in a tangential direction; again Figs. 2 and 3 show that such field lines correspond to the fifth harmonic of the horizontal and the seventh of the vertical field. In reality the situation is slightly more complicated because the magnetic field has a z-component. The above statement still holds, however, because the z-component of the field is almost zero for the fifth horizontal and seventh vertical harmonics and it is maximum (and hence aids the radial field in controlling θ_1) for the fifth vertical and seventh horizontal harmonics.

It is interesting to note that it is a coincidence that the angle 37° is approximately the zero of $\sin 5\theta$ and $\cos 7\theta$; this allowed us to separate the effects of the various harmonics. When the beam is going to an arbitrary point on the screen, this kind of diagramatic analysis is not very illuminating.

In principle, one can solve Eqs. [20] and [21] and determine what these four harmonic functions (a_5, b_5, a_7, b_7) should look like in order to satisfy four conditions (Eqs. [22] and [23]) needed for perfect convergence between red, green, and blue beams. Even if this cannot be done, we now at least know which harmonics to change to reduce a given amount of misconvergence at the corner. The present analysis also shows that the ninth or higher harmonic of the field is not really necessary. Some high harmonics in the vertical coil wire distribution might be necessary, however to make the coil physically windable.

5. Discussion and Conclusion

The main results of this paper can be summarized as follows:

(a) For a theoretical treatment it is more appropriate to resolve the corner misconvergence error into a radial part ρ_1 and a tangential part θ_1 instead of this conventional horizontal and vertical components.

(b) The fifth harmonic component of the horizontal deflecting field and the seventh harmonic component of the vertical deflecting field are the most effective in controlling the radial error ρ_1 while the fifth harmonic of the vertical field and the seventh of the horizontal field are the most effective in controlling the angular error θ_1.

(c) First-order expressions have been derived for ρ_1 and θ_1 by assuming these quantities to be small. These expressions can be numerically

evaluated if the magnetic field components are known at all points along zero-order the electron trajectory.

We should emphasize at this point the relative merits of the present method of calculating the corner errors and the one described in Ref. [2]. In the method followed by Ref. [2], the deflection of each beam is computed at the corner of the screen and then the differences between these deflections are taken to get the errors. Since these deflections are rather large (about 5 to 13 inches depending on the screen size) compared to the misconvergence errors we are looking for (of the order of 30–50 mils) it is obvious that the results of deflection calculation have to be accurate to within about 0.2% to 1%. Even if the computer program itself might be capable of calculating to such a high degree of accuracy it is virtually impossible to measure all the input data to the program (such as geometric parameters of the kinescope tube and the gun and wire distributions in the coils) to such accuracy. Eqs. [20] and [21], on the other hand, determine the errors directly. If ρ_0 for each beam were known exactly (e.g., from an analytical expression), then any inaccuracy in the computation would have been reflected as a corresponding uncertainty in the value of the error. This would have been a big improvement over the method of Ref. [2]. Unfortunately, in a practical yoke, ρ_0 has to be calculated numerically and the error in this calculation adds to the error in the ρ_1 calculation. Nevertheless, the present method offers a physical insight into the relationship between the misconvergence errors and the various harmonics of the magnetic field that is unavailable in a completely numerical scheme.

We should again point out that our formalism can be applied to calculate the misconvergence at any point at or near the screen boundary where the aberration theory is inadequate. For example, if we apply it to the 3 o'clock position, we get instead of Eqs. [20] and [21]

$$\rho_1(z) = -k\mu_0 \int_{z_0}^{z} dz'[1 + \rho_0'(z')^2]^{1/2} \int_{z_0}^{z'} dz'' \times \sum_{m=3,5\cdots} \frac{m a_m(\rho_0, z'')}{\rho_0(z'')} \quad [24]$$

$$\theta_1(z) = 0. \quad [25]$$

We have restricted ourselves to corner points simply because the convergence errors at the corner are usually more difficult to fix empirically.

Also note that we have some flexibility in the selection of the unperturbed solution. It is not necessary to take the result of the first-

order aberration theory as our unperturbed solution; any *known* curve that is reasonably close to the true path of electrons will serve this purpose. Since, in order to reach the corner point, the electron beam has to run very close to the inner surface of the horizontal coil and eventually emerge in a straight line path towards the corner, it is not too difficult to approximate the beam-path by some known polynomials in z and use that for $\rho_0(z)$ and $\theta_0(z)$. However, since we are calculating the trajectories separately for each beam, a different pair of polynomials must be chosen for each beam. Otherwise we have to worry about the gradient of the field across the beam-bundle on the right-hand side of Eqs. [10] and [11].[5] The advantage of taking the first-order aberration theory result as our zeroth-order solution is that it allows us to drop the $m = 1$ terms from the right-hand sides of Eqs. [18] and [19]. Otherwise Eqs. [20] and [21] get more complicated.

The only problem in applying the present technique to calculate the numerical values of the convergence errors for a given yoke is that it requires numerical integrations *twice* over functions that involve the magnetic field components. Unfortunately, these components themselves require complicated computer programs for their evaluation. It would be very desirable for the purpose of such calculations to have an analytical, even if somewhat approximate, expression for the magnetic field components for various harmonics. The possibility of deriving such an expression is being explored.

Acknowledgment

The author wishes to thank D. E. Laux for many stimulating and helpful discussions.

References:

[1] J. Haatjes and G. J. Lubben, *Philips Res. Report*, **12**, p. 6 (1957) and **14**, p. 65 (1959).
[2] Y. Yokota and T. Toyofuku, *IEEE Trans. on Consumer Electronics*, **25**, p. 91 (1979).
[3] D. M. Fye, J. Applied Physics, **50**, p. 17 (1979).
[4] See, e.g., M. Born and E. Wolf, *Principles of Optics*, Third Ed., p. 128 and 740, Pergamon Press, London (1965).
[5] See R.G.E. Hutter, *IEEE Trans. on Electron Devices*, **17**, p. 1022 (1970).

Patents Issued to RCA Inventors—Second Quarter 1982

April

A. R. Balaban and S. A. Steckler Dual Phase-Control Loop Horizontal Deflection Synchronizing Circuit (4,327,376)
S. L. Bendell Optical Assembly for Color Television (4,323,918)
T. E. Benner and A. Month Mesh Assembly Having Reduced Microphonics for a Pick-up Tube (4,323,814)
R. W. Chambers and F. Cuomo, Jr. Method and Apparatus for Deflashing Molded Recorded Discs (4,326,325)
K. K. Chang System for Enhancing Deflection in Kinescopes (4,323,816)
T. J. Christopher Video Disc Stylus Position Sensor System (4,327,434)
R. R. Demers Wafer and Boule Protection During The Blade Return Stroke of a Wafer Saw (4,326,494)
C. B. Dieterich and F. B. Lang Video Disc Player with Variable Offset RFI Reduction Circuit (4,327,431)
D. F. Dion Sequencer for Power Supply Voltages (4,323,789)
R. A. Dischert and G. A. Reitmeier Data Rate Reduction for Digital Video Signals By Subsampling and Adaptive Reconstruction (4,323,916)
C. A. Elliott Video Disc Player Having Turntable Assist Apparatus (4,326,284)
K. Fukazawa and A. Yamada Video Disc Locked Groove Corrector (4,323,998)
N. F. Gubitose Apparatus for Transferring Pure Abrasive Material From One Hopper to Another (4,325,419)
W. B. Hall Megasonic Jet Cleaner Apparatus (4,326,553)
L. A. Harwood and E. J. Wittman Electronic Filter for Generating a Third Harmonic Signal (4,325,076)
P. M. Heyman and R. L. Quinn Workpiece with Machine Readable Marking Recessed Therein and Method of Making Same (4,327,283)
S. W. Kessler, Jr. Resilient Contact Ring for Providing a Low Impedance Connection To the Base Region of a Semiconductor Device (4,327,370)
F. B. Lang and J. K. Clemens Video Disc Player with RFI Reduction Circuit (4,327,432)
H. M. Langley and J. W. Stephens Video Disc Defect Detector (4,325,134)
A. W. Levine, K. D. Tomeczek and S. A. Harper Method of Metallizing A Phosphor Screen (4,327,123)
M. E. Malchow Circuit Arrangement Useful in Developing Decoupled Operating Voltages for IF Amplifier Stages of an Integrated Circuit (4,327,332)
J. B. McMackin Regulated Switching Apparatus (4,325,021)
M. L. McNeely Method for Producing Disc Records Having Molded-In Center Holes (4,327,047)
M. J. Nierenberg Method of Making a Machine-Readable Marking in a Workpiece (4,323,755)
F. R. Nyman, B. N. Stevens and J. A. Calamari, Jr. High Density Information Disc Processing (4,327,048)
P. E. O'Connell, L. M. Hughes and J. D. Fletcher Video Disc Player Having Carriage Drive Apparatus (4,325,136)
J. R. Preston High Density Information Disc Lubricants (4,327,140)
J. P. Pudlosky Chuck for Use in Testing of Semiconductor Pellets (4,327,325)
W. F. Reichert Method for Forming a Narrow Thin Film Line (4,324,814)
J. P. Russell Urinary Beam Guide/Electron Gun Assembly for Flat Panel Display Devices (4,323,815)
J. P. Russell and C. B. Carroll Envelope for Flat Panel Display Devices (4,325,489)
O. H. Schade, Jr. Temperature-Correction Network for Extrapolated Band-Gap Voltage Reference Circuit (4,325,017)
O. H. Schade, Jr. Temperature-Correction Network with Multiple Corrections as for Extrapolated Band-Gap Voltage Reference Circuits (4,325,018)
J. C. Sokoloski and A. C. Ipri MNOS Memory Transistor (4,323,910)
L. J. Vieland and V. M. Cannuli Spring-Loaded Resistive Lens Structure for Electron Gun (4,323,813)
S. Weisbrod Scanning Waveform Generator for Flat Panel Display Devices (4,326,151)
G. J. Whitley Apparatus for Automatic Adjustment of an Inductor in a Tuned Circuit (4,325,040)

R. Williams Apparatus and Method for Measuring the Rate of Evaporation of a Liquid (4,324,132)
C. T. Wu Hardware Interpretive Mode Microprocessor (4,323,963)

May

G. M. Allardyce, R. N. Moskalczak and E. A. Gronka Method of Checking for Electrical Frit Breakdown in Kinescopes and Apparatus Therefor (4,329,648)
J. Y. Avins Encoder for Recording Incremental Changes (4,328,463)
A. E. Bell Information Record (4,329,697)
S. L. Bendell Line-Scan Still Image Reproducer (4,331,979)
K. K. Chang Horizontal Deflection Enhancement for Kinescopes (4,329,618)
R. W. Clayton Tape Transducer Carrier with Dihedral and Protrusion Adjustment (4,329,724)
B. J. Curtis Method for End Point Detection in a Plasma Etching Process (4,328,068)
P. Datta and E. S. Poliniak High Density Information Record Lubricants (4,330,583)
C. A. Elliott Disc Player Having Turntable Height Varying Apparatus (4,328,575)
J. Gross and W. H. Barkow Alignment-Insensitive Self-Converging In-Line Color Display (4,329,671)
J. R. Harford Television Automatic Gain Control System (4,329,713)
G. Kaganowicz Method for Preparing an Abrasive Coating (4,328,646)
E. O. Keizer Technique for Uniform Stylus Configuration (4,330,915)
H. P. Kleinknecht and H. Meier Optical Line Width Measuring Apparatus and Method (4,330,213)
P. R. Knight Side Pincushion Modulator Circuit with Overstress Protection (4,329,729)
H. Kressel and G. H. Olsen III-V Quaternary Alloy Photodiode (4,328,508)
F. B. Lang Adaptive Distortion Elimination Circuitry for a Video Disc Player (4,329,712)
D. E. Laux and K. E. Meyer Deflection Circuit Linearity Coil (4,331,907)
M. A. Leedom Beam Guide Structure for a Flat Panel Display Device (4,330,735)
A. C. Limm, J. T. O'Brien, T. V. Colgrove and P. Nyul Injection Laser Diode Array Having High Conductivity Regions in the Substrate (4,331,938)
M. E. Malchow Arrangement for Selectively Routing a Signal Indicative of Received Signal Strength to Different Portions of a Radio Receiver in Response to Different Levels of a Control Signal (4,330,866)
A. F. McDonie Rubidium-Cesium-Antimony Photocathode (4,331,701)
S. V. Naimpally Video Blanking Circuit with Controlled Rate of Unblanking (4,330,792)
R. W. Nosker Video Disc Apparatus for Clearing Foreign Matter From the Signal Pickup Stylus During Playback (4,330,881)
T. R. Pampalone Positive Resist for Electron Beam and X-Ray Lithography and Method of Using Same (4,330,671)
R. P. Parker Linear High Gain Sampling Amplifier (4,331,981)
R. P. Parker Sample and Hold Circuit Particularly for Small Signals (4,331,982)
B. P. Patel and J. J. Prusak Record Stamper Protector (4,327,830)
D. H. Pritchard Audio Distortion Eliminator (4,329,714)
W. R. Roach Video Disc Having a Label for Identifying Material Recorded Thereon (4,329,575)
O. H. Schade, Jr. Dynamic Current Supply (30948)
R. L. Schelhorn Method for the Manufacture of Porcelain Coated Metal Boards Having Interconnections Between the Top and Bottom Surfaces (4,328,614)
R. L. Schelhorn Method of Making a Composite Substrate (4,331,700)
R. G. Stewart Overload Protection Circuit for Output Driver (4,329,600)
W. C. Stewart and G. A. Alphonse Apparatus for Monitoring a Wideband Electromechanical Recording System (4,330,882)
L. F. Wallace Low Cost Reduced Blooming Device and Method for Making the Same (4,329,702)
C. M. Wine Adaptive Stylus Kicker Using Disc Track and Disc Sector Information (4,330,879)

June

R. F. Abt and W. L. Behrend Linear Loading for PWM Filter (4,336,615)
R. C. Alig, W. H. Barkow and J. Gross Color Television Display System Having

Improved Convergence (4,335,366)
L. R. Armstrong Testing the Condition of a Turbocharger (4,334,427)
F. Aschwanden Triax Safety Circuit (4,335,412)
S. Berkman and R. Metzl Method of and Apparatus for Growing Crystal Ribbon (4,334,948)
M. D. Bock Apparatus for Molding a Recorded Disc (4,334,849)
G. N. Butterwick Photomultiplier Tube Having Directional Alkali Metal Vapor Evaporation Means (4,333,031)
T. L. Credelle Focus Mesh Structure and Biasing Technique for Flat Panel Display Devices (4,335,332)
K. M. Dinter Digital Tracking System (4,335,408)
W. A. Dischert Length Counter for Web Transport System (4,335,411)
R. L. Giordano Dual Output Switching Circuit (4,337,423)
N. Goldsmith and S. T. Hsu Method of Forming an Improved Gate Member for a Gate Injected Floating Gate Memory Device (4,334,347)
A. M. Goodman Method and Apparatus for Determining Minority Carrier Diffusion Length in Semiconductors (4,333,051)
W. V. Goodwin and J. S. Williams Radar System (4,336,540)
D. E. Greisemer Method for Vaporizing Getter Material in a Succession of Cathode-Ray Tubes (4,335,926)
W. E. Harbaugh Sputter-ion Pump for Use with Electron Tubes Having Thoriated Tungsten Cathodes (4,334,829)
W. E. Harlan Composite Timing Signal Generator with Predictable Output Level (4,337,478)
D. D. Holmes Information Transmission During First-Equalizing Pulse Interval in Television (4,335,402)
M. V. Hoover Differential-Input Complementary Field-Effect Transistor Amplifier (4,333,057)
M. V. Hoover Operational Amplifier Employing Complementary Field-Effect Transistors (4,333,058)
M. V. Hoover Complementary Symmetry FET Frequency Converter Circuits (4,334,324)
M. V. Hoover Class AB Push-Pull Amplifiers (4,335,360)
S. T. Hsu Method of Making Electrically Programmable Control Gate Injected Floating Gate Solid State Memory Transistor (4,332,077)
M. E. Malchow Biasing of Transistor Amplifier Cascades (4,334,198)
E. T. Manson Stone-Positioning Apparatus and Method (4,335,544)
W. Z. Marder Apparatus for Handling Deformable Components Supported in a Matrix (4,333,592)
J. C. Marsh, Jr. and M. L. Snell, Jr. Audio De-Emphasis Circuit (4,335,470)
K. E. McGuire and S. S. Brokl Jam-Resistant TV System (4,333,107)
L. B. Medwin CMOS Device with Silicided Sources and Drains and Method (4,336,550)
S. Miko Free-Running Push-Pull Inverter (4,334,267)
D. B. O'Leary Video Disc Player (264,712)
D. B. O'Leary Video Disc Player (264,713)
P. F. Price Mold Preparation Method (4,332,841)
R. G. Raush Method and Device for Separating Parts from a Strip of Material (4,334,945)
G. A. Reitmeier and R. A. Dischert Adaptive Amplitude Averaging for Weighting Quantizing Noise (4,334,237)
O. H. Schade, Jr. Amplifier Using Lateral and Vertical Transistors (4,334,196)
M. C. Stewart Transducer Displacement Apparatus for Video Disc Player (4,333,174)
R. G. Stewart Memory Circuit with Means for Compensating for Inversion of Stored Data (4,337,522)
D. J. Tanguay and C. E. Weitzel Use of Silicide to Bridge Unwanted Polycrystalline Silicon P-N Junction (4,333,099)
B. K. Taylor Flylead for a Video Disc Stylus Cartridge (4,337,536)
H. R. Warren Crosstalk Filtering Arrangement with Variable Frequency Filtering to Remove Effects of FM Carrier (4,335,394)
D. H. Willis Television Receiver High Voltage Protection Circuit (4,335,335)
C. M. Wine Video Accessory Having Channel Identifier (4,336,555)
J. P. Wittke Method for Machining a Workpiece with a Beam of Radiant Energy Assisted by a Chemically-Reactive Gas (4,332,999)
G. S. Zorbalas Rapid Correlation of Recorded Information (4,335,401)

AUTHORS

Raymond L. Camisa received his BEE, MEE, and PhD degrees from the City College of the City University of New York in 1965, 1969, and 1974, respectively. From 1965 to 1967 he was at the RCA Advanced Communications Laboratory, New York, where he worked on microwave filters, low-noise parametric amplifiers, and microwave integrated-circuit techniques. From 1967 to 1970, as a Member of Technical Staff at Wheeler Laboratories, Inc., Great Neck, LI, he was part of a group developing a microwave integrated-circuit receiver for IFF applications. Specifically, he developed various MIC components including low-noise transistor amplifiers, frequency multipliers, and filters. From 1970 to 1974 he was a part-time lecturer teaching courses in electromagnetic theory, electronics, and microwave measurements. At the university, he also worked as a graduate research assistant investigating the use of MIS varactors in microwave networks. During those years he was a consultant to Wheeler Laboratories and the RCA Advanced Communications Laboratory. In 1974 Dr. Camisa joined the Microwave Technology Center at RCA Laboratories. His responsibilities include research on GaAs field-effect-transistor device technology and linear-amplifier development.

Dr. Camisa has published numerous papers on microwave devices and systems and currently holds two U.S. patents.

Dr. Camisa is an active member of IEEE and has served on many committees on the local chapter level. He is a past chairman of the MTT/ED Princeton section and is a member of Sigma XI.

Basab B. Dasgupta received his B.Sc. and M.Sc. degrees in physics from the University of Calcutta, India and Ph.D. degree from the University of Wisconsin in 1976. He worked as a faculty member of physics at two different campuses of the University of Wisconsin system and as a member of the Electrical Engineering faculty at Marquette University. His area of research has involved electronic, electromagnetic, and acoustic properties of solid surfaces. He joined RCA Consumer Electronics in 1981 as a member of the engineering staff associated with the Advanced Yoke Development group.

Robert A. Donnelly graduated from St. Peters College 1952 with a B.S. in chemistry and later obtained an MBA from Bowling Green State University. After serving four years as a Naval Aviator, he joined the Solid State Division of RCA in Somerville as a production engineer. In 1960, he transferred to the Findlay Ohio facility and was promoted through a series of positions to Manager of Manufacturing and Production Engineering for Integrated Circuits. In 1970, he assumed responsibility for RCA Solid State operations in Taiwan ROC, returning to Findlay in 1973 as Manager Findlay Operations. In 1976, he was named Program Director for the MOS technology transfer program between SSD and the

Industrial Technology Research Institute in Taiwan R.O.C.. In 1980, he joined the Solid State Technology Center as Program Manager and in 1982 was promoted to his present position as Manager Program Management and Business Planning for SSTC.

Hammam Elabd received the BSc degree in Electrical Engineering from Cairo University, Egypt, in 1969, and MSc degrees from the University of Arkansas, Fayetteville, AR, and Rensselaer Polytechnic Institute, Troy, NY, in 1975 and 1979, respectively. He received the PhD degree in Electrical Engineering from Rensselaer Polytechnic Institute in 1979. His PhD thesis described the material, optical, and electrical properties of the PbS-Si heterojunction infrared detector. From 1969 to 1970 Dr. Elabd worked as a system analyst and programmer in the Suez Canal Co. and Cairo University Computer Center. From 1970 to 1975 he was a member of the technical staff of Brown Boveri and Cie A.G., Mannheim, West Germany. From 1974 to 1979 he was a research assistant in the area of solid-state devices in the Department of Electrical Engineering of the University of Arkansas, Purdue University, and Rensselaer Polytechnic Institute. During the same period he served as a consultant and lecturer in the areas of power electronics, remote control, telemetery, and load management systems. He is currently a member of the technical staff at RCA Laboratories Princeton, N.J., where he is involved in the development of Schottky Barrier IR-CCD arrays. This work has led to contributions in the areas of detector process development for the platinum silicide and paladium silicide Schottky-barrier detectors, and detector and IR-CCD image sensor characterization. In 1981 he was awarded an RCA Outstanding Achievement Award for contributions to the science and technology of Schottky-Barrier infrared detectors that have led to the development of high performance IR-CCD image sensors.

Dr. Elabd is a member of the IEEE and the society of Photo-Optical Instrumentation Engineers.

Krishnamurthy Jonnalagadda received his B.Sc. in Physics from the Osmania University, India, in 1964; his B.E. (1967) and M.E. (1969) in Power Systems from the Indian Institute of Science, Bangalore, India; and his Ph.D. (1972) from the Clarkson College in the area of Statistical Theory of Communication. He taught at the Indian Institute of Science and at Clarkson College in the years 1973–1978, where he also conducted research in the areas of interference in digital communications, digital filters, and information theory. He joined RCA Laboratories, Princeton, N.J., in 1978. His work includes analysis and design of voice and video satellite communication systems, and signal processing methods in VideoDisc and Tape Recorders. In 1980 he was awarded an RCA Laboratories Outstanding Achievement Award for analysis of nonlinear crosstalk effects in satellites and 1981 he was awarded the David Sarnoff Achievement Award for work that led to a significant increase in the capacity of the RCA domestic satellite system.

Dr. Jonnalagadda is a member of Eta Kappa Nu, IEEE, and Sigma Xi.

Werner Kern received his education in chemistry in schools in Switzerland and the U.S.A. The research thesis he published in 1947, on the discovery of fluorescing carcinogenic hydrocarbons in soil, established an important new branch of environmental science. He was a research chemist with Hoffmann-La Roche in Switzerland and New Jersey, and later with Nuclear Corporation of America; there he became chief chemist directing research in radiation chemistry. In 1959, Mr. Kern joined RCA Electronic Components and Devices Division to investigate semiconductor processes by radiochemical methods, was project scientist and consultant on several research projects, and was in charge of radiological safety. Since 1964 he has been at RCA Laboratories, Princeton, N.J. as a Member of Technical Staff. He has been working in semiconductor process research, specializing in the characterization and device applications of dielectric films, chemical vapor deposition, and etching processes. From 1974 to 1979 he was project scientist for government-sponsored research contracts on glass passivation, dielectric defects, and silicon solar cells.

Mr. Kern is Vice Chairman of the Dielectric and Insulation Division of the Electrochemical Society, is a member of the American Chemical Society, the American Vacuum Society, the Electrochemical Society, and the Research Honorary Society of Sigma Xi, and is listed in *American Men and Women of Science* and *Who's Who in the East*. He is the author or coauthor of over 80 scientific publications, holds six U.S. patents, has presented numerous invited technical lectures, and has organized scientific symposia. He received an RCA Achievement Award in 1966 for his work in integrated-circuit process research, and is the recipient of the Callinen Award for 1971 of the Electrochemical Society, in recognition of his pioneering research in chemical vapor deposition. Mr. Kern received a 1973 RCA Laboratories Outstanding Achievement Award for his team contributions to the glass passivation of silicon device structures. He also coedited and coauthored a book, *Thin Film Processes*, published by Academic Press in 1978.

Walter F. Kosonocky was awarded BS (1955) and MS (1957) degrees in Electrical Engineering by Newark College of Engineering, Newark, NJ. In 1965, he received the ScD degree in Engineering from Columbia University, New York, NY. Since June 1955, he has been employed at RCA Laboratories, Princeton, NJ. He was appointed a Fellow of the Technical Staff in 1979. At RCA Laboratories, Dr. Kosonocky has been engaged in research on solid-state devices, circuits, and system applications. This work included the following areas: ferrite memories, parametric digital circuits, tunnel diode circuits, applications of lasers as switching and digital devices, optical hologram memories, and MOS photosensor arrays. From 1970 to 1977, he was engaged in the development of charge-coupled devices for digital, imaging, and signal processing applications. Since 1977, he has led a team effort on the development of Schottky-barrier infrared image sensors. He has been granted 38 U.S. patents. He received RCA Laboratories Achievement Awards in 1959, 1963, and 1980, and the RCA David Sarnoff Award in 1981.

Dr. Kosonocky is a member of Tau Beta Pi, Eta Kappa Nu, and Sigma Xi, and Fellow of IEEE. From 1963 to 1967, he was Chairman of the Solid-State Circuits Committee of IEEE's Circuits and Systems Society. From 1974 to 1978, he served as Chairman of the Integrated Circuits Technology Committee of the IEEE Electron Devices Society. He is presently the Chairman of the VLSI Committee of the IEEE Electron Devices Society.

A. Mikelsons has been with RCA since 1956. His career with RCA started at the Surface Communications Systems, Lab in NY which later became the Advanced Communications Laboratory. While there he participated in the development of microwave components for a broad spectrum of applications, including ground to missile, and satellite to ground communications systems. He was a contributor to the development of upconverters and downconverters for army small satellite terminals. He also was a contributor in many broadband parametric amplifier programs.

In 1976 Mr. Mikelsons joined RCA Laboratories in Princeton as a Research Technician, where he has worked on the circuit aspects of microwave GaAs FET power amplifiers. He has participated in the development of both narrow band and broadband FET amplifiers. He currently is involved in the development of lumped-element matching and distributed combining techniques as applied to broadband FET amplifiers.

Louis S. Napoli graduated from Rutgers University 1959 with a BS degree in Electrical Engineering with high honors and was awarded the MS degree in Electrical Engineering in 1961. During the years 1962 to 1965, he did graduate studies at the Polytechnic Institute of Brooklyn, and subsequently completed special courses in Plasma Physics at Princeton University and at the University of California, Los Angeles. He joined RCA Laboratories in 1959, specializing in research related to microwave phenomena in gaseous plasmas. Based on the results of this work, he received an RCA Laboratories' Achievement Award. The same work was cited by Industrial Research magazine as one of the 100 most important achievements in 1963. His subsequent research in microwave phenomena in avalanching semiconducting devices led to a second Achievement Award. A third award was granted for his contribution toward the advancement of microwave integrated circuits, and a fourth, for his pioneering work in the area of GaAs field-effect microwave power transistors. He has been granted more than 25 U.S. patents.

Mr. Napoli has held a research management position as head of a microwave components group that developed L- and S-band avalanching microwave diodes for use as high-power amplifiers and in phased-array radars and transponders, developed and space-qualified K-band avalanching semiconductor amplifiers for satellite communications, and developed manufacturing methods for radar speed indicators and controllers currently used in railroad locomotives. He has also been an engineering manager in the area of concentrator photovoltaics, laying the engineering and manufacturing base for a solar-electric concentrator business. He is currently Head of the LSI Devices and Memories group responsible for the development of CMOS RAMs, EE-PROMs, radiation hardened CMOS/SOS, and technology for digital integrated circuits.

Eugene C. Ngai received the BS degree from the University of Rochester, Rochester, NY, in 1976, his MS from Northwestern University, Evanston, IL, in 1978, and his EE from Syracuse University, Syracuse, NY, in 1980, all in electrical engineering. Since June 1980 he has been with RCA AstroElectronics, Princeton, NJ, where he has been engaged in studies on satellite antennas.

George L. Schnable received a B.S. degree in chemistry from Albright College, Reading, Pa., in 1950, and M.S. and Ph.D. degrees in Chemistry from the University of Pennsylvania, in 1951 and 1953, respectively. From 1953 until 1971, he was employed by Philco-Ford Corporation, where he became Manager of the Advanced Materials and Processes Department in the R & D Operation of the Microelectronics Division. In 1971, Dr. Schnable joined RCA Laboratories, Princeton, N.J., as Head, Process Research, in the Process and Applied Materials Research Laboratory, where he supervised projects dealing with thin-film dielectrics and metallization, silicon device fabrication technology, ion-implantation technology, and silicon device reliability. In 1977, he was named Head, Solid State Process Research. He is presently Head, Device Physics and Reliability in the Integrated Circuit Technology Laboratory of RCA Laboratories.

Dr. Schnable holds over 20 U.S. Patents and is listed in American Men and Women of Science. He is a Member of the American Chemical Society, the Electrochemical Society, the Franklin Institute, the Pennsylvania Academy of Science, Alpha Chi Sigma, Phi Lambda Upsilon, and Sigma Xi; a Senior Member of the American Association for the Advancement of Science and the Institute of Electrical and Electronics Engineers; and a Fellow in the American Institute of Chemists.

Ronald K. Smeltzer received the B.S. degree in Electrical Engineering from Bucknell University in 1964, and the M.S. and Ph.D. degrees in Electrical Engineering from Northwestern University in 1968 and 1970. Prior to joining RCA Laboratories, Dr. Smeltzer was with Southern Methodist University, Texas Instruments Inc., and Princeton University; during this period, his research interests included the growth and characterization of compound semiconducting materials, device fabrication with compound semiconductors, and the development of silicon photovoltaic cells. At Texas Instruments he developed various silicon technologies, including a new selective epitaxial deposition process, for the fabrication of a radiation hardened, vertical multijunction solar cell. From 1975 to 1978 Dr. Smeltzer was Assistant Professor in the Department of Electrical Engineering at Princeton University. He then joined RCA Laboratories, where he has worked on the development of technologies for radiation hardening of integrated circuits. At the present time, he is concerned with process development and device characterization for the RCA hardened CMOS/SOS process.

Dr. Smeltzer is a member of the Electrochemical Society and the New York Microscopical Society.

Binboga Siddik Yarman received his BS degree in Electrical Engineering from the Technical University of Istanbul, Istanbul, Turkey, 1974 and his MEEE from Stevens Institute of Technology in New Jersey in 1977. He completed his Ph.D. in the area of broadband matching at Cornell University in November 1981. In 1982, he joined RCA Laboratories, David Sarnoff Research Center, Princeton, N.J. He is currently working on new design concepts for broadband, multi-stage microwave amplifiers. His interests include analytic and computer-aided designs of passive and active microwave circuits.

Dr. Yarman is a member of the IEEE and the Turkish Electrical Engineers Chamber.

J. Yeh received a BS degree in Electrical Engineering from National Taiwan University in 1968, and an MS degree in Electrical Engineering and a Ph.D. degree in Solid State Physics from the University of Alabama in 1972 and 1977, respectively. His dissertation work involved the radiation effects to the ferroelectric phase transistion in organic crystals. Dr. Yeh was at Yale University from 1977 to 1979, studying ferromagnetic resonance in thin metal films and stress induced magnetic anisotropy in magnetic alloy wires. In 1979, Dr. Yeh joined the Solid State Technology Center of RCA Laboratories at Somerville, N.J. He has engaged in the development of a computer controlled automation system for device and process evaluation in the semiconductor integrated circuits. Since 1980, Dr. Yeh has worked on the development of radiation hardened silicon gate CMOS technologies. He has been instrumental in the establishment of a radiation hardened C^2L CMOS bulk-Si technology and a radiation hardened CMOS/SOS technology for various high reliability aerospace and military applications.

Dr. Yeh is a member of Eta Kappa Nu, Sigma Pi Sigma, and IEEE.